Investigation on Selective Laser Sintering of Micro-nano Scale Metallic Powder

Thesis submitted by

Srijan Paul

Doctor of Philosophy (Engineering)

School of Laser Science and Engineering
Faculty Council of Engineering & Technology
Jadavpur University
Kolkata, India

2019

JADAVPUR UNIVERSITY
KOLKATA – 700032, INDIA

INDEX NO. 297/12/ENGG

1. **Title of the Thesis :** Investigation on Selective Laser Sintering of Micro-nano Scale Metallic Powder

2. **Name, Designation & Institution of Supervisor/s :**

   (a) Prof. (Dr.) Souren Mitra
   Professor,
   Production Engineering Department,
   Jadavpur University,
   Kolkata – 700032,
   India

   and

   (b) Dr. Nagahanumaiah
   Director,
   Central Manufacturing Technology Institute,
   Bangalore – 560022,
   India

3. **List of Publication (1):**

   (a) Journal Publications:

   Paul, Srijan, Nagahanumaiah and Mitra, Souren, 2019, **A Study on Porosity in Micro-Selective Laser Sintering of Copper Powder**. *Manufacturing Technology Today, Vol.18*(Issue-1), pp.3-10

(b) Book Chapter Publication (1):

Paul, Srijan, Nagahanumaiah, Mitra, Souren, Roy, Debabrata, 2018. **Molecular Dynamics Simulation Study of Neck Growth in Micro-selective Laser Sintering of Copper Nanoparticles**. In *Simulations for Design and Manufacturing* (pp. 259-292). Springer, Singapore.

(c) Conference Publications (3):

(i) Paul, Srijan; Nagahanumaiah; Mitra, Souren, **"Selective Laser Sintering of 5µm Copper Powder using Nd-YAG Nanosecond Pulsed Laser"** in International Conference on Precision, Micro, Meso and Nano Engineering (COPEN-7, 2011), December 11–12, 2011, at COEP-Pune, India

(ii) Paul, Srijan; Nagahanumaiah; Mitra, Souren and Roy, Debabrata, **"Molecular Dynamics Simulation Study of Neck-growth in Micro-Selective Laser Sintering of Copper Nanoparticles."** in 6th International & 27th All India Manufacturing Technology, Design and Research Conference (AIMTDR-2016), December 16–18, 2016, at COEP-Pune, India

(iii) Paul, Srijan; Nagahanumaiah; Mitra, Souren, **"Investigation of defects in Selective Laser Sintering of submicron scale copper powder"** in 1st International Conference on Emerging Trends in Engineering and Science (ETES-2018), March, 23–24, 2018 at AEC-Asansol, India

4. List of Patents: NIL

5. List of Presentations in National/International/Conferences/Workshops (3):

(i) Paul, Srijan; Nagahanumaiah; Mitra, Souren, **“Selective Laser Sintering of 5µm Copper Powder using Nd-YAG Nanosecond Pulsed Laser”** in *International Conference on Precision, Micro, Meso and Nano Engineering (COPEN-7, 2011)*, December 11–12, 2011, at COEP-Pune, India

(ii) Paul, Srijan; Nagahanumaiah; Mitra, Souren and Roy, Debabrata, **“Molecular Dynamics Simulation Study of Neck-growth in Micro-Selective Laser Sintering of Copper Nanoparticles.”** in *6th International & 27th All India Manufacturing Technology, Design and Research Conference (AIMTDR-2016)*, December 16–18, 2016, at COEP-Pune, India

(iii) Paul, Srijan; Nagahanumaiah; Mitra, Souren, **“Investigation of defects in Selective Laser Sintering of submicron scale copper powder”** in *1st International Conference on Emerging Trends in Engineering and Science (ETES-2018)*, March, 23–24, 2018 at AEC-Asansol, India

CERTIFICATE FROM THE SUPERVISOR/S

This is to certify that the thesis entitled **“Investigation on Selective Laser Sintering of Micro-nano Scale Metallic Powder”** submitted by Shri **Srijan Paul**, who got his name registered on **5th April, 2012** for the award of Ph.D. (Engg.) degree of Jadavpur University in absolutely based upon his own work under the supervision of **Prof. (Dr.) Souren Mitra and Dr. Nagahanumaiah** and that neither his thesis nor any part of it has been submitted for any degree / diploma or any other academic award anywhere before.

1. ____

Prof. (Dr.) Souren Mitra
Professor, Production Engineering Department,
Jadavpur University, Kolkata – 700032, India

2. ____

Dr. Nagahanumaiah
Director, Central Manufacturing Technology Institute, Bengaluru – 560022, India

Dedicated to my Parents

ACKNOWLEDGEMENTS

I wish to avail this opportunity to express my sincere gratitude, regards and indebtedness to my Supervisors, Prof. (Dr.) Souren Mitra, Professor, Production Engineering Department, Jadavpur University, Kolkata and Dr. Nagahanumaiah, Director, Central Manufacturing Technology Institute, Bangalore, for their expert guidance while executing the present research work and introducing me to the exciting field of selective laser sintering of submicron sized metallic powder. Their strict vigilance, generous help and continuous encouragements were instruments in giving my work its final shape.

I would like to express my gratitude to Prof. (Dr.) Dipten Misra, Professor and Director, School of Laser Science and Engineering, Jadavpur University, Kolkata, for his kind permission to carry out the course of work and to use laboratory equipment for conducting experiments.

I am grateful to Dr. Abhiram Hens, Scientist at CSIR-Central Mechanical Engineering Research Institute, Durgapur for introducing me to the fascinating field of Molecular Dynamics.

I am thankful to my colleague Mr. Debabrata Roy for his help to conduct virtual experiments using Molecular Dynamics simulations.

I owe my thanks to Mr. Abhijit Mondal and Mr. Subhasis Biswas, NDT and Metallurgy Lab., CSIR-Central Mechanical Engineering Research Institute, Durgapur for helping in taking images in Scanning Electron Microscope.

I am deeply indebted to Dr. Aditya Kr. Lohar, Principal Scientist at CSIR-Central Mechanical Engineering Research Institute, Durgapur for giving me the opportunity to carry out sintering experiments in his laboratory and encouraging during the work and to Piyush, Sarbani and Apurba for assisting me during the experiments.

My special thank goes to Mr. Shatrughna Dhara, Mr. Vijay, Mr. Saurav Halder and Arjita of Microsystem and Technology Lab., CSIR-Central Mechanical Engineering Research

Institute, Durgapur for helping me to collect the raw materials of my work and without their help my work would not have been possible.

It is indeed a pleasure to thank all my labmates and all the fellow friends in lab. in CMERI-Durgapur and School of Laser Science and Engineering for the joyous company.

I would also like to express my thankfulness to all staff members, research scholars of School of Laser Science and Engineering specially Rajada and Srijnoy for their cooperation and support during my research tenure.

I cannot forget to express my thankfulness to my enjoining friends Kailash Mondal, Sourav Patra and Dhiraj Bajpai for their cooperation in my research work.

I am grateful to CSIR-Central Mechanical Engineering Research Institute, Durgapur for providing me the resources, infrastructure of laboratory and instrumental facilities without any financial charges to accomplish my research work.

Word cannot express my feelings and gratitude for my MAA and BABA without whose upbringing, teaching and guidance I would have never reached this stage of my life. The constant moral support, sympathy and tenderness of my MAA and BABA could only be felt. I would like to thank my sister for supporting me spiritually throughout my research work and my life in general.

The profound love and company of Meghnath helped me to overcome many difficult situations during the whole journey.

Finally, I would like to pray to the ‘Almighty’ for giving me the strength and patience to accomplish my task.

Srijan Paul

PREFACE

Since past few years Selective Laser Sintering has become a popular technique in the field of Additive Manufacturing (bottom-up approach). Layer-by-layer selective laser sintering of powder is one such process widely accepted for ceramic and metal prototype manufacturing. During the process of selective laser sintering the powder particles are converted into a coherent solid mass by selectively laser heating without through melting. Selective laser sintering is extensively used for manufacturing customised complex shape parts of various materials which are used in electronics, aeronautical, automobile and biomedical applications. The process of selective laser sintering of submicron (less than 10µm) size powder particles is still under research and development. Study of past literatures revealed that there are many challenges to effective sintering of micro-nano scale metallic powder in the area of powder handling, grain growth effects, effect of change in refractory index and its effect on laser absorption power etc.

Few researchers used molecular level simulation to analyze neck formation and resulting porosity during laser sintering of nanosized powder particles. During molecular level simulations of laser sintering, atom movements are observed. Past literatures revealed that major number of atoms are diffused from the surface and grain boundary of the particles. A whirling rotation of atoms is visible from the vector plots of diffused atoms. The direction of atom movements is especially towards the contact point of adjacent particles or towards the neck. During molecular level simulations, heating rate shows great influence on the mechanism of sintering and neck formation. Several processing parameters like heating rate, particle size, multi-material, powder of different particle size etc. influence the neck formation between adjacent particles.

Present research is focused on investigating several issues associated with laser sintering of submicron size metallic powder in the range of a nanometer to less than 10µm. For better understanding these mechanisms of sintering, neck growth and resulting porosity have been investigated by both theoretical and experimental techniques.

TABLE OF CONTENTS

Chapter No.	*Chapter Name*	*Page No.*
	Title of the Thesis	i – iii
	Certificate of supervisors	v
	Acknowledgements	ix – x
	Preface	xi
	Table of contents	xiii – xv
	List of Tables	xvii
	List of Figures	xix - xxii
CHAPTER – 1	**INTRODUCTION**	**1 – 37**
1	Introduction	1
1.1	Additive Manufacturing	1
1.2	Challenges of Additive Manufacturing	3
1.3	Selective Laser Sintering (SLS)	4
1.3.1	Materials for Selective Laser Sintering	6
1.3.2	Lasers for Selective Laser Sintering	6
1.3.3	Potentials and Limitations of Selective Laser Sintering	7
1.3.4	Sintering Mechanisms	8
1.3.5	Mechanism of Neck Formation	10
1.3.6	Binding and Consolidation Mechanisms	13
1.4	Review of past research	16
1.4.1	Review of literatures on Theoretical Aspects of Selective Laser Sintering	17
1.4.2	Review of literatures on Alternative Materials used in Selective Laser Sintering	21
1.4.3	Review of literatures on Selective Laser Sintering of micro-scale powder materials	23
1.4.4	Review of literatures on process optimisation of Selective Laser Sintering technique	27
1.4.5	Review of literatures on Application of Selective Laser Sintering	32
1.5	Objective of Present Research	34

CHAPTER – 2 MOLECULAR DYNAMICS SIMULATION OF SELECTIVE LASER SINTERING **37 - 88**

2.1 Molecular Dynamics Simulation and its approaches 37

2.2 Fundamental Concepts of Molecular Dynamics 38

2.2.1 Interatomic/Intermolecular Potential 39

2.2.2 Integration Algorithm 44

2.3 Thermodynamic Ensembles 47

2.4 Molecular Dynamics (MD) Simulation for Selective Laser Sintering of Nanoparticles 48

2.5 Investigation of Neck Growth Mechanism and Porosity Formation during Selective Laser Sintering using Molecular Dynamics simulation-based Virtual Experiments 49

2.5.1 Molecular Dynamics Simulation-based Virtual experiments to explore mechanism of neck-growth in process of Laser Sintering of pair of Nanoparticles 50

2.5.2 Molecular Dynamics Simulation-Based Virtual Experiments to explore atomic displacement during growth of neck in laser sintering of nano-particles using same heating rate 63

2.5.3 Molecular Dynamics Simulation-based Virtual Experiments to explore effect of particle size to minimize porosity level during laser sintering of copper nanoparticles under same heating rate 78

2.6 Summary 86

CHAPTER – 3 INVESTIGATION OF SELECTIVE LASER SINTERING OF MICRO-SCALE COPPER POWDER USING NANOSECOND PULSED ND:YAG LASER **89 – 104**

3.1 Experimental Setup 89

3.2 Materials and Methods 92

3.3 Results and Discussions 96

3.4 Summary 103

CHAPTER – 4 INVESTIGATION OF SELECTIVE LASER SINTERING OF MICRO-SCALE COPPER POWDER USING CONTINUOUS WAVE LASER 105 – 130

4.1 Experimental Setup 105
  4.1.1 Continuous Wave Fibre Delivered Diode Laser Setup 105
  4.1.2 Continuous Wave Fibre Array Packages (FAP) Diode Laser Setup 107
4.2 Materials and Methods 108
  4.2.1 Selective Laser Sintering using Continuous Wave (CW) Fibre Delivered Diode laser 109
  4.2.2 Selective Laser Sintering using Continuous Wave (CW) Fibre Array Packages (FAP) Diode Laser 113
4.3 Results and Discussions 115
  4.3.1 Selective Laser Sintering using Continuous Wave (CW) Fibre Delivered Diode laser 116
  4.3.2 Selective Laser Sintering copper powder blended with binder material using Continuous Wave (CW) Fibre Array Packages (FAP) Diode Laser 124
4.4 Summary 128

CHAPTER – 5 GENERAL CONCLUSIONS AND FUTURE SCOPE 131 – 136

5.1 General Conclusions 131
5.2 Future Scope 134

REFERENCES 137 – 146

LIST OF TABLES

Table No.	Caption	Page No.
Table 1.1	Lasers used in Selective laser sintering of different materials	7
Table 1.2	Six common mechanisms of sintering	9
Table 1.3	Stages of Neck formation	10
Table 2.1	Basic thermodynamic ensembles	48
Table 2.2	Change in temperature and neck diameter w.r.t. time during isothermal sintering simulation	53–55
Table 2.3	Change in temperature and neck diameter w.r.t. time during non-isothermal sintering simulation	56–57
Table 2.4	Change in D1 (diameter of particle) and D2 (Fig. 2.4)	60–62
Table 2.5	Change of Temperature, Neck diameter, Neck growth (%) and MSD w.r.t. Time	73–74
Table 2.6	Comparison of pore area in different models during sintering simulation	84–85
Table 3.1	Specification of Nano-second pulsed Nd-YAG Laser Setup	90–91
Table 3.2	Specification of Optical Microscope	92
Table 3.3	Copper Powder	92–93
Table 3.5	Various Laser Parameters used for SLS of almost dry Copper Powder in Diode Pumped Nanosecond-pulsed Nd:YAG laser	94
Table 3.6	Various Laser Parameters used for SLS of Copper Powder blended with Silicon Oil (binder material) in Diode Pumped Nanosecond-pulsed Nd:YAG laser	95
Table 4.1	Copper Powder	108
Table 4.2	Silicon oil as Binding Material	109
Table 4.3	Various laser parameters used for SLS of Dry Copper Powder using CW Fibre Delivered Diode Laser	110
Table 4.4	Various laser parameters for SLS of Copper Powder with Silicon Oil using CW Fibre Delivered Diode laser	112
Table 4.5	Various laser parameters used for SLS of Copper Powder with Silicon Oil binder material in CW FAP diode laser	114

LIST OF FIGURES

Fig. No.	Caption	Page No.
Fig. 1.1	Additive Manufacturing	2
Fig. 1.2	Schematic diagram of Selective Laser Sintering System	5
Fig. 1.3	Schematic diagram of Selective Laser Sintering process	5
Fig. 1.4	Sintering Mechanisms	9
Fig. 1.5	Schematic of stages of neck formation between two particles during selective laser sintering	11
Fig. 1.6	SEM micrograph of neck growth during selective laser sintering	12
Fig. 1.7	Schematic for porosity between the particles during Sintering	12
Fig. 1.8	SEM image of formed pores between particles during SLS	13
Fig. 1.9	Laser-based powder consolidation mechanisms	15
Fig. 2.1	LJ Potential energy vs. intermolecular separation curve	40
Fig. 2.2	Morse Potential energy vs. intermolecular separation curve	42
Fig. 2.3	Flowchart of MD simulation study	49
Fig. 2.4	Atomistic model of copper particles of diameter (D1)=1.82nm with 0.02 nm gap between two particles; D2=(2×D1+0.02)nm	51
Fig. 2.5	Temperature vs Time graph for Isothermal sintering at different temperatures (300K, 600K, 900K, 1200K and 1500K) (following Table 2.2)	52
Fig. 2.6	Temperature vs Time graph for non-isothermal sintering from temperatures 300K- 1500K (following Table 2.3)	59
Fig. 2.7	Neck diameter vs time graph during isothermal sintering at set of temperatures (following Table 2.2)	59
Fig. 2.8	Configuration changes of Cu-Cu pair during sintering	60
Fig. 2.9	Change in dimension of D1 and D2 in non-isothermal sintering process	62
Fig. 2.10	Neck diameter vs. Time graph during non-isothermal sintering (following Table 2.3)	63
Fig. 2.11	Initial Copper nano-particles pair models of size 1nm, 2nm and 3nm particle size (figures are not in scale)	64

Fig. No.	Caption	Page No.
Fig. 2.12	Snap shots of sintering the 1nm nanoparticle pair at time steps 5.6ps, 12ps, 18.4ps, 24.8ps and 30ps	67
Fig. 2.13	Snap shots of sintering the 2nm nanoparticle pair at time steps 5.6ps, 12ps, 18.4ps, 24.8ps and 30ps	68
Fig. 2.14	Snap shots of sintering the 3nm nanoparticle pair at time steps 5.6ps, 12ps, 18.4ps, 24.8ps and 30ps	69
Fig. 2.15	Vector plots of atom displacements during sintering of 1nm pair of nanoparticles at 5.6ps, 12ps, 18.4ps, 24.8ps and 30ps time	70
Fig. 2.16	Vector plots of atom displacements during sintering of 2nm pair of nanoparticles at 5.6ps, 12ps, 18.4ps, 24.8ps and 30ps time	71
Fig. 2.17	Vector plots of atom displacements during sintering of 3nm pair of nanoparticles at 5.6ps, 12ps, 18.4ps, 24.8ps and 30ps time	72
Fig. 2.18	Change in Temperature w.r.t. Time during sintering of pairs of copper nanoparticles (following Table 2.5)	75
Fig. 2.19	Neck size Variation with Time throughout the process of laser sintering of copper nanoparticle pairs (following Table 2.5)	75
Fig. 2.20	Percentage of neck growth with reference to particle size and variation of neck growth percentage with time of heating during laser sintering of nanoparticle pairs (following Table 2.5)	76
Fig. 2.21	Mean Square Displacement (Å2) vs Time (picosecond) curve throughout the process of laser sintering of pairs of nanoparticles (following Table 2.5)	77
Fig. 2.22	Atomistic models of four Copper nanoparticles (a) each particle diameter 0.72nm, (b) each particle diameter 1.82nm and (c) each particle diameter 3.64nm (no gap is kept between particles)	79

Fig. No.	Caption	Page No.
Fig. 2.23	Snapshots of sintering simulation of the model of 0.72nm sized nanoparticles at time steps (a) 0ps, (b) 10ps, (c) 20ps and (d) 30ps	81
Fig. 2.24	Snapshots of sintering simulation of the model of 1.82nm sized nanoparticles at time steps (a) 0ps, (b) 10ps, (c) 20ps and (d) 30ps	82
Fig. 2.25	Snapshots of sintering simulation of the model of 3.64nm sized nanoparticles at time steps (a) 0ps, (b) 10ps, (c) 20ps and (d) 30ps	83
Fig. 2.26	Pore area (nm2) vs Time (picosecond) graph during laser sintering for different models of four nanoparticle (following Table 2.6)	85
Fig. 3.1(a)	Schematic diagram of various parts of Nanosecond pulsed diode pumped Nd:YAG laser and 3D scanning head	89
Fig. 3.1(b)	Pictorial view of Nanosecond pulsed diode pumped Nd:YAG laser system integrated with 3D scanner (QUANTA-SYSTEM)	90
Fig. 3.2	Optical Microscope	91
Fig. 3.3	Type of hatch and hatch space during Selective Laser Sintering of Micro-Scale Copper Powder Using Pulsed Nd-YAG Laser	94
Fig. 3.4	Miniaturized laser sintered part of Copper Powder blended with Silicon Oil	95
Fig. 3.5	Micrographs of selective laser sintered dry copper powder of 5µm average particle size	97
Fig. 3.6	Micrographs of selective laser sintered copper powder of 5µm average particle size blended with silicon oil	98
Fig. 3.7	Micrographs of selective laser sintered copper powder of 5µm average particle size blended with silicon oil	99–101
Fig. 4.1(a)	Schematic diagram of Continuous Wave Fibre Delivered Diode Laser Setup	106

Fig. No.	Caption	Page No.
Fig. 4.1(b) and (c)	Pictorial view of Continuous Wave Fibre Delivered Diode Laser Setup (Developed in CSIR-CMERI, Durgapur)	106
Fig. 4.2(a)	Pictorial view of Fibre Array Packages (FAP) Diode laser Set up (Developed at School of Laser Science and Engineering in Jadavpur University, Kolkata)	107
Fig. 4.2(b)	Schematic diagram of Fibre Array Packages (FAP) Diode laser Set up	108
Fig. 4.3	Style of hatch and hatch space during Selective Laser Sintering of Micro-Scale Copper Powder Using Continuous Wave (CW) Fibre Delivered Diode Laser	110
Fig. 4.4	Pictorial view of the micropart developed by selective laser sintering of dry copper powder of 5µm average particle size (Sample S8)	111
Fig. 4.5	Pictorial view of the part developed by selective laser sintering of copper powder with Silicon Oil Binder	112–113
Fig. 4.6	Type of hatch and hatch space during Selective Laser Sintering of Micro-Scale Copper Powder Using Continuous Wave (CW) FAP Diode Laser	114
Fig. 4.7	Pictorial view of samples of selective laser sintered copper powder of 5µm average particle size blended with silicon oil (scanned under FAP CW Diode laser)	115
Fig. 4.8	SEM Micrographs of selective laser sintered dry copper powder of 5µm average particle size (scanned under CW Fibre Delivered Diode laser)	118–119
Fig. 4.9	SEM Micrographs of selective laser sintered copper powder of 5µm average particle size blended with silicon oil (different laser parameters shown in Table 4.4)	120 – 122
Fig. 4.10	SEM Micrographs of selective laser sintered copper powder of 5µm average particle size blended with silicon oil (scanned under CW FAP Diode laser)	126–128

CHAPTER – 1

INTRODUCTION

1. Introduction

Machining of complex shapes on advanced hard materials is found to be difficult in conventional machining processes. Often poor surface finish, low material removal rate (MRR) becomes an issue for precision engineering applications. Moreover, with the emerging trend towards micro-nano systems, machining by many of the conventional methods impose challenges with respect to cutting tools minimum feature size and finish of machined surface. While application of non-conventional machining processes, namely, Electrochemical Machining (ECM), Electric discharge machining (EDM), Laser beam machining (LBM), Wire-cut Electric discharge machining (W-EDM) etc., for micro-machining solved some of these problems to a great extent. They become a handicap, particularly in complex 3D feature machining in the submicron and nano-scales. In this context bottom up approach of manufacturing is proving to be one of the alternative options.

Since the last few decades rapid growth in application of the rapid prototyping (RP) technique has been observed in the field of additive manufacturing (AM). Since last few years, a number of technologies have been developed based on layered manufacturing concepts. Selective laser sintering (SLS) is one of the popular additive manufacturing techniques which has been widely accepted for producing metallic and ceramic prototypes. SLS is one of the advantageous techniques among the techniques of Additive Manufacturing, in which production cost is quite low and processing time is short.

The consistently growing competition in the global market for manufacturing products alongside improvement of novel techniques. The present global market demands extremely customized products in the shortest possible time, which forces the upgradation of new approaches of manufacturing as an alternative to traditional manufacturing.

1.1 Additive Manufacturing

Additive Manufacturing is a technique of manufacturing of three-dimensional products using layer-by-layer manufacturing approach. Fabricating 3D microparts of complex geometry using Additive Manufacturing technique is widely accepted and is profitable over the conventional techniques [01]. This technique is also named as Layered Manufacturing

(LM) or Solid Freeform Fabrication (SFF). Additive Manufacturing technique involves in building up product part by fusing successive layers of powder material, one on another. This technology is advantageous to produce the part with complex geometry due to the additive built-up nature of manufacturing. The fusion technologies of a thin layer of powder bed are versatile and widely adapted with respect to an extensive range of materials e.g. plastics, metals, ceramics, composites, etc. [02], [03] as well as for a vast area of applications e.g. biotechnology, medical, electronics, automotive, aerospace etc. [01], [03], [04]. Using Additive Manufacturing technique macro and microscale 3D parts of complex geometry can be produced quickly directly from 3D CAD data. In the process of Additive Manufacturing intermediate tooling steps are entirely eradicated, as a result production cost and time are diminished. The layer-by-layer build-up principle of Additive Manufacturing technique is shown in Fig. 1.1. Using 3D CAD data laser beam scans the layers of powder material. Initially, the powder layer on the substrate is scanned (Fig. 1.1(a)). Later, powder layers are spread over the first developed layer and scanned by laser beam to build the part (Fig. 1.1(b) and (c)).

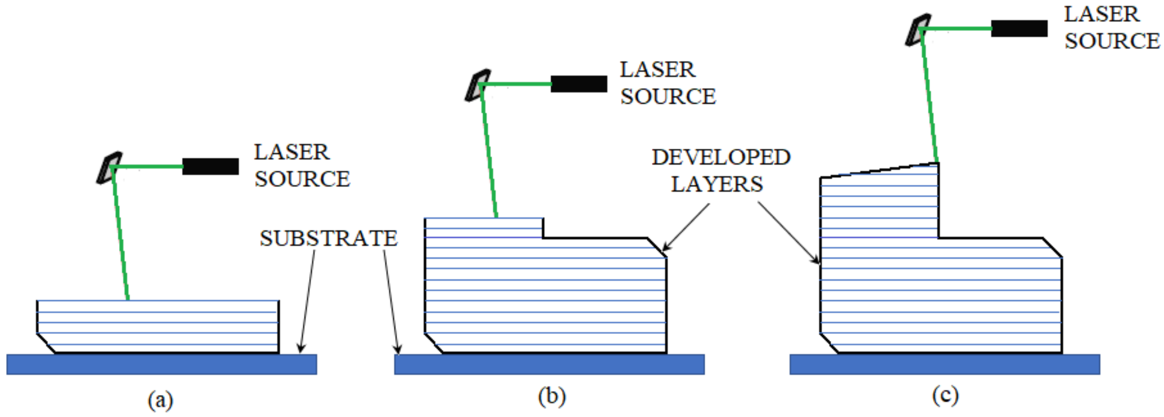

Fig. 1.1 Additive Manufacturing

The seven categories of Additive Manufacturing techniques [03], [05], classified by the International Organisation for Standardisation (ISO), are (i) Binder jetting (BJ), (ii) Directed energy deposition (DED), (iii) Material extrusion (ME), (iv) Material jetting (MJ), (v) Powder bed fusion (PBF), (vi) Sheet lamination (SL) and (vii) Vat photopolymerization (VP). Over the last few decades, a rapid growth has been observed in the class of manufacturing of Additive Manufacturing. Due to layer-by-layer build-up principle, Additive Manufacturing technique is advantageous to produce parts with complex geometrical shapes. This offers potentials in optimizing even by geometrical means. Additive Manufacturing allows rapid production of 3D parts with complex geometry of designed macro and microstructure using CAD data. Production time and cost get reduced as it entirely removes the intermediate tooling steps. It has the additional important advantage, that is production cost as well as production time almost remain unchanged with the degree of geometrical complexity.

In the last few decades the practice of additive manufacturing is increased in the field of direct production of parts. A few of Additive Manufacturing techniques, are popular and playing leading role in the commercial manufacturing field. The powder based fusion technologies become more adaptable with respect to engineering materials as well as vast application area in sector of biomedical, aerospace, automotive, etc. Selective laser sintering (SLS) showed great possibilities in the view of qualifying the necessities of direct manufacturing sectors. These techniques are able to process common engineering materials and showing great results in microstructural and mechanical properties of produced parts. All the technologies have some advantages and disadvantages depending on the type of materials, manufacturing details, and post processing. In present research Selective Laser Sintering (SLS) technology is focused. Selective laser sintering (SLS) is one of the popular additive manufacturing techniques which has been widely accepted for producing metallic and ceramic prototypes.

1.2 Challenges of Additive Manufacturing

Although Additive Manufacturing technology has a wide range contribution in manufacturing, challenges remain in producing complex shape and size of the part, choosing materials and develop metrological properties of produced parts. Common challenges in fabrication using Additive Manufacturing technique are in the range of robustness, safety, self-sufficiency, system integration required in high speed manufacturing of high resolution featured and dimensionally accurate products using low energy. Surface finish, feature size, oxidation of material, product variety and quality are other challenges of Additive Manufacturing technique. Different new engineering materials are developing day by day and part size in the range of micro-nano scale is highly demanding in present world of manufacturing. Handling the different state, forms and types of materials, machines and appropriate Additive Manufacturing technologies are significantly challenging. Currently, there are novel efforts to recognize and overcome complicacy of materials handling, product variety with the help of high-level customized Additive Manufacturing machineries and techniques [05]. Observation during fabrication, using high speed camera of laser scanning improved product quality. Several researches are undergoing to understand and overcome metrological challenges. With the help of several non-destructive testing, microstructural studies with high resolution microscopy, the metrological challenges have been tackled. Several novel techniques of AM are under research and development to understand and overcome the challenges of range of materials and range of submicron level products. Selective Laser Sintering (SLS) is one of the novel techniques of AM to accept and resolve a lot of challenges.

1.3 Selective Laser Sintering (SLS)

In Selective laser sintering (SLS) three-dimensional parts are produced by scanning thin layers of powder materials with laser beam selectively. In this process, the fabrication temperature is maintained at just below the melting temperature of the powder material. The heat is supplied through the laser beam and that slightly elevates the temperature, resulting in sintering.

Fig. 1.2 is showing the schematic of typical SLS system. The system consists of a laser source, optical devices to focus the laser beam, machine control unit, and work table. Before starting of the sintering process, a thin powder-layer is created, on the substrate kept on top of work table or directly on the top of the work table, with the help of a coater (Fig. 1.3(a)). Once the coating process is over, the layer of powder layer is scanned selectively with the laser beam (Fig. 1.3(b)). Laser scanning path is controlled by movement of CNC work table, in x-y direction, using the generated CAD data saved in the Machine Control Unit (MCU). After completion of sintering the first layer of powder, the next layer is spread over the top of the previous layer and scanned selectively using laser beam as shown in Fig. 1.3(c). Similar way other layers are coated and sintered selectively using laser beam to create a 3D part as shown in Fig. 1.3(d).

During selective laser sintering, the first layer of powder particles create bond with one another as well as with the substrate. From the second layer of powder particles create bond with the neighbouring un-sintered particles as well as with previously sintered powder layer to build a solid 3D structure. For sintering every layer of powder, the focal length of the laser beam is adjusted by moving up the laser scanner along z-direction using the stored CAD data in the MCU.

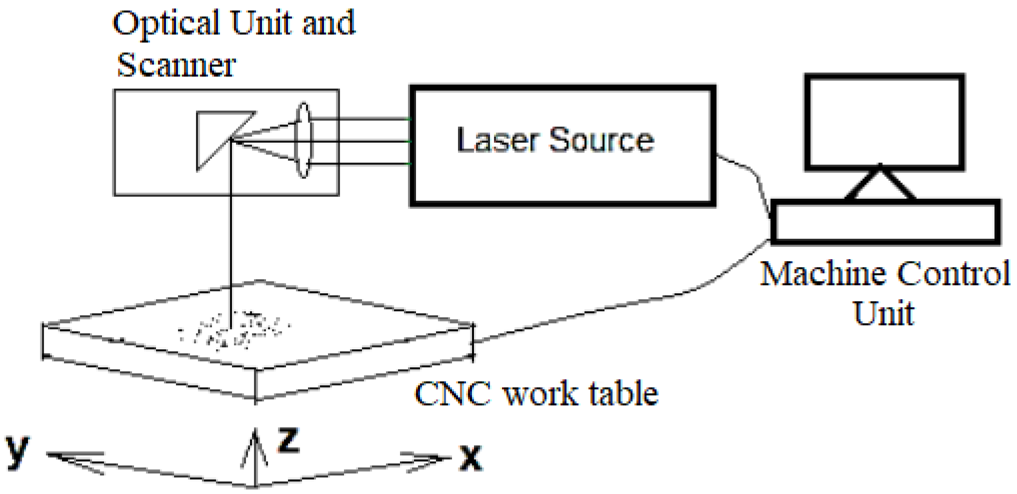
Optical Unit and Scanner
Laser Source
Machine Control Unit
CNC work table
y
z
x

Fig. 1.2 Schematic diagram of Selective Laser Sintering System

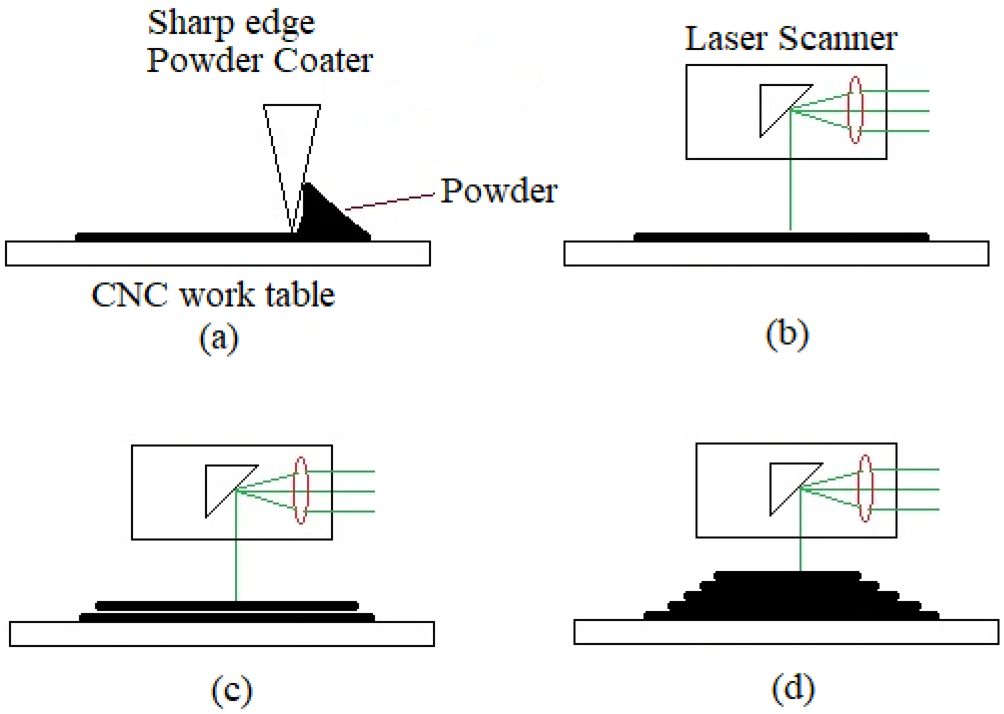
Sharp edge Powder Coater
Powder
CNC work table
Laser Scanner
(a)
(b)
(c)
(d)

Fig. 1.3 Schematic diagram of Selective Laser Sintering process

1.3.1 Materials for Selective Laser Sintering

Selective Laser Sintering is one of the suitable and popular technique among the fusion technologies of thin layer of powder of an extensive range of non-metallic, metallic and composite materials that can build 3D complex geometry parts [03]. Initially selective laser sintering technique was applied to process various polymers. In liquid state polymer materials are highly viscous, are less reactive with gases and have low surface energy and low thermal conductivity. Selective laser sintering may be applied to almost any materials provided that the materials are available in the form of powder, tend to fuse with the applied laser heat [06] and difference of melting and solidification point is high. Selective Laser Sintering are versatile and widely adopted with respect to extensive variety of materials e.g. metals, ceramics, nylon, plastics, composites etc. [02], [03] as well as wide range of applications such as biotechnology, medical, electronics, automotive, aerospace etc. [01], [03], [04]. A wide range of materials having high or medium fusion property, can be sintered as a single material. Sintering of powder materials having low fusion can be performed by mixing or reinforcing with binder materials.

1.3.2 Lasers for Selective Laser Sintering

Selective laser sintering is significantly influenced by various types of lasers. A wide range of commercially available lasers are being used for the SLS process. From case studies, *Pinkerton* [03] reported that, for sintering process lasers of a power range of 1W to 6000W of wavelengths of 0.3547µm to 10.6µm are available commercially. For processing the thermoplastics 30W to 200W CO_2 laser is required and for metallic materials 50W to 500W CO_2 laser, 200W to 1000W fibre laser are commercially available.

Selection of appropriate laser, type, wavelength and other parameters are dependent on mechanical and thermal properties, composition and particle size of powder materials to be sintered. *Kruth el al* [06] reported in his case study about the lasers used in selectively laser sintering technique. Application of lasers are shown in Table 1.1

Table 1.1 Lasers used in Selective laser sintering of different materials

Laser Source:	Application on metals	Application on non-metals	Application on composite and alloys
CO_2 laser	Iron, Copper, Tin	Ceramics: Al_2O_3, SiO_2, SnO, CuO, ZnO, TiC, WC, SiC, Cr_3C_2 Polymers: Polymethylacrylate, Polytetrafluoroethylene, Epoxypolyether-based polymer	Cobalt alloys, Copper alloys, Nickel alloys, Iron alloys, etc. Mixture of Fe alloys and TiC, Ni alloys and Epoxypolyether-based polymer
Nd:YAG laser	Iron, Copper, Tin, Lead		
Diode Laser	Copper, Aluminium and Anodised Aluminium	Ceramic, Polymers	Stainless Steel
Diode pumped solid state lasers	Copper, Iron, Aluminium, Silver, etc.	Polymers	Copper alloys, Nickel alloys, Iron alloys, etc.

1.3.3 Potentials and Limitations of Selective Laser Sintering

Almost all the additive manufacturing methods produce parts with porosity which is undesired. In Selective Laser Sintering also the produced part exhibits changing degrees of inherent porosity due to the distinct nature of layered manufacturing. Local porosity is imparted due to selectively laser scanning and discrete bonding of individual particles or neighbouring particles. Porosity is generally an undesired property, which causes decrease in part integrity. However, there are several emerging or potential techniques of controlling porosity. It can be reduced by using proper graded composite materials during SLS of composite materials.

In review of literatures, it is observed that SLS can be enforced for a propagative build-up of workpiece of customised profile to regulate different micro-mesoscopic physical properties e.g. density, porosity and also crystalline structure. There are limitations w.r.t. the particle size used in SLS. The limitations are dependent on grain size of powder materials. To overcome these limitations, three alternatives can be chosen.

(a) *Use of multi-materials:* Sintering can be done by using the mixture of multiple materials having different melting temperatures. The mixture can be prepared by mixing the material which will be sintered and another material of lower melting point. The material with lower melting point acts as a matrix. Other material acts as reinforcement. It is known as Liquid Phase sintering. *Kruth et al* [07] explained in detail about sintering of multi material mixture in SLS.

(b) *Mixture of powder of different particle size:* Sintering can be done by mixing the powders of different particle size. The smaller particles bind the larger particles. The smaller particles act as a binder. The porosity of the sintered part can be reduced by this method.

(c) *Use of submicron sized powder:* Sintering process using the submicron sized powder (grain size is less than 10μm) will help to reduce the porosity level as well as to achieve the minimum feature size in SLS.

During SLS of submicron sized metal powder researchers faced several challenges in powder coating, balling effect which are still not resolved successfully [07], [08], [09]. With the efforts of few researchers some alternatives are observed to minimize the difficulties. *Regenfuss et. al.* [09] demonstrated use of hollow cylindrical coating rake which works like a blade to spread powder as well as storage of powder. To overcome the balling effect, use of binder material is demonstrated by *Regenfuss et. al.* [08], [09]

1.3.4 Sintering Mechanisms

The surface atoms of the powder particles are diffused during process of sintering. Interatomic potential gradient is responsible for the atom diffusion from the boundaries of the powder particles. Neck formation is the major phenomenon of sintering [10], [11]. Different pathways are followed by the atoms during dislocation and to initiate formation of neck. Six common mechanisms of sintering [12] are shown in Fig. 1.4. These mechanisms are explained in Table 1.2. The diffused atoms are sunk to the neck formed between the particles.

Table 1.2: Six common mechanisms of sintering [12], [14]

Sl. No.	Source	Sink	Path of Transport
1	Surface	Neck	Surface diffusion
2	Surface		Vapour Transport
3	Surface		Lattice diffusion from surface
4	Grain Boundary		Lattice diffusion from grain boundary
5	Grain Boundary		Grain boundary diffusion
6	Bulk dislocation of atoms		Lattice diffusion

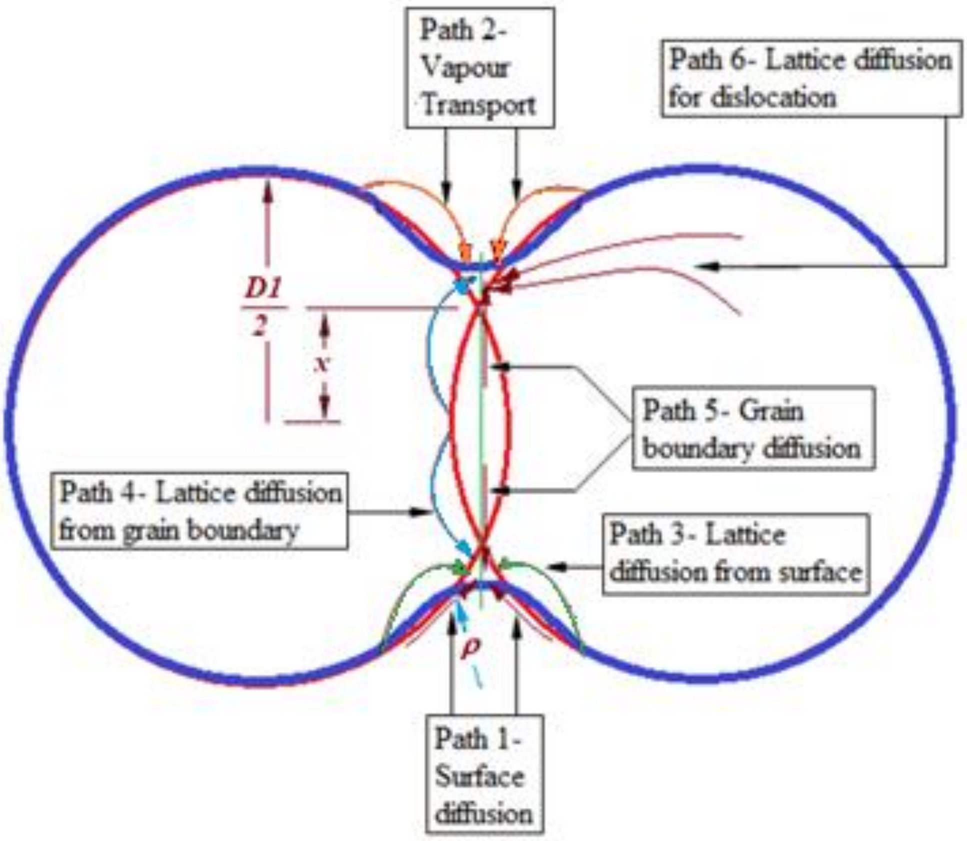
Path 2- Vapour Transport
Path 6- Lattice diffusion for dislocation
D1/2
x
Path 5- Grain boundary diffusion
Path 4- Lattice diffusion from grain boundary
Path 3- Lattice diffusion from surface
ρ
Path 1- Surface diffusion

Fig. 1.4 Sintering Mechanisms

In sintering process, atoms follow different paths during displacement from their positions. The surface atoms displace to another surface or to different location on the same surface. Redisposition of grain boundary atoms results porosity between the particles. Bulk movement or movement of massive number of atoms also take place towards the pore surfaces. This bulk atom movement may eliminate porosity and increase the density of the sintered part. Continuous change in centres of mass of the nanoparticles occurs during sintering process. The centre distance of the nanoparticles decreases during condensation due to densification and shrinkage. Fig. 1.4 shows different atom movement paths during neck formation.

1.3.5 Mechanism of Neck Formation

Neck is initialized shortly after heating starts due to laser irradiation and the neck grows slowly. *Y. I. Frenkel* established the physical theory of sintering [13], [14]. Fig. 1.5 shows the steps of neck growth. Because of high temperature, movement of atoms across grain boundaries takes place. *Frenkel* stated that "Surface stress can cause viscous flow in crystal materials; and sintering of crystal materials can be explained by that phenomena" [13], [14]. *Frenkel* explained that neck formation and growth of neck during sintering occurs as a result of viscous flow caused by surface stress. The fused particles come in contact like liquid droplets and later gradually contact surface increases to grow neck.

The stages of neck formation in SLS are shown in Table 1.3 [12], [14].

Table 1.3: Stages of Neck formation

Stage	Name of Stage	Description
0	Instantaneous	Powder particles come into contact which results instantaneous neck formation. *M. F. Ashby* introduced this stage called zero stage. [12]
1	Early stage	Diameter of neck increases with heating time
2	Intermediate stage	Diameter of neck become quite larger and roughly cylindrical pores become visible
3	Final stage of neck formation	Maximum diameter of neck is achieved. Isolated and spherical shape of pores are created.

Fig. 1.5, reveals that all the six sintering mechanisms (shown in Table 1.2) are responsible for neck formation and densification occurs due to mechanisms 4, 5 and 6. Small gap is

being kept initially between the pair of particles (shown in Fig. 1.5(a)). Later when heating is started, the particles come in contact and instantaneous neck formation starts (shown in Fig. 1.5(b)). The intermediate stage of neck formation is shown in Fig. 1.5(c). Neck diameter slowly increases due to viscous flow of fused material of the surface of the particles (shown in Fig. 1.5(d)). In the SEM image (Fig. 1.6) of selectively laser sintered 5µm copper powder, fully grown neck between two copper powder particles are clearly visible.

During sintering, due to the above mechanisms rearrangement of grain boundary atoms takes place. As a result, porosity occurs. Porosity in sintered part is one of the limitations of sintering process. Fig. 1.7 shows the schematic diagram of empirical steps of development of porosity during sintering. SEM image of selectively laser sintered 5µm copper shows the porous areas developed during SLS (Fig. 1.8).

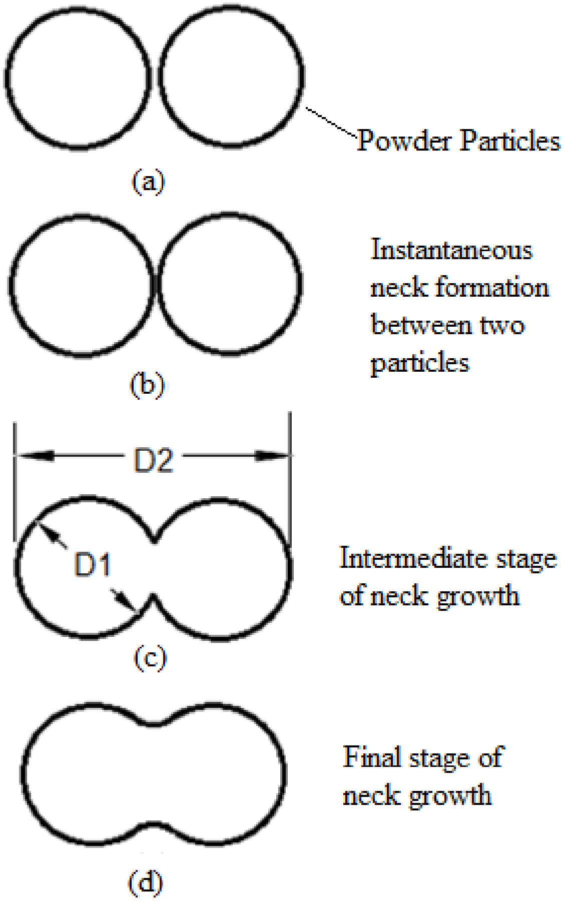
Powder Particles
(a)
Instantaneous neck formation between two particles
(b)
D2
D1
Intermediate stage of neck growth
(c)
Final stage of neck growth
(d)

Fig. 1.5: Schematic of stages of neck formation between two particles during selective laser sintering

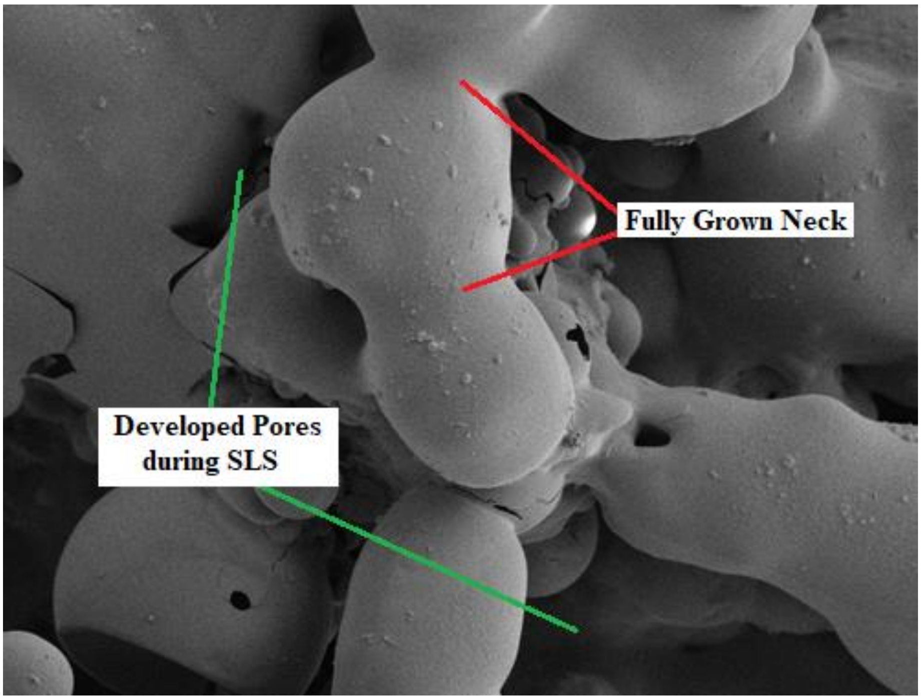
Fully Grown Neck
Developed Pores during SLS

Fig. 1.6: SEM micrograph of neck growth during selective laser sintering

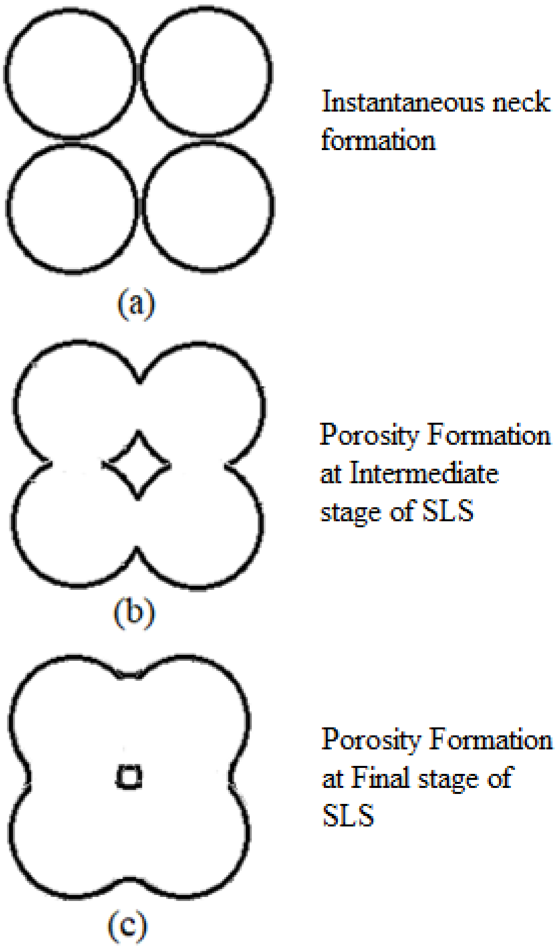
Instantaneous neck formation
(a)
Porosity Formation at Intermediate stage of SLS
(b)
Porosity Formation at Final stage of SLS
(c)

Fig. 1.7: Schematic for porosity between the particles during Sintering

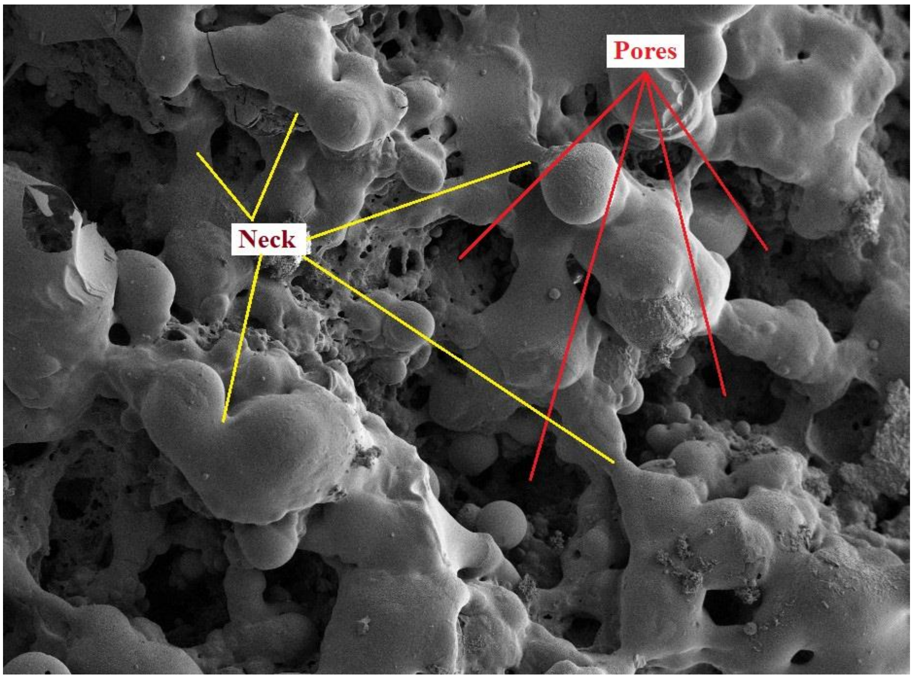

Fig. 1.8: SEM image of formed pores between particles during SLS

1.3.6 Binding or Consolidation Mechanisms

During the process of Selective Laser Sintering, due to confined heating using laser beam the powder particles get defused and then solidified after removal of laser beam. *Kruth et al* [15] reported the dominant consolidation mechanisms after surveying several cases. Fig 1.8 depicts the classification of Binding or Consolidation Mechanisms.

a) **Solid State Sintering:** During Solid State Sintering, powder particles are heated below the melting temperature of the materials. In Table 1.2, atom diffusion mechanisms and neck formation are shown. During Solid State Sintering, surface diffusion and diffusion of grain boundary occurs and diffused atoms are displaced towards the neck between the neighbouring particles. This consolidation mechanism is very slow and is not suitable for high scanning speed. This mechanism is suitable for consolidation of ceramic materials, also often applied for those materials which require post processing [15].

b) **Liquid Phase Sintering – Partial Melting:** During this sintering process some of the powder particles are melted and some remain solid for the same time duration of heating. In this process solid phase as well as liquid phase coexist. During this process the molten material spreads into the void parts among the solid particle due to capillary forces and afterwards it gets solidified. In this process mixture of different powder materials are used. Among them some of the material has low melting temperature and some has high melting temperature. After application of heat, lower melting temperature material melts and another material does not reach the melting temperature. These low melting point material works as a binding material in this process. Currently liquid phase sintering is one of the popular consolidation mechanisms. To improve novel method of manufacturing, challenge of single component liquid phase sintering is taken up by the researchers.

c) **Full Melting:** During Full Melting consolidation mechanism powder particles get fully melted and form a dense structured part [07]. Produced parts does not require any post processing. Laser beam with high energy density is applied during Full melting process. The only advantage of this process is to develop a part with high density. There are limitations of this process – due to high intensity of laser and high temperature gradient shrinkage occurs during consolidation which leads distortion of part [16] and balling effect phenomenon during laser scanning leads to poor surface finish. To minimize these limitations severe control over process conditions is required.

d) **Chemically Induced Binding:** Chemically induced binding is commercially quite popular in the Additive Manufacturing technique. Presently, this binding mechanism becomes feasible in the SLS of metals, polymer and ceramics. *Kruth et al* [15] reported that chemical binding has been applied by researcher during SLS of ceramic as well as metallic material. Binder materials are used in many forms – binder material in powder from mixed with basic powder material before laser scanning, sometimes basic powder particles are coated with binder material, another way out is blending liquid binding materials with the basic powder materials. Polymer materials are commonly chosen as chemically induced binders as they are highly viscous, low surface energy, low thermal conductivity and less reactive with other elements. These properties help to retain the liquid phase of metallic materials for longer time and binding with neighbouring particles become stronger. Due to the viscous property of chemically induced binders balling effect could be avoided and accuracy level of sintered part increased. During post processing at high temperature, binder material if required can be removed.

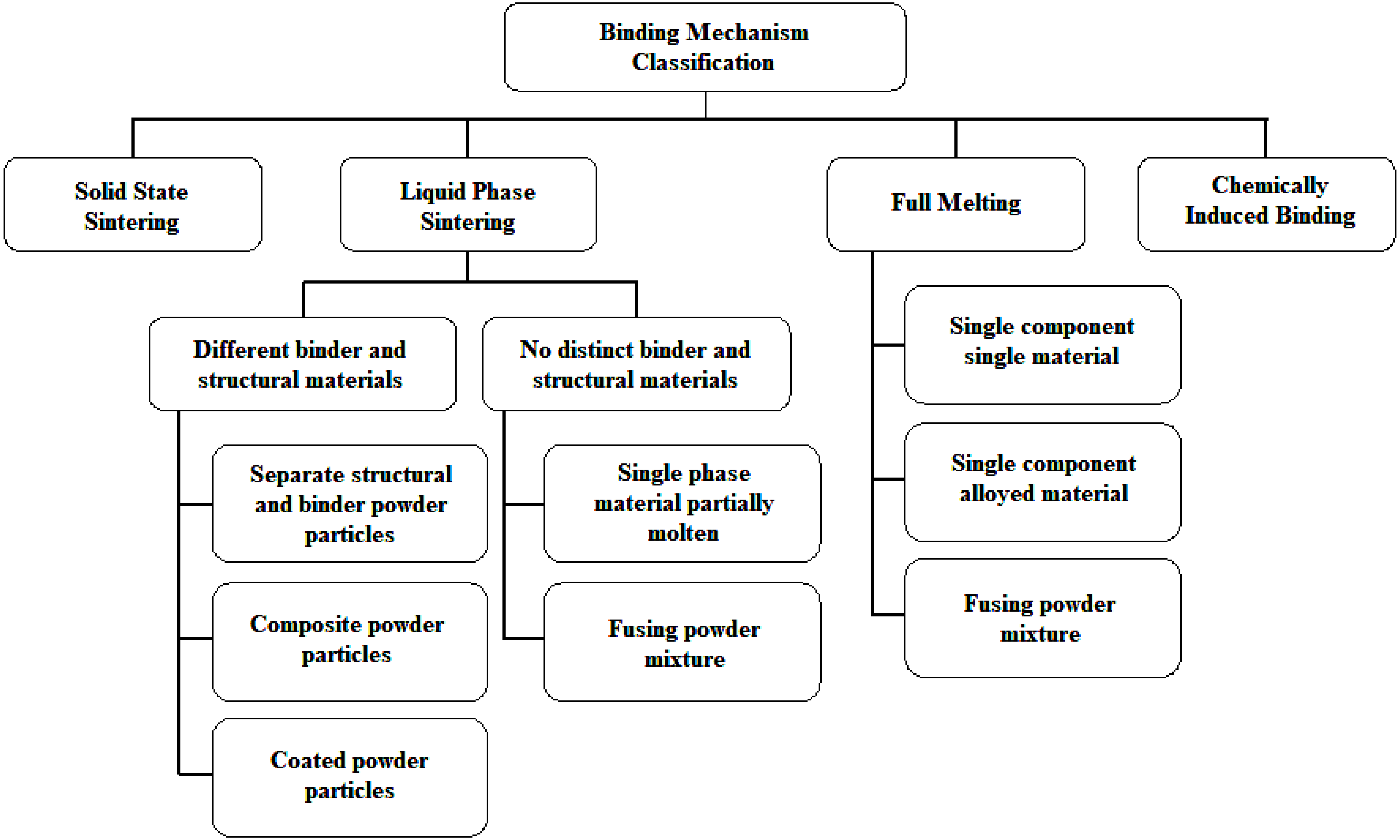
Binding Mechanism Classification
Solid State Sintering
Liquid Phase Sintering
Full Melting
Chemically Induced Binding
Different binder and structural materials
No distinct binder and structural materials
Separate structural and binder powder particles
Composite powder particles
Coated powder particles
Single phase material partially molten
Fusing powder mixture
Single component single material
Single component alloyed material
Fusing powder mixture

Fig. 1.9 Laser-based powder consolidation mechanisms [07]

1.4 Review of past research

So far multi-scale manufacturing capabilities paved pathways for development of intelligent micro-nano systems/devices, which have been finding their deployment in several real-time applications. This needs to be appreciated that economics of these developments largely depends on multi-scale manufacturing protocols within the industrial engineering attributes of responsiveness, reproducibility and cost. This still remains a major issue in micro-nano scale. This is largely attributed multi-material multi-scale manufacturing capabilities that lack technological maturity and standardization. The conventional lithography-based operations producing 2D features mainly over the silicon substrate. Integration of mechanical based processes such as micro-milling, micro-EDM, laser ablation etc. would enhance capabilities to produce 3D features over multi materials. While assuring repeatability, these processes lack limits in feature size and accuracy. On the other hand, micro injection molding could produce the micro plastic parts with complex geometry, but micro mold manufacturing is still an issue. In the current status, manufacturing of meso-micro parts having undercut features in micro scale having high aspect ratio will be a daunting task.

In the segment of component manufacturing, Sintering is well recognized and traditional fabrication process. In earlier stage it was popular in preparing earthenware. Advancement of sintering technique started in eighteenth century and continued to nineteenth century with the use of various simple metals and non-metals. In the early twentieth century, the empirical sintering technique is employed with the harder metals and metal alloys. In 1980s computer assisted laser apparatus was used to selectively sinter powder layers. At the end of twentieth century Selective laser sintering (SLS) started its journey as a novel technique of Additive Manufacturing. Few literatures of Selective Laser Sintering are reviewed and explained briefly in the following aspects:

(1) Theoretical aspects of SLS; (2) Alternative Materials used in SLS technique; (3) Selective laser sintering of Micro scale powder materials; (4) Process Optimisation of SLS technique; and (5) Application of SLS

1.4.1 Review of literatures on Theoretical aspects of SLS

German [17] demonstrated the history of sintering. He reported from archaeological evidences that sintering of minerals like ceramic objects which were found in different parts of the globe, were prepared approximately 26,000 years ago. He also reported that sintering of ceramic particles was popular for manufacturing several artefacts before 1700 A.D. He also reported the records of sintering of metallic materials using trial and error approaches exist between 1700 and 1900 A.D. In early 1900's, use of sintering techniques for hard materials and metal alloys are evident. After 1940's mathematical models of sintering were developed to understand neck growth, densification, shrinkage etc. In 1980's analytical computer models of sintering were developed.

Ristic [12] has demonstrated about contemporary concepts and mechanisms of sintering and its future in his book, named "Science of Sintering". Movement of mass across different position of the particles are demonstrated with the help of six different mechanisms and stages of neck growth between neighbouring particles during sintering. He discussed phenomenology in the science of sintering and roles of defects in sintering process. He also discussed about the change of thermodynamic properties during sintering and instantaneous creep and plastic deformation of the particles.

Kumar [18] has reviewed various literatures and explained about materials, binding mechanisms, experimental procedures and effects of processing parameters during SLS. He appreciated SLS as it got great attention from researchers. He also reported that promising results can be formulated by optimizing various process modelling and experimental strategy.

Dong et al [19] developed transient three-dimensional finite element model to simulate phase transformation during SLS process. They considered no phase change effect in the model. In the experimental study they analysed the effect of different parameters, like scanning speed, intensity of laser, preheating temperature, laser beam spot size, etcetera. They compared their predicted results with experimental results and found good agreement for density distribution.

Glardon et al [20] investigated the effects of different process parameters of Nd:YAG laser on SLS of metallic powder for improvement of sintering. They found that Q-switching of Nd:YAG laser offer wider range of laser parameter than CO_2 laser sources due to short pulsed energy delivery. They found that in pulsed mode consolidated sintered part is more dense than the mode of CW due to pulse repetition rate of pulsed mode.

Gusarov et al [21] studied powder bed contact thermal conductivity during SLS. They proposed model for independent small thermal contacts to determine effective contact conductivity. Their proposed model demonstrates that the effective thermal conductivity is proportional to the linear dimension of the contact.

Paul and Anand [22] stated that SLS technique is viable for wide range of materials, metal, polymer and ceramic powder materials can be sintered using laser power. They presented numerical analysis of essential laser energy for producing simple parts via SLS technique. They concluded from the results that slice thickness is inversely proportional to overall laser energy for producing the laser sintered part and the effect of orientation of the part is dependent on the part geometry.

Qian and Shen [23] reviewed several research articles on growth of laser sintering of ceramics focused on the principles and the potential of this novel technique of additive manufacturing. They explained about the technique of laser sintering, laser and ceramic powder material interactions, laser scanning strategy etc. They could reveal that laser sintering is a viable for producing complex shaped customised 3D parts, in a single production operation, which could hardly be prepared by traditional manufacturing processes.

Senthilkumaran et al [24] investigated the shrinkage compensation during SLS for improvement of accuracy level of sintered part. They developed shrinkage model of SLS of powder particles and optimised the several laser parameters (like power, scan speed, hatch spacing, part bed temperature) using experimental empirical relationship. To obtain relationship they used Taguchi method for designing and conducting experiments. From experiments they found that shrinkage factors became flexible with the help of empirical relationships.

Fischer et al [25] conducted experiments of SLS of pure titanium powder with pulsed Nd:YAG laser to understand the process. They simulated heat flow with a numerical model to compare with experimental data and they obtained a process map. They experimentally identified and confirmed three important repetition rate domains with respect to heating effects and pulse energy, (a) at higher range, pulse effects are not so strong to produce liquid, which leads to higher average temperature, (b) in lower range, liquid is produced in each pulse, in which average temperature remains low, (c) in the intermediate range creates optimum processing space with limited plasma effect due to quick and local heating.

Regenfuss et al [08], [09] performed several sintering operations on different metallic and ceramic powder materials using q-switched pulsed and continuous wave mode laser sources. They established the effect of laser sources on sintered part. They found significant effect of laser energy sources on rapidly heated and cooled sintered parts. High geometric resolution can be achieved during sintering of metal powder.

Ristic and Milosevic [13] presented the theoretical representation of Frenkel's theory of Sintering. They demonstrated the neck growth mechanism during sintering in analytical approach with the help of Frenkel's model. He also demonstrated rate of shrinkage with respect to time and porosity formation. Y. I. Frenkel explained in his theory of sintering that neck formation during sintering occurs due to viscous flow influenced by surface stress.

Li et al [26] discussed about the challenges in laser nanomanufacturing technologies to produce 3D nanostructures through additive manufacturing techniques. They found that laser based nanomanufacturing is advantageous in narrow size distribution. They also stated that laser nanomanufacturing is relatively new, rapidly growing and promising technique in the field of manufacturing of nanofabrication.

Daw et al [27] proposed an interatomic potential which is known as Embedded Atom Method (EAM) potential to simulate models at atomistic levels. EAM potential is a derived expression based on density-functional theory. This potential deals with total energy. The total energy is obtained from the embedding function which is the sum of embedding energy in the electron density. Using developed model, they found out ground state properties of metallic materials which have agreement with experimental data.

Richardson et al [28] investigated and explained the capability of EAM model simulation of the equilibrium and non-equilibrium behaviour of metallic materials to produce alike values of re-growth velocity as experimentally obtained. They also noticed that on ignoring the contribution of free electron towards transport property, shows quantitatively accurate results.

Johnson [10] developed a mathematical model of sintering to find coefficients of volume diffusion, surface diffusion and grain boundary diffusion during neck growth in sintering. He determined grain-boundary and volume diffusion coefficients from quantities of instantaneous neck geometry and interpretation rate of pair of particles on mutual axis of rotation for circular neck formation. He also stated that with the appropriate geometric assumptions, measurements of shrinkage and neck size are possible.

Pan et al [29] employed Molecular Dynamics simulations for comparing the process of neck growth by heating gold nanoparticles using continuous laser. They compared the results of Molecular Dynamics simulations with the proposed analytical model by *Johnson* [10] for heating with continuous laser. They revealed nearer concurrence with particles more than 10nm nanoparticles.

Yang et al [30] also performed Molecular Dynamics simulations of 4nm to 20 nm gold nanoparticles to investigate effect of particle size and laser intensity on neck growth. They noticed that the decelerating heating rate takes more time to reach to the ultimate temperature. Due to this reason the neck becomes wider. But if the heating rate increases, melting phenomenon occurs. This is resulting subsequent increment in neck width. Mean Square Displacement (MSD) decreases with increment in particle size. A reverse effect on the radius of gyration occurs which is not affected by heating rate and the particle reaches to melting point at the last stage of sintering.

Jiang et el [31] analysed the sintered hollow silver nanoparticles structure. They have developed fruitful sintering models for FCC structured metals such as Au, Cu, Ag, Al and performed Molecular Dynamics simulations to correlate traditional theories with experimental data.

In consequence of micro-nano scale systems engineering, the demands of customised complex geometry microparts manufacturing have been increased. Past literatures reveal that the researchers are showing interest of using submicron range of size of particles in the arena of Selective Laser Sintering. But still the use of submicron particle is in the stage of research and development. In the cases of laser sintering of submicron sized powder, it is observed that the particle size is lower than the laser beam spot diameter. Practical experiments of the joining process of metal nanoparticles at the atomic level in the laboratory is very tough and expensive. Nevertheless, these process mechanisms may perhaps be modelled and simulated using Molecular Dynamics (MD) simulations for more honest understanding and operation improvement. The MD simulation method is chosen as it took to investigate dynamic properties of the sintering operation.

Recap of past researches reveals that the researchers have employed Molecular Dynamics simulation to explore the interaction between laser-material and magnificently simulated the neck growth phenomenon during the various stages of sintering and subsequently reduces on the culmination of the sintering.

1.4.2 Review of literatures on Alternative Materials used in SLS

Wang et al [32] conducted simulation as well as experimental studies of laser sintering to produce 3D hard metal part using Nd: YAG laser at various power levels up to the orbit of 8.18W to 28.1W and scanning speed in the range of 3mm/s to 25mm/s. They have compared simulation data with experimental data. Their investigation was focused on sintering of powder mixture of hard metal powders like tungsten carbide–cobalt (WC-Co). They investigated the effects of different processing parameters, viz. scan speed, laser power, hatch spacing, grain size, proportion of powder mixture, and shapes, on mechanical properties of produced parts. They demonstrated that WC-Co mixture could be processed in a broad range of process parameters compared to Fe-Cu mixture due to better absorption properties of WC-Co.

Salmoria et al [33] analysed the effect of hydroxyapatite (HA) on mechanical properties and microstructure of producing parts by SLS of the functional graded scaffold of HA (of particle size 5–10µm) reinforced high density polyethylene (HDPE) of particle size range 150–212µm. They found that the scaffold specimens were with a pore diameter range of

30–180 µm and a porosity range of 45–48%. They also found that the modulus of storage of the composite scaffolds decreases with the rise in hydroxyapatite (HA).

Gu and Shen [34] performed experiments to investigate on direct laser sintering of WC-Co and Copper composite. They studied the microstructure of laser sintered parts to find the effects of WC-Co on microstructural properties. They successfully produced laser sintered part using WC-10%Co reinforcing copper matrix composite and found great interfacial bonding between the reinforcement and the matrix. They obtained high average microhardness of the sintered part using 30 wt.% WC-Co.

Nakamoto et al [35] prepared selectively laser sintered part of alloyed steel powder and for hardening the sintered layer they plasma nitrided in N_2-H_2 gas mixture at 773K or 823K temperature. They found hardness of the plasma nitrided samples at 773K and 823K were about 680HV and 600HV respectively, whereas hardness of original SLS part was found about 330HV. They compared mechanical properties of nitrided and non-nitrided parts with the help of optical microscopy, XRD, GDS and micro-Vickers hardness test. They investigated and found better properties in nitrided part.

Singh et al [36] studied the microstructures and measured mechanical properties of the cross-section and top surface of selectively laser sintered $Al_{50}Ti_{40}Si_{10}$ composite powder. They prepared sintered sample by scanning 50–100µm size powder particles using continuous wave CO_2 laser with power 350W and scan speed 15mm/s in Argon environment. After experimental investigations they demonstrated that sintering and hardness improvement was effective up to a depth of 200-400µm. They also compared experimental data with predicted analytical model data and found better comparison.

Simchi et al [37] investigated liquid phase laser sintering of iron-based powder mixture. The powder was consisting of iron, carbon, copper, molybdenum and nickel. They found the sintered density was influenced by shape, size and distribution of powder particles. They also noticed that optimised carbon content significantly decreases the viscosity and surface tension of molten iron, whereas copper content works as a bonding material for iron particles. They also noticed that Molybdenum and Nickel helped to improve the mechanical properties.

Zhu et al [38] investigated the shrinkage behaviour of Copper based laser sintered powder. They theoretically explained and analysed the sintering shrinkage and thermal shrinkage. They conducted experiments of sintering of powder mix of Copper powder and S-Cu-P powder in the weight ratio of 60:40. They also created a hypothetical model to clarify the in-plane expansion. They calculated shrinkage in different processing parameters like laser power, hatch spacing, scanning speed and layer thickness. They observed the shrinkage in all directions, but shrinkage in the direction of height is maximum. They described the causes of in-plane shrinkages – cause of sintering shrinkage is densification; cause of thermal shrinkage is change in temperature. They also reported expansion due to structural particles fall.

From literatures of previous researchers this can be summarized that Selective Laser Sintering of metallic powders is roughly classified into two categories on the basis of material used – (1) single material and (2) multi-material. During SLS of single material powder particles, binding between particles take place due to partial melting of the powder particles. Due to this understanding, the process needs strict control over the processing parameters. Whereas in the case of SLS of multi-material, binding of powder particles occurs due to full melting of powder particles of low melting point in concoction of multiple materials of different melting points.

1.4.3 Review of literatures on Selective laser sintering of Micro-scale powder materials

In current research integration of selective laser sintering (SLS) of submicron scale metallic powder to produce 3D parts is explored. Investigation has been carried out on issues associated with several aspects of laser sintering metal powder having <10µm particle size, which is yet commercially not viable. This research focus on reasoning multi viewpoint, including requirements of substrate (supporting base plate), consistent coating of submicron size powder in each and every layer, laser-metal interactions at micro scale, metallurgical and morphological investigations, requirements and techniques for post sintering and finally the handling these micro-sintered parts. At the beginning of twenty first century researches on Selective laser sintering (SLS) of submicron scale powder material started its journey.

The journey of approximately two decades of SLS of submicron scale powder is reviewed and explained briefly as following.

Regenfuss et al [08] reported in their paper that, use of controlled atmosphere, and use of sub-micron size powders to reduce the feature resolution of SLS process up to 10µm has been employed in early 2003. They [09] demonstrated the unique advantages of q-switched pulsed Nd-YAG lasers to sinter sub-micron powder with a feature resolution as small as 30µm. They found that resolution of generated structure with q-switched pulsed Nd-YAG lasers was better than which was achieved with other laser sintering methods. They also found that it was difficult to handle the properties of powder materials during coating. They [39] studied the mechanisms in laser micro sintering for metallic materials and ceramics. They explained the fundamentals of the hypothesized specific process mechanisms.

Ebert et al [40], *Exner et al* [41], *Exner et al* [42], *Regenfuss et al* [43], *Petsch et al* [44] aimed to sinter micropart made of mixture of copper and tungsten in the range of dimension of 20µm using SLS technique. They obtained structure in resolution of 30µm. they found the surface roughness of the produced parts as R_a = 5µm (horizontal), R_a = 3.5µm (vertical) and R_a = 7µm (separation cross section). They produced micro-freeforms from different metals applying a special laser sintering regime.

Exner et al [45] studied the process mechanism of micro laser sintering to produce metal and ceramic parts using submicron sized powder particles. They reported basic differences between selective laser sintering and micro laser sintering. They reported that this process could be applicable for the submicron particle size range up to 10µm. They observed the best resolution in the range of 50µm for ceramic materials and in the range of 15µm for metallic materials.

Ebert et al [46] investigated the function of power, pulse interval of laser and vacuum level during micro sintering of tungsten powder. They studied the morphology of sintered structure. They observed a complete built up sinter structure with low density and visible cracks, with a laser power of 0.8W, with pressure 500mbar, 45µm of pulse interval. They reported that on density of sintered part depends on power and pulse interval of laser and pressure.

Regenfuss et al [47] discussed methodology and approach to fabricate micro tools of submicron sized metallic powder, using laser micro sintering technique in controlled laser pulse. They could develop micro tools of overall structural resolution of 30µm. *Regenfuss et al* [39] studied thermo-mechanical effects on micro laser sintering of ceramic powder with the help of the reaction models. They presented mechanistic hypotheses based on the perceptions obtained from micro laser sintering of different metallic and non-metallic materials. They reported that micro laser sintering of metals processes is initiated by high laser intensity radiation with pulse times of 10-100µs.

Streek et al [48] aimed to improve sinter resolution and density of sintered powder layer during micro laser sintering of metal with the application of high-intensity q-switched pulsed laser. They observed that sinter densities above 90% result from sinter regimes. Sintering of lower dense powder layers lead to either balling phenomenon or excessive ablation. They found that within the pulse regimes dense structure of sintered part could be achievable.

Streek et al [49] aimed modification of micro laser sintering. They developed upgraded coating technique to improve compaction of powder before sintering the powder layer with chosen suitable laser regimes. With the help of upgradation, they achieved higher density in micro sintered part. They reported that micro laser sintering of adequately controlled compacted powder layers, with continuous laser irradiation might be feasible. They observed sintering with new regime i.e. pulse energy 57µJ, peak intensity 5×10^7 W/cm^2, pulse per area 30.8×10^3 cm^{-2} and sinter density ≈90%. They renamed the technology as "high density-laser micro sintering" (HD-LMS).

Chen et al [50] prepared micro laser sintered 3D part and investigated micro selective laser sintering. They explained about Micro Laser Sintering system which was developed for experiments. They developed a powder feeder to feed micro-scale powder. They optimised the various laser parameters and successfully built 3D parts using micro-laser sintering technique at laser power of 35W fiber laser. They prepared four rings of wall thickness of 100 microns and height 2mm. Smallest diameter of the samples was less than 1mm. They sintered the micro-scale powder selectively using laser beam of focus diameter of 10µm.

Paul et al [51] studied kinetics of sintering of submicron scale cobalt powder. They sintered submicron sized powder of size 23µm, 18µm and 12µm average grain size separately using conventional sintering technique. They observed little shrinkage at lower temperature before starting of actual sintering. They found that grain boundary diffusion, lattice diffusion and viscous flow are the three most leading sintering mechanisms. From SEM analysis the found consistent microstructure of sintered parts.

Shirazi et al [52] reported in the review that, selective laser sintering is one of the powerful and versatile technique of additive manufacturing. They found that, research on SLS of on more than 10µm powder particle is available. They reviewed the effect of layer thickness on average pore size during SLS. They reported that, average pore size increases with layer thickness. They also reported that microstructural and mechanical properties of laser sintered parts are influenced by material characteristics and process conditions like energy density of laser, temperature of powder bed, thickness of powder layer, scanning speed and hatch spacing.

Shishkovsky and Scherbakov [53] studied selective laser sintering of biopolymers with micro and nono ceramic additives. They selectively laser sintered 50µm average sized polymer with 20 – 80 µm sized ceramic powder with ceramic-polymer wt. ratios of 1:1, 1:2, 1:3, 1:4 and 1:10. From study of microstructures, X-ray structural analysis and EDS they found no significant modifications. They recommended the samples for steam cell study and proved to be successful for medical tests.

Streek et al [54] developed 3D powder model to investigate energy conversion in approach of estimation of powder layer thickness during laser sintering of micro-scale molybdenum powder. They prepared 3D model of particle sizes of 2µm, 3µm, 5µm, 10µm and studied energy absorption to optimize layer thickness. They found that (a) sintered layer is adequately fused to underlying layer in case of 8µm thick powder layer, (b) sintered layer is giving indication of poor fusion to the bulk in the case of 16µm layer thickness and (c) sintered layer showed almost no fusion at all in the case of 32µm thick layer.

From the review of several literatures of previous researchers, it is observed that SLS technique has ever increasing demand in the field of manufacturing of highly customised complex geometry product. The literatures of past researchers also revealed that SLS technique in the submicron range i.e. less than 10µm particle size is still under research and development. In previous researches integration of selective laser sintering (SLS) of submicron scale metallic powder to produce 3D parts is not much explored. Very less investigation has been carried out on issues associated with several aspects of laser sintering metal powder having less than 10µm particle size and it is still commercially not viable.

1.4.4 Review of literatures on Process Optimisation of SLS technique

Ghita et al [55] studied to investigate SLS of used and unused polyether ketone (PEK) powder. They conducted laser sintering experiments at high temperature. They demonstrated that better quality products can be produced by optimizing process parameters. From the optimised experimental data and they reported that, tensile strength reduced by 17% when 30% of used PEK incorporated.

Dai et al [11] conducted the preliminary experiments of selective laser micro sintering to produce 3D micro metallic part. They performed a theoretical analysis of characteristics of wetting, capillary force and viscosity during selective laser micro sintering. They used the copper based metallic powder consist of Cu and CuP alloy for selective laser sintering. With the hatch spacing of 0.05mm and scanning speed 10mm/s they scanned the metallic powder mixture of Cu (of two different particle size of 150µm and 75µm) and CuP alloy (of mean particle size of 45µm), using 50W continuous wave Nd:YAG laser. They found results showing the mechanism of laser micro sintering and the significant effects of various processing parameters on the characteristics of the sintered part. They also found that CuP alloy powder played an effective role as a binder as its melting temperature is low and small scan spacing gave dense microstructure.

Das et al [56] performed experiments on direct SLS of cobalt and nickel-based superalloy materials. Their research was focused on investigating the effects of various composition of materials and process conditions on mechanical properties and solidification microstructures; to optimise process conditions to minimise defects; to demonstrate the reusability of unprocessed materials to minimise cost. They successfully developed direct selective laser sintering process for nickel and cobalt based superalloys, saved cost by eliminating some process steps and achieved greater microstructure and properties.

Kathuria [57] investigated microstructure of laser sintered part using methods of one metal component (single melting point), and two metal components (of different melting points). In all the methods he performed experiments with pulsed Nd:YAG laser (2W to 20W). He achieved about 221μm wide line with single metal component and about 470μm wide line with two dissimilar metal components. He reported different observations in microstructure of these cases. In SLS of one metal component, neck formation is visible but due to uncontrolled thermal effects some damages spots are also visible. In SLS of two metal components, melting as well as sintering effects are visible and low melting point metal acts as binder.

Bae et al [58] performed experiments of SLS varying the laser beam spot diameter to find the measurement mechanism of beam spot size during SLS process. They obtained from the experiments that the laser beam spot diameter can be changed at SLS process. They also proposed the device by which beam spot size can be measured and the mechanism of measurement of beam spot is presented. They suggested a new sintering process in which digital mirror system can be applied.

Chang et al [59] demonstrated the potentials of producing selectively laser sintered porous silica with controlled porosity without using any polymer binding material. They observed improved laser absorptivity on silica by using carbon as dopant. They did not notice any such unwanted blend, which might affect the final properties. They could be able to build up well-bonded selectively laser sintered 3D porous silica with low shrinkage. They also reported that this approach of SLS is also applicable to build 3D porous ceramics.

Chivel and Smurov [60] reported that, slow manufacturing application is generally accountable for poor efficiency and surface quality SLS and optical monitoring is especially important for SLS to improve quality. They developed an optical system and integrated with SLS machine to monitor temperature during SLS. They measured temperature distribution during sintering using CCD camera using process monitoring based optical measurements and controlled maximum surface temperature in the laser beam spot using weblengths pyrometers. They optimised SLS process with high range of porosity by using online temperature monitoring during SLS.

Dürr et al [61] studied the application of layer-by-layer SLS technique to build up simple and complex geometry EDM electrodes. They performed sets of experiments of SLS of powder mixture of bronze and nickel to optimise process parameters such as sintering strategy, scanning speed and hatch spacing. They studied various factors, which influence the quality of EDM electrode, like process parameters (laser performance, scan speed, hatch spacing, scan strategy), subsequent treatment (withdrawing, infiltration, polishing), powder properties (composition, melting point, particle size and shape), laser source (wavelength, spot size, operating mode) and environment (humidity, atmosphere). They found that lower scanning speed gives closer moulded particles and better surface finish, hatch spacing plays an important role to maintain quality of sintered electrode.

Kasperovich et al [62] presented the correlation laser process parameters and porosity formation during selective laser melting of TiAl6V4 alloy. They investigated porosity by 2D and 3D methods to study the mechanisms and morphology of porosity formation. They studied various defects such as balling effect, cracks during laser scanning of TiAl6V4, alloy of Ti and Al. They mentioned cracks are mostly influenced by balling effects as well as inadequate melting of powder particles. They also mentioned that the pores created due to surface tension of molten materials.

Kwak et al [63] presented the optimized post process for laser sintered polymer part. They reported that the post process under high temperature increases the adhesion of powder particles. For optimization they developed a model of post process and tested by heating at 178ºC for the periods of 0, 10, 20 and 30minutes. They also conducted experiments of post process and compared and analysed both accuracy and tensile strength of products produced by SLS which is one of the Solid Freedom Fabrication (SFF) process.

Macedo and Hernandes [64] studied laser sintering of $Bi_4Ti_3O_{12}$ ferroelectric ceramics by CO_2 laser heating. They found that high density can be efficiently provided to $Bi_4Ti_3O_{12}$ by laser sintering and to achieve this high density 16 times shorter time is required than traditional sintering furnaces.

Ning et al [65] discussed the effect of geometric shape on accuracy due to shrinkage during direct metal laser sintering. They investigated the empirical relationship of percentage of shrinkage for different shapes. From several case studies they found optimized speed-compensation method for improvement the dimensional accuracy of fabricated prototypes. After studing different cases, they demonstrated that to increase dimensional accuracy, correct speed settings can be generated for various geometric shapes.

Read et al [66] studied and optimized the effects of various laser parameters such as power, scanning speed, hatch space during selective laser melting to minimize porosity. They adopted statistical experimental design to optimize the effect of process parameters and minimize porosity and cracks. They studied various parameters using ANOVA approach. After investigation, they studied the effects of scanning speed, laser power and overlapping of laser scan on porosity. They reported that porosity increases with decrements in laser power and the increment in scan speed.

Shaw and Dirven [67] investigated porosity and mechanical properties of selectively laser sintered Nylon. They compared selectively laser sintered part with conventional methods of casting, injecting moulding processes and found sintered parts are more porous and having poor mechanical properties. To improve mechanical properties, they presented novel approach of creating resin-impregnated composite structures to reduce porosity and improve mechanical properties.

Song et al [68] performed experiments to develop selectively laser sintered silica sand structure to investigate effects of various laser parameters like power, scanning speed, laser beam spot diameter, overlapping rate, ratio of powder mixture on the quality of sintering and sintered parts. They found the SLS technique is appropriate for developing smaller, single and complex geometry parts. They sintered powder mixture keeping laser power of 12W and beam spot diameter 3mm fixed, and other parameters as variable. Investigation of process parameters showed significant effect on accuracy and property of sintered parts; optimisation of process parameters can improve the quality of sintered parts. They reported that, post-sintering processes can improve strength of sintered parts by distributing binding materials uniformly.

Stichel et al [69] studied the mechanical properties of a selectively laser sintered polymer part. They conducted six experiments of SLS of polymers in different machines for Round Robin study. For Round Robin study the prepared samples for finding the effects of pore morphology on mechanical properties. They prepared eighteen samples i.e. three samples on each machine, in three build directions – (a) horizontal, (b) diagonal and (c) vertical. They also studied the pore morphologies with the analysis of microstructure. They observed that the pore-density and mechanical properties of sintered parts are affected by the process temperature.

Wei et al [70] investigated the influences of sintering time on microstructure of sintered porous Tantalum. They sintered the material for the time of 10, 20, 30, 40 and 50 minutes at 1250ºC temperature. They were aimed to investigate the effects of sintering time on the microstructure and porous characteristics of the material. They found that the effect of sintering time is significant on porosity and pore size of sintered porous Tantalum. They also observed rapid shrinkage of powder during early period of sintering.

Yan et al [71] and *Koo et al* [72] investigated the influence of particle size over pore size during sintering of ceramics and metal. *Yan et al* prepared porous spinel ceramics by using pore-forming *in-situ* technique from bauxite and magnesite to investigate the effect of particle size on strength and microstructure. They found that microstructure and strength strongly affected by particle size. *Koo et al* classified Fe-Cr-Al powder into 25-35µm, 35-45µm and 45-75µm and sintered them at different temperature of 1250ºC, 1300ºC and 1350ºC. They observed and recognized phases all the specimen in SEM and XRD, respectively. They observed with increment in sintering temperature from 1250C to 1350C for same particle size, porosity was increased from 34.7% to 36.3%. They also observed that with the increment of particle size from 25-35µm to 45-75µm for same temperature, porosity was increased from 56.4% to 63.2%. Both of them demonstrated that, particle size is another key parameter and it is found that the porosity increases with the increase in particle size.

From the literatures of previous researchers, various difficulties and limitations are found. Main complications observed are balling phenomenon, porosity formation, effect of various process parameters on neck growth and porosity formation, deformation in layers, internal and surface cracks etc. Focus of this literature review is to observe the effect of processing parameters on neck growth and to minimize porosity during sintering. The major influencing process parameters of the neck growth and porosity formation are laser power, scanning speed, hatch spacing, energy density and layer thickness. At higher laser power and lower scanning speed incident of laser energy increases which leads to liquid phase sintering. Amount and size of the pores can be minimised by controlling over the processing parameters. Lower scanning speed, small hatch spacing and higher laser power also tend to liquid phase sintering which results lower the porosity level.

Particle size of powder have a key role in reduction of porosity level. Sintering time is reduced with decrement in size of powder particles. Densification occurs due to neck formation at the contact points of neighbouring particles. Lower size powder particles tend to combine with each other to create balls, whereas larger size powder particle tend to separate – porosity in both the cases increase.

1.4.5 Review of literatures on Application of SLS

Das et al [73], [74] studied a hybrid technique of selective laser sintering and hot isostatic pressing (SLS/HIP) for Ti6Al4V alloys to combine the strengths of both processes. They studied mechanical properties and microstructure, and reported that SLS/HIP is equivalent to conventionally processed materials. They demonstrated that using SLS technique complex geometry customized components could be developed and directly post processed by HIP with equivalent characteristics as conventionally processed materials.

Duan and Wang [75] *demonstrated the potentials of application of selective laser sintering in the area of biomedical technology.* They found the versatility of SLS in the biomedical engineering field, especially in producing scaffolds of tissue engineering and drugs. They demonstrated the preferable materials in the biomedical engineering field and particles shape and size range as spherical particles of size range 10-150 µm.

Fina et al [76] demonstrated the versatility of the SLS technique in preparation of 3D printed orally disintegrating tablets. They aimed to study the feasibility of the SLS technique to produce new solid dosage procedures with quicker drug release characteristics. From the SEM micrographs they reported that overall porosity is increased with higher scanning speed and more porous structure can be achieved by fabrication through layer-by-layer approach. After investigation they reported that SLS is a viable and acceptable technique to develop modern medicine.

Hao et al [77] investigated the rapid production of customised implants for manufacturing scaffolds of tissues and bioactive implants by means of SLS of hydroxyapatite (HA) reinforced high density polyethylene (HDPE). They found the effect of scanning speed and laser power on sintering behaviour. They also found that SLS is a potential technique to produce HA-HDPE composite products and capable of giving suitable features for their application as scaffolds of tissues and bioactive implants.

Ji and Jiang [78], [79] studied microstructure and dielectric properties of laser sintered tantalum pentoxide ceramic. They found that dielectric permittivity was increased in laser sintered samples compared to furnace sintered samples. They also prepared laser sintered transparent tantalum pentoxide ceramic. They achieved quite good results in transparency and dielectric permittivity compared to conventional sintering methods. They expected that in electronic and optical applications, the novel transparent ceramic will be found as better application.

Kinzel et al [80] investigated the feasibility of using SLS technique to produce thick-film microwave components. They optimised properties of lased using DC parametric study. They demonstrated that the technique of SLS is one of the suitable techniques to prepare functional microwave components with thick-film performance.

Laoui et al [81] studied the effect of different processing parameters of laser sintering on the features of Ti dental implants. They developed a model of dental implants with the help of Ti powder of size 45µm and 200µm using SLS and SLM. They achieved porous structure of surface increases the bone-osseointegration and essential mechanical strength is provided by compact core. They demonstrated feasibility of laser sintering in preparation of Titanium dental implants.

Singh and Pandey [82] studied fitment porous polyamide scaffolds produced using SLS. They prepared CAD model of porous polyamide scaffolds using SOLIDWORKS and fabricated with biocompatible material polyamide using SLS technique. They experimentally found that the scaffold of required geometry was getting fit into the defected area of bone with appropriate pose size to develop bone cells, which can be produced using the SLS technique. They obtained up to 1.3%-dimensional deviation using SLS technique which is found to be within the acceptable tolerance.

Sun et al [83] aimed the investigation to upgrade the production rate with low porosity during scanning the layers of SS316L selectively with high power laser beam with high scanning speed. They stated that dense structure of SS316L parts was successfully built.

Yang et al [84] prepared pattern of complex shapes for investment casting of high impact polystyrene (HIPS) material using selective laser sintering. They found that selectively laser sintered HIPS is suitable for proper dewaxing process. Using this carbonization residues could be avoided. As with the help of SLS, 3D complex structures are developed, these types of laser sintered patterns found to be useful during investment casting.

Yuan et al [85] studied the mechanical, thermal and electrical properties of selectively laser sintered MWCNT/polymer composite powder. They proposed a new manufacturing approach to fabricate CNT composite powders and utilize them in SLS. They compared SLS process with hot-compression process to prepare CNT/polymer composite with electrically conductive segregated structure and found SLS more effective to produce electrically conductive complex geometrical structured composite products.

Review of past researches reveals several applications of selective laser sintering. A wide range application of SLS in the field of biomedical engineering is observed from the research papers. Many of the researchers appreciated SLS in building porous scaffolds of tissue engineering and drugs. Researchers mentioned that SLS is one of the suitable techniques to build 3D complex geometry porous structure of bone tissues and bone surfaces with appropriate mechanical strength. Researchers also claimed that SLS is a versatile technique to produce orally disintegrating tablets with proper porosity. This technique is also feasible to prepare various dental implants. Porous sintered structure of tantalum pentoxide ceramic to increase dielectric permittivity. SLS found feasible to produce thick-film microwave components.

1.5 Objectives of Present Research

After review of literatures objective for the present research has been determined. The main objective of this doctoral thesis is to investigate neck growth mechanism between neighbouring powder particles during selective laser sintering (SLS) of submicron scale metallic powders i.e. less than 10µm and to investigate how porosity level be minimized by using submicron size powder during SLS.

Layer-by-layer powder grains are selectively scanned by irradiation of laser beam. The heated powder grains are consolidated by fusing the outer surface of granules, but not by melting. The review of past literatures reveals that the selective laser sintering of macro to meso scale powder particles is recognized widely. SLS of submicron-scale powder material is still under research and development. Compared to other techniques of Additive Manufacturing, SLS is one of the novel and popular techniques to produce 2D and 3D micro structures with complex geometry. However, wide-range review of previous research works has been completed to fix the objectives of present research.

However, from the review of past literatures following research gaps has been drawn:

A) Less investigation on effect of process parameters on submicron sized powder particles has been revealed
B) Less investigation has been carried out on issues associated with several aspects of laser sintering metal powder having less than 10µm particle size and it is still commercially not viable
C) To minimize porosity level use of less than 10µm particle size is still under research and development

The primary objective of this research is to explore and explain the selective laser sintering mechanism of submicron powder (less than 10µm particle size) by investigating the neck formation during joining of adjacent powder particles under the irradiation of laser energy and the resulting porosity formed between the particles. However, the investigation will be focused to explore the following:

(a) To study the mechanisms of neck formation and analyse influences of particle size on neck growth mechanism, using molecular level simulations
(b) To study the influences of particle size on porosity formation and to minimize porosity using molecular level simulations

(c) To investigate the neck formation during joining of adjacent powder particles under the irradiation of laser energy

(d) To investigate the resulting porosity formed between the adjacent powder particles under the irradiation of laser energy

(e) To investigate the effects of processing parameters on various mechanisms of laser sintering over range of powder size ranging from a nanometer to less than 10µm

CHAPTER – 2

MOLECULAR DYNAMICS SIMULATION OF SELECTIVE LASER SINTERING

One of the primary objectives of the present research is to explore the mechanism of selective laser sintering of submicron sized (less than 10μm particle size) metal powder by investigating neck formation during joining adjacent powder particles and porosity formation between particles, virtual experiments of laser sintering process are conducted using Molecular Dynamics simulations for copper-based nanoparticles.

Molecular level simulation describes the interactions among the atoms and molecules which is governed by macro and microscopic properties of the system. Various properties are being studied and computed using molecular simulation. However, all of the properties of a system may not be measured with the help of simulation study. Also measured quantity using simulation may not match with the data achieved from practical experiments. Practical experiments provide the averaged measured data of the properties over measurement time as well as number of particles. To measure these average data using computer simulation, the study should be focused on the kind of average to compute. Statistical mechanics helps to explain and measure the average quantity. During simulations, the derivations of basic expressions of statistical mechanics are done on the basis of some assumptions to simplify the computation. Molecular Dynamics simulation is popular among the molecular level simulation technique. Basic concepts of molecular dynamics, application in SLS are discussed in this chapter.

Virtual Experiments using Molecular Dynamics simulation has been carried out to investigate and validate neck growth mechanism in micro laser sintering. Large-scale Atomic/Molecular Massively Parallel Simulator (LAMMPS) [86] is used for conducting laser sintering virtual experiments using Molecular Dynamics simulations in the present research.

2.1 Molecular Dynamics Simulation and its approaches

Molecular Dynamics (MD) Simulation is popular computing method of the properties and equilibrium of many-body system. Molecular Dynamics is broadly accepted simulation tool in the area of research of thermodynamics. Simulation can be conducted in the range of length scale from Angstroms to Nanometer and time scale from femtosecond to picosecond. During practical experiments various measuring instruments are installed to maintain experimental environment and properties are measured after certain interval of time. After getting several data, the approximation is done to achieve more accurate quantity. Exactly similar approach is taken to carry out virtual experiments using Molecular Dynamics simulation. Firstly, the model is prepared which consists N number of atoms/molecules. Secondly, the prepared model is equilibrated by resolving Newton's equations of motion. The equations are solved until the change of properties tend to zero with respect to time. Finally, measurement of the quantity under observation is performed.

2.2 Fundamental Concepts of Molecular Dynamics

Newton's second law of motion is applied to movement each particle and equations of motion are resolved. Interactive forces act among each of the neighbouring atoms/molecules. Mathematical expression of these interactive is

$$F_{ij} = m_i a_i \qquad \dots (2.1)$$

where

F_{ij} resultant interactive force between atom *i* and *j*

m_i mass of atom *i*

$a_i = \frac{d^2 r_i}{dt^2}$ where, r_i is displacement of atom *i* at time *t*

These resultant interactive forces acting between atom *i* and *j* can be expressed as the gradient of interatomic/intermolecular potential energy of the neighbouring atoms/molecules. Suitable intermolecular/interatomic potential is needed to be chosen for Molecular Dynamics simulations. Primary coordinates and masses of atoms/molecules are defined according to lattice structure and type of material, respectively. A potential function is used to define the interatomic/intermolecular interaction $\phi(r_1, r_2, r_3, \dots\dots\dots, r_n)$, where $(r_1, r_2, r_3, \dots\dots\dots, r_n)$ are denoted as positional coordinates of atoms/molecules. To calculate the resultant interactive forces between each atom/molecule, the potential function is to be differentiated *w.r.t.* the distances of neighbouring atoms/molecules. Mathematical expression is shown below:

$$F_i = -\frac{\partial}{\partial r_i} \phi(r_1, r_2, r_3, \dots\dots\dots, r_n) \qquad \dots (2.2)$$

In Molecular Dynamics simulations various potential functions are used. Lennard-Jones (LJ) potential and embedded-atom method (EAM) potential are the most commonly used intermolecular/interatomic potential for metals. The fundamental concepts of EAM and LJ potential have been deliberated later. When selection of proper intermolecular/interatomic potential is done, a suitable algorithm is to be established for integrating the equations. Among different algorithms, Verlet algorithm is the most recommended algorithm. The theory of Verlet algorithm is discussed briefly later.

2.2.1 Interatomic/Intermolecular Potential

a) Lennard-Jones (LJ) Potential

LJ Potential is a mathematical model of approximation. Interaction of two neighbouring atoms/molecules is demonstrated by this potential. F_{ij} is resultant interacting force between atom i and j. F_{ij} can be replaced by LJ potential gradient. Mathematical expression is [87],

$$F_{ij} = -\frac{\partial \phi_{ij}}{\partial r_{ij}} \qquad \ldots (2.3)$$

Mathematically ϕ_{ij} (LJ potential) can be expressed as [88],

$$\phi_{ij} = 4\varepsilon\left[\left(\frac{\sigma}{r_{ij}}\right)^{12} - \left(\frac{\sigma}{r_{ij}}\right)^{6}\right] \qquad \ldots (2.4)$$

where

ϕ_{ij} Interatomic/intermolecular Lennard-Jones potential between the two atoms;

ε Lennard-Jones well depth parameter. It is the measure of attraction strength of two atoms/molecules. (shown in Fig. 2.1(a))

σ Interatomic/intermolecular separation at that distance interatomic/intermolecular potential turn out to be naught (shown in Fig. 2.1(a)). This is the equilibrium separation parameter (shown in Fig. 2.1(b)). It is equal to the half of the interatomic distance between nonbonding atoms.

r_{ij} separation distant of the atoms/molecules (centre distance of the atoms/molecules).

Minimum value of ϕ_{ij} at $r = R_{\min}$

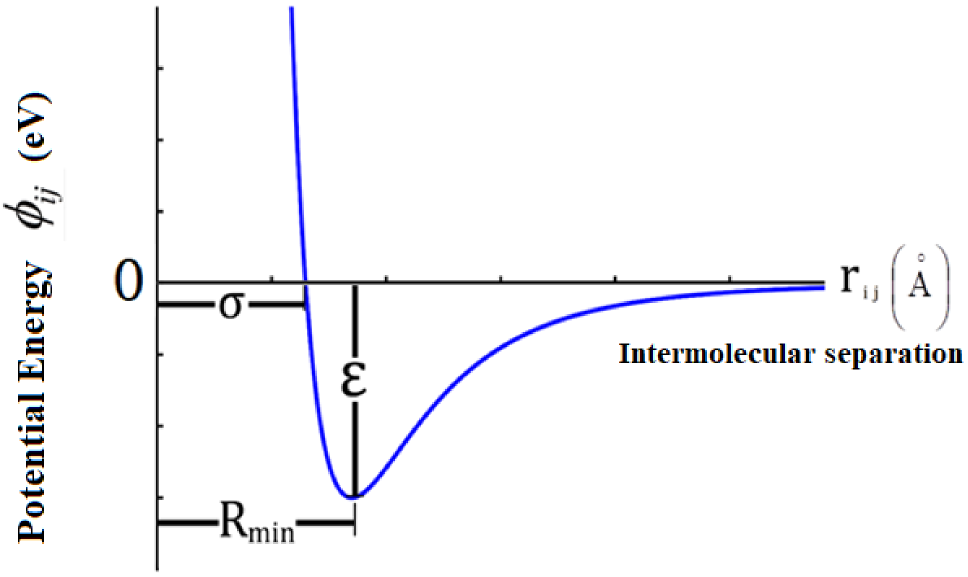

(a)

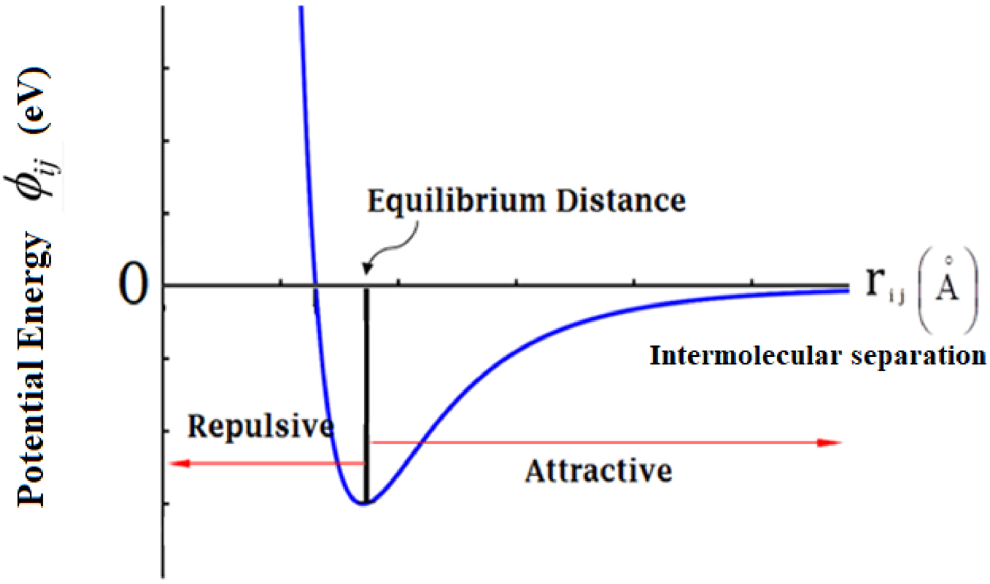

(b)

Fig. 2.1: LJ Potential energy vs. intermolecular separation curve

b) Embedded-Atom Method (EAM) Potential

The EAM Potential [27], [89] is another mathematical model of approximation of intermolecular potential energy among many atoms/molecules or bodies [90]. It is the summation of separation energies of many atoms/molecules and the near atoms/molecules [28], [29]. This is apposite for metallic materials. Mathematically this potential can be written as [90]

$$E_{tot} = \sum_{i=1}^{n} E_i \qquad \text{… (2.5)}$$

where E_{tot} is summation of separation energies of many atoms/molecules and the near atoms/molecules and E_i is energy of atom/molecule *i*.

The total energy of each molecule/atom is split into two terms. One term is intermolecular potential between atom/molecule *i* and *j*; another term is required energy to embed atom/molecule in the cloud of electron. Mathematically it is expressed as [89], [91]

$$\sum_{i=1}^{n} E_i = \frac{1}{2}\sum_{\substack{i,j \\ j\neq i}} \phi_{ij}\left(r_{ij}\right) + \sum_{i} U\left(\rho_i\right) \qquad \text{… (2.6)}$$

where

r_{ij}	separation of atoms/molecule *i* and *j*;
$\phi_{ij}\left(r_{ij}\right)$	interatomic/intermolecular potential between atoms/molecule *i* and *j*;
U	required energy to embed atom/molecule in the cloud of electron;
ρ_i	density of electron at location r_i because of adjacent atoms/molecules.

The Eq. (2.6) is valid within the cut-off distance of atom/molecule *i* from the neighbouring atoms/molecules. Interaction between atom/molecule can be possible within the Cut-off distance at which potential between neighbouring atoms/molecules is infinitesimally small.

c) Morse Potential

This is the mathematical model of interatomic potential to create bonds between pair of atoms/molecules. The interactive forces between the atoms/molecules will form a diatomic molecule when the atoms closer to each other. Mathematically this potential [92] can be written as [87], [93]

$$\phi(r_{ij}) = D_e\left(1 - e^{-\alpha\left(r_{ij} - r_e\right)}\right)^2 \qquad \text{... (2.7)}$$

where

r_{ij}	instantaneous interatomic/intermolecular distance;
r_e	equilibrium interatomic/intermolecular distance;
D_e	potential well depth (shown in Fig. 2.2);
α	constant determined from the physical properties of the material.

At the equilibrium interatomic/intermolecular distance, Morse potential energy function become lowest i.e. – D_e. When interatomic/intermolecular distance tends to infinite (Fig. 2.2), the potential tends to dissociation energy (D_e). Now, D_e is subtracted from ϕ_{ij} [87], [93]

$$\phi_{ij}^{*} = \phi_{ij} - D_e = D_e\left[e^{-2\alpha\left(r_{ij}-r_e\right)} - 2e^{-\alpha\left(r_{ij}-r_e\right)}\right] \qquad \text{... (2.8)}$$

where ϕ_{ij}^{*} is having a minimum value i.e. $\phi_{ij}^{*} = -D_e$ at $r_{ij} = r_e$ and $\phi_{ij}^{*} \rightarrow 0$ at $r_{ij} = \infty$

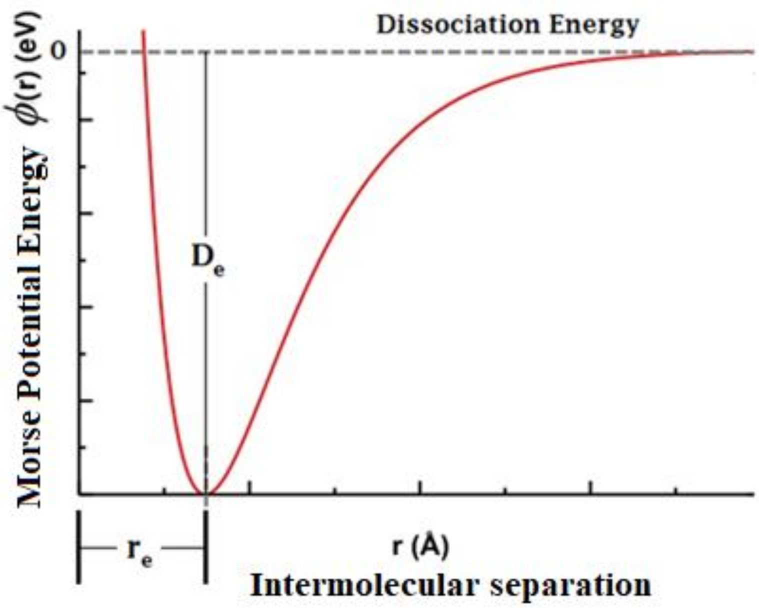

Fig. 2.2: Morse Potential energy vs. intermolecular separation curve

d) Born-Mayer Potential

This potential has been proposed by Born-Mayer. This potential function is intermolecular repulsion and it can be written as in the term of repulsion [87],

$$\phi(r) = A \cdot e^{-\left(\frac{r}{B}\right)} \qquad \text{... (2.9)}$$

where

$\phi(r)$	Born-Mayer Potential,
r	intermolecular/interatomic distance
A and B	empirically determined repulsive interaction components.

Potential well is not formed.

e) Tersoff Potential

Tersoff Potential [94] is the many-body interatomic potential energy. This energy function also has angular involvement. Mathematically this energy function can be expressed as [87]

$$E = \sum_i E_i = \frac{1}{2}\sum_i \sum_{i \neq j} \phi_{ij} \qquad \text{... (2.10)}$$

where

$$\phi_{ij} = f_C(r_{ij})\left[a_{ij}{}' f_R(r_{ij}) + b_{ij}{}' f_A(r_{ij})\right]$$

$$f_R(r) = A' \cdot e^{(-\lambda_1 r)}$$

$$f_A(r) = -B' \cdot e^{(-\lambda_2 r)}$$

$$f_C(r) = \begin{cases} 1, & r < R - D \\ \frac{1}{2} - \frac{1}{2}\sin\left(\frac{\pi}{2}(r - R)/D\right), & R - D < r < R + D \\ 0, & r > R + D \end{cases}$$

$$b_{ij}{}' = \left(1 + \beta^n \zeta_{ij}^n\right)^{-1/2n}$$

$$\zeta_{ij} = \sum_{k(\neq i,j)} f_C(r_{ij})\, g(\theta_{i,j,k}) . e^{\left[\lambda_3^3 (r_{ij} - r_{jk})^3\right]}$$

$$g(\theta) = 1 + \frac{c^2}{d^2} - \frac{c^2}{[d^2 + (h - \cos\theta)^2]}$$

$$a_{ij}{}' = \left(1 + \alpha^n \eta_{ij}^n\right)^{-1/2n}$$

$$\eta_{ij} = \sum_{k(\neq i,j)} f_c(r_{ij}) . e^{\left[\lambda_3^3 (r_{ij} - r_{jk})^3\right]}$$

where,

i, *j*, and *k*	label the atoms in the system;
r_{ij}	bond length of atoms *ij* bond;
$\theta_{i,j,k}$	bond angle between *ij* and *ik* bonds;
R and *D*	cut-off parameters;

A', B', $\lambda_1, \lambda_2, \lambda_3$, α, β, *n*, *c*, *d*, *h* are fitting parameters of the Tersoff potential.

2.2.2 Integration Algorithm

In Eq. (2.1), acceleration *a* can be expressed in differential form assuming constant acceleration as,

$$a = \frac{dv}{dt} \qquad \ldots (2.11)$$

Velocity *v* can be obtained by integrating Eq. (2.11)

$$v = at + v_0 \qquad \ldots (2.12)$$

Velocity $v = \frac{dr}{dt}$ and distance *r* can be derived after integrating Eq. (2.12),

$$r = vt + x_0 \qquad \ldots (2.13)$$

Combining Eqs. (2.12) and (2.13) the distance between atoms/molecules, can be found

$$r = \frac{1}{2}at^2 + v_0 t + r_0 \qquad \ldots (2.14)$$

where *r* is a function of initial distance, initial velocity, acceleration and time i.e. $r(r_0,v_0,a,t)$.

Taylor's series expansion can be applied to integrate Newton's equation of motion and to approximate the distance, velocity and acceleration, [91].

$$\left.\begin{aligned} r(t+\Delta t) &= r(t) + \dot{r}(t)\Delta t + \frac{1}{2}\ddot{r}(t)\Delta t^2 + \ldots \\ v(t+\Delta t) &= \dot{r}(t) + \ddot{r}(t)\Delta t + \frac{1}{2}\dddot{r}(t)\Delta t^2 + \ldots \\ a(t+\Delta t) &= \ddot{r}(t) + \dddot{r}(t)\Delta t + \frac{1}{2}\ddddot{r}(t)\Delta t^2 + \ldots \end{aligned}\right\rangle \qquad \ldots (2.15)$$

Where,

Δt	restricted or fixed timestep;
r, $\dot{r}$ and $\ddot{r}$	distance, velocity (*v*) and acceleration (*a*)
$\dddot{r}$ and $\ddddot{r}$	third- and fourth-order derivative of distance or position w.r.t. time.

Eq. (2.15) can be written as,

$$\left.\begin{aligned} r(t+\Delta t) &= r(t)+v(t)\Delta t+\frac{1}{2}a(t)\Delta t^2+\ldots \\ v(t+\Delta t) &= v(t)+a(t)\Delta t+\frac{1}{2}\dddot{r}(t)\Delta t^2+\ldots \\ a(t+\Delta t) &= a(t)+\dddot{r}(t)\Delta t+\frac{1}{2}\ddddot{r}(t)\Delta t^2+\ldots \end{aligned}\right\rangle \qquad \ldots (2.16)$$

a) Basic Verlet Algorithm

The most suitable algorithm of integration and approximation is Verlet Algorithm [95]. This algorithm is simply based on the distances from initial coordinates of the molecule or atom, i.e. next or previous positions of the atom/molecules can be found by using this algorithm. The next position at next timestep, can be obtained by using [91]:

$$r(t+\Delta t)=r(t)+v(t)\Delta t+\frac{1}{2}a(t)\Delta t^2+\ldots \qquad \ldots (2.17)$$

Similarly, to find the previous step following equation can be used,

$$r(t-\Delta t)=r(t)-v(t)\Delta t+\frac{1}{2}a(t)\Delta t^2+\ldots \qquad \ldots (2.18)$$

Summing the Eqs. (2.17) and (2.18), we get [91],

$$r(t+\Delta t)\approx 2r(t)-r(t-\Delta t)+a(t)\Delta t^2 \qquad \ldots (2.19)$$

During estimation of atom's new location, a little error remains due to approximation. Acceleration can be expressed (from Newton's eq. of motion) as

$$\ddot{r}(t)=a=\frac{F(t)}{m}$$

where $F(t)$ → force and m → atom's mass.

Eq. (2.19) is redrafted as [91],

$$r(t+\Delta t)\approx 2r(t)-r(t-\Delta t)+\frac{F(t)}{m}\Delta t^2 \qquad \ldots (2.20)$$

In basic Verlet algorithm, velocity is not used to find the new position of the atom.

There are some similar algorithms of Verlet algorithm. They are Verlet Leapfrog algorithm and velocity Verlet algorithm.

b) Verlet Leapfrog Algorithm

To find the new location, the velocities of atoms are used in this algorithm. Velocities are being computed by averaging half-integer timesteps. The velocities at half-integer timesteps can be expressed by the following equations [91]

$$v\left(t-\frac{\Delta t}{2}\right)=\frac{r(t)-r(t-\Delta t)}{\Delta t} \qquad \dots (2.21)$$

and

$$v\left(t+\frac{\Delta t}{2}\right)=\frac{r(t+\Delta t)-r(t)}{\Delta t} \qquad \dots (2.22)$$

The equation of new location can be obtained from eq. (2.22), [91]

$$r(t+\Delta t)=r(t)+v\left(t+\frac{\Delta t}{2}\right)\Delta t \qquad \dots (2.23)$$

The equation of the updated velocity is derived from Verlet algorithm, [91]

$$v\left(t+\frac{\Delta t}{2}\right)=v\left(t-\frac{\Delta t}{2}\right)+\frac{F(t)}{m}\Delta t \qquad \dots (2.24)$$

This algorithm helps to calculate the new coordinate and velocity of atoms. Coordinate and velocity jump over one another.

c) Velocity Verlet Algorithm

Position, velocity and acceleration at the time *t* (variable) are being calculated using Velocity Verlet algorithm. Velocity is incorporated during solving Basic Verlet algorithm. Precision is not compromised during computation. Mathematically it is expressed as [91]

$$r(t+\Delta t)=r(t)+v(t)\Delta t+\frac{1}{2}a(t)\Delta t^2 \qquad \dots (2.25)$$

$$v(t+\Delta t)=v(t)+\frac{1}{2}\left[a(t)+a(t+\Delta t)\right]\Delta t \qquad \dots (2.26)$$

Velocity Verlet algorithm does not monitor the velocity continuously at each timestep. Due to this reason, for computation using this algorithm, very low memory is needed. Following steps are followed by this algorithm [91]:

Step-1 → Velocity is to be computed at half of the timestep,

$$v\left(t+\frac{1}{2}\Delta t\right)=v(t)+\frac{1}{2}a(t)\Delta t$$

Step-2 → Position is to be computed at same timestep, $r(t+\Delta t)=r(t)+v\left(t+\frac{1}{2}\Delta t\right)\Delta t$

Step-3 → Acceleration of next timestep $a(t+\Delta t)$ is to be derived from interactive energy potential by means of $r(t+\Delta t)$

After elimination of the half-integer time step velocity, the steps of computations can be done by following the steps below [91]:

Step-1 → Position is to be computed, $r(t+\Delta t)=r(t)+v(t)\Delta t+\frac{1}{2}a(t)\Delta t^2$

Step-2 → Acceleration of next timestep $a(t+\Delta t)$ is to be derived from interactive energy potential by means of $r(t+\Delta t)$

Step-3 → Velocity at same timestep is to be computed,

$$v(t+\Delta t)=v(t)+\frac{1}{2}[a(t)+a(t+\Delta t)]\Delta t$$

Assumption for this algorithm: Acceleration $a(t+\Delta t)$ is independent of velocity $v(t+\Delta t)$ and only dependent of position $r(t+\Delta t)$.

2.3 Thermodynamic Ensembles

The MD simulation is conducted in atomistic approach. Due to this reason, difficulty arises during study of each and every atom and their properties at the microscopic level at different states. To determine atomic positions and movements, statistical mechanics is needed in the microscopic level. In the macroscopic level, they tend to show same thermodynamic states that can be defined by thermodynamic properties at different states. Macro level thermodynamic properties of a system are volume, pressure, temperature, entropy etc. Some of the group of some thermodynamic properties form the thermodynamic ensembles. In these group of ensembles some properties remain constant and others are variables or not considered during observation. Table 2.1 is showing the ensembles [87].

Table 2.1 Basic thermodynamic ensembles

Ensembles	**Abbreviation**	**Constant properties**	**Variable properties**
Canonical	NVT	No of atoms, N, Volume, V and Temperature, T	Pressure, P
Micro Canonical	NVE	No of atoms, N, Volume, V and Overall Energy, E	Pressure, P Temperature, T
Isobaric Isothermal	NPT	No of atoms, N, Pressure, P and Temperature, T	Properties under observation
Grand Canonical	µVT	Volume, V, Temperature, T and Chemical Potential, µ	Properties under observation

2.4 Molecular Dynamics (MD) Simulation for SLS of Nanoparticles

Molecular Dynamics simulation study to explore mechanism of neck formation during selective laser sintering of nanoparticles, follow the following sequence of process:

Step 1: Selection or preparation of atomistic Model.
Step 2: Selection of suitable an intermolecular potential.
Step 3: Appropriate algorithm selection to integrate the equations of motion.
Step 4: Initialisation of Model.
Step 5: The model is relaxed from initial state to its dynamically equilibrium condition.
Step 6: Simulation the model is run to analyse the required results.

Fig. 2.3 is showing the flowchart of simulation study

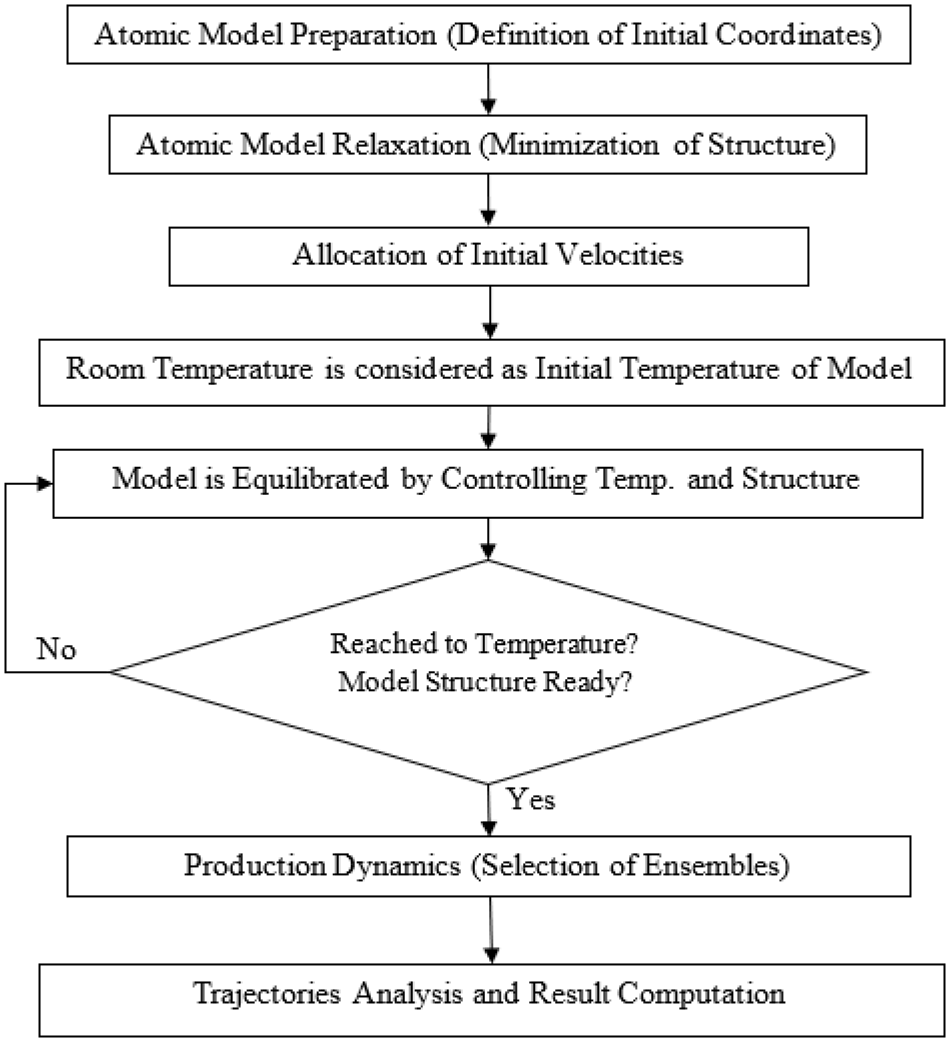
Atomic Model Preparation (Definition of Initial Coordinates)
Atomic Model Relaxation (Minimization of Structure)
Allocation of Initial Velocities
Room Temperature is considered as Initial Temperature of Model
Model is Equilibrated by Controlling Temp. and Structure
Reached to Temperature?
Model Structure Ready?
No
Yes
Production Dynamics (Selection of Ensembles)
Trajectories Analysis and Result Computation

Fig. 2.3 Flowchart of MD simulation study

2.5 Investigation of Neck Growth Mechanism and Porosity Formation During SLS Using MD Simulation-Based Virtual Experiments

Virtual Experiment is the experiment conducted virtually over computer-based environment. During all practical experiments, various instruments are installed or attached to measure various properties to maintain experimental environment and properties are measured after certain interval of time. Exactly same conditions are followed during the virtual experiments to maintain the proper environment of the experiments. The experimental environment is created numerically as well as preserving some important and considered properties of the many-body systems.

All the virtual experiments are carried out in a 3D space using “large-scale atomic/molecular massively parallel simulator” (LAMMPS). Firstly, a cuboid shaped simulation box is created and periodic boundary conditions is applied on all the faces. The atomistic model is prepared inside the simulation box. During preparation of atomistic model of the nanoparticles, the dimension, fcc crystal structure and initial position of the particles are provided. The simulation is started with the equilibration of the simulation box at room temperature. Temperature of the system is maintained by adjusting velocities and positions of atoms using Nosé-Hoover thermostat. The virtual experiments of SLS of nanoparticles are carried out using NVT ensemble.

2.5.1 Molecular Dynamics Simulation-based Virtual experiments to explore mechanism of neck-growth in process of Laser Sintering of pair of Nanoparticles

Computer program has been developed for Molecular Dynamics simulation to study laser sintering of pair of copper nano-particles. Periodical boundary conditions have been considered during preparation of atomistic model.

Firstly, a 3D simulation box has been created of size 4.26×2.34×2.34 nm^3. Two identical nano-particles have been created of diameter 1.82 nm. Verlet algorithm has been used to assign the velocities to the atoms to attain control over temperature. List of atom neighbour has been updated at time step of 1.00 femtosecond (fs) or 0.001 picosecond (ps). Centre distance between two nanoparticles are maintained (D1+0.02)nm, where D1=1.82nm, the diameter of each copper nano-particle at room temperature i.e. 300K. Initial atomistic model has been shown in Fig. 2.4. In this figure outer most surface distance D2 = (2×D1+0.02)nm.

a) Atomistic Model

Inside the simulation box, two alike copper nano-particles are formed. Diameter of each nano-particles is 1.82nm with a centre distance of 1.84nm. Therefore, 0.02nm gap is kept between two nano-particles. Fig. 2.4 shows the initially created atomic model of copper nanoparticle pair. The atom count in these two nanoparticles are 12,646 and 12,630, respectively. Maxwell–Boltzmann distribution is taken to maintain velocities of atom randomization in the nanoparticles and initial configuration of the particles at the room temperature are given.

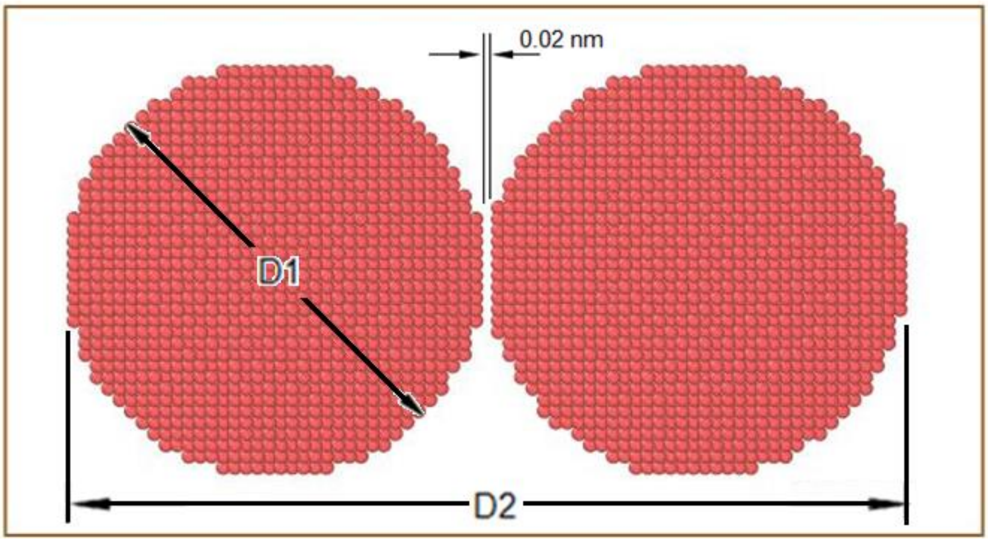

Fig. 2.4 Atomistic model of copper particles of diameter (D1)=1.82nm with 0.02 nm gap between two particles; D2=(2×D1+0.02)nm

b) Simulation Model for Sintering

During simulation of laser sintering model, continuous heating of copper nano-particles using laser irradiation is considered. Also, no loss of heat is considered during the simulation study [29]. In all directions, periodic boundary conditions are considered when atomistic model of copper nano-particle is created.

During laser sintering neck is initialized after very short duration of heating and neck has been fully grown after a long duration. The neck has been grown by following to Frenkel's theory of sintering (Fig. 1.4).

I. Isothermal Sintering: Simulation of the atomistic model is conducted isothermally with NVT considerations. The set of temperature considered is (300, 600, 900, 1200 and 1500 K). Temperature is maintained by using Nose-Hoover thermostat. The initial temperature of the atomistic model is maintained at the above set of temperatures and then to randomize the atoms are given velocity using Maxwell-Boltzmann distribution. Equilibration of the system is done with Embedded Atom Method potential gradients (EAM) [27], [89] at the above set of temperatures and isothermally sintering is continued for 30ps time. Initially neck formation is started during process of equilibration. The datasheet of Timestep vs Temperature is shown in Table 2.2. Diameter of neck is measured at every time step (Table 2.2). Temp. vs. time graph has been shown in Fig. 2.5.

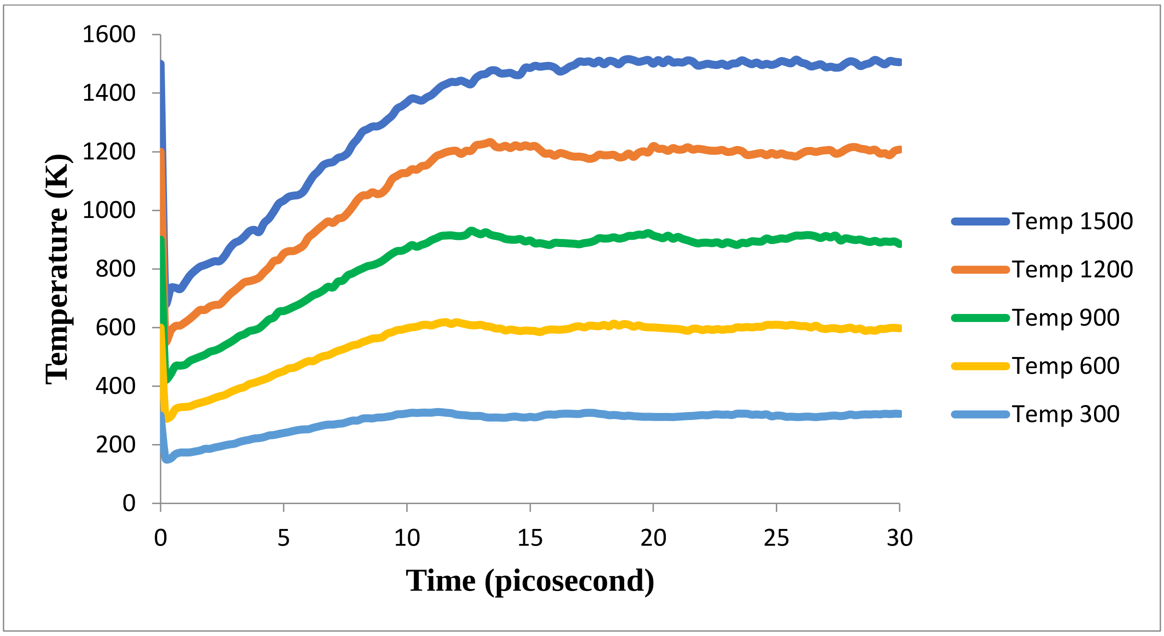

Fig. 2.5: Temperature vs Time graph for Isothermal sintering at different temperatures (300K, 600K, 900K, 1200K and 1500K) (following Table 2.2)

Table 2.2 Change in temperature and neck diameter w.r.t. time during isothermal sintering simulation

	Isothermal Temp 300K		Isothermal Temp 600K		Isothermal Temp 900K		Isothermal Temp 1200K		Isothermal Temp 1500K	
Time (ps)	Sintering Temp (K)	Neck Dia(nm)	Sintering Temp (K)	Neck Dia(nm)	Sintering Temp (K)	Neck Dia(nm)	Sintering Temp (K)	Neck Dia(nm)	Sintering Temp (K)	Neck Dia(nm)
0	300	0	600	0	900	0	1200	0	1500	0
0.5	160.4161	0.2355	308.391265	0.3254	454.324505	0.36	596.41963	0.5054	734.990835	0.3254
1	173.68213	0.5262	329.23885	0.5123	473.4007	0.5123	618.20438	0.5054	754.56714	0.4777
1.5	178.808465	0.5192	340.54851	0.4915	497.126415	0.5608	652.682745	0.5123	800.9393	0.5192
2	186.34728	0.54	353.15962	0.5469	517.34027	0.5815	671.73738	0.5469	820.20954	0.5331
2.5	195.984805	0.5469	367.60667	0.5469	533.912915	0.6023	686.78494	0.5331	835.505935	0.5469
3	203.58569	0.5538	385.94337	0.547	558.94434	0.6023	725.99028	0.4985	888.42927	0.5054
3.5	215.55506	0.5677	402.11549	0.5538	582.504995	0.5885	756.29343	0.4985	919.369455	0.5193
4	222.80633	0.54	417.36491	0.54	597.68921	0.5954	770.80038	0.547	926.09479	0.5677
4.5	232.52114	0.5538	434.1303	0.5469	631.037575	0.63	815.83425	0.6438	984.49688	0.5954
5	240.18478	0.6646	451.5055	0.6438	656.43053	0.6369	852.6263	0.5954	1033.2555	0.63
5.5	248.933875	0.6646	466.15991	0.6508	674.56976	0.6508	865.143875	0.6785	1051.44775	0.6577
6	253.03374	0.6785	485.40073	0.6577	699.0572	0.6993	907.22684	0.6923	1091.7172	0.6715
6.5	264.1082	0.6992	498.60598	0.6923	722.023835	0.72	943.07142	0.6992	1143.9186	0.7062
7	268.86237	0.7615	513.14015	0.7338	737.05033	0.7615	957.43282	0.7131	1165.1465	0.7062
7.5	275.59636	0.7823	529.08436	0.7685	769.339215	0.7754	983.71223	0.7615	1190.1105	0.7477
8	282.73813	0.81	542.51737	0.7823	794.35994	0.7962	1036.4574	0.7892	1244.4279	0.7892
8.5	290.258835	0.8169	559.126315	0.7962	811.251485	0.7962	1056.72885	0.81	1281.496	0.8031
9	293.4466	0.8377	567.18464	0.8238	827.72406	0.8446	1060.589	0.8308	1294.5662	0.8377
9.5	301.06027	0.8516	587.648755	0.8446	856.4622	0.8377	1112.3106	0.8169	1335.3086	0.817
10	306.80879	0.8377	597.62156	0.8446	870.44293	0.8446	1127.7297	0.8654	1368.9129	0.8308
10.5	309.06368	0.8862	605.596255	0.8723	879.067265	0.8931	1144.79055	0.8862	1376.6246	0.8446

	Isothermal Temp 300K		Isothermal Temp 600K		Isothermal Temp 900K		Isothermal Temp 1200K		Isothermal Temp 1500K	
Time Step (ps)	**Sintering Temp (K)**	**Neck Dia(nm)**	**Sintering Temp (K)**	**Neck Dia(nm)**	**Sintering Temp (K)**	**Neck Dia(nm)**	**Sintering Temp (K)**	**Neck Dia(nm)**	**Sintering Temp (K)**	**Neck Dia(nm)**
11	309.5331	0.9	607.06454	0.8862	898.18912	0.9	1169.251	0.9485	1393.6382	0.9277
11.5	310.184075	0.9	617.569155	0.8862	913.352905	0.9208	1195.38955	0.9485	1427.36575	0.9485
12	303.34271	0.8792	618.22438	0.8862	912.36215	0.9208	1203.0068	0.9623	1437.6965	0.9485
12.5	299.52611	0.9	609.647685	0.8931	923.55578	0.9277	1203.15185	0.9831	1432.936	0.9692
13	298.15244	0.8931	609.32915	0.8792	918.31041	0.9069	1224.6721	1.0177	1462.6887	0.99
13.5	293.0036	0.8723	599.66168	0.8792	914.68115	0.9069	1225.11695	1.0592	1477.0827	1.0385
14	292.22687	0.8723	590.18973	0.8654	902.40142	0.8931	1220.2469	1.08	1467.4127	1.0662
14.5	295.145745	0.8585	589.5425	0.8586	900.82365	0.8931	1218.9677	1.0385	1462.84715	1.0454
15	295.27942	0.8792	589.07919	0.8863	897.11108	0.9138	1217.0935	1.08	1485.9048	1.0662
15.5	299.463605	0.8792	587.358	0.8451	886.435705	0.9415	1200.22765	1.0869	1491.0974	1.0869
16	302.74743	0.852	593.12126	0.8658	889.26363	0.8931	1186.31	1.0454	1486.7898	1.0246
16.5	306.085315	0.852	595.370015	0.8587	887.5645	0.8723	1189.4502	1.0731	1484.3371	1.0593
17	305.15467	0.8379	604.38086	0.8449	884.32101	0.8931	1183.3076	1.0662	1507.8363	1.0731
17.5	308.77931	0.8656	606.09323	0.8589	893.10403	0.8792	1177.439	1.0869	1504.8232	1.0731
18	304.33905	0.8449	609.0609	0.8526	903.57653	0.8792	1187.8078	1.08	1498.7222	1.0869
18.5	300.90838	0.8723	609.91486	0.8598	905.80612	0.8654	1185.10845	1.1146	1502.75285	1.1077
19	299.423	0.9069	609.59156	0.8387	912.65343	0.8792	1193.7382	1.1077	1516.0559	1.1008
19.5	296.027145	0.9208	605.009825	0.8741	916.877575	0.8585	1198.89555	1.1631	1508.3502	1.1215
20	295.176	0.9277	600.57376	0.8802	913.93556	0.8792	1219.2921	1.1285	1500.5901	1.1146
20.5	295.07188	0.9069	597.619055	0.8595	909.248475	0.8792	1206.4455	1.0869	1508.39195	1.1008
21	295.8516	0.8931	595.27529	0.8802	909.3304	0.8654	1207.153	1.1146	1505.715	1.1215
21.5	298.269675	0.9	592.399705	0.873	894.655895	0.8654	1211.3035	1.1354	1509.7636	1.1077
22	301.38477	0.9138	591.52619	0.8799	889.40398	0.8723	1208.2032	1.1077	1496.3102	1.1215

	Isothermal Temp 300K		**Isothermal Temp 600K**		**Isothermal Temp 900K**		**Isothermal Temp 1200K**		**Isothermal Temp 1500K**	
Time Step (ps)	**Sintering Temp (K)**	**Neck Dia(nm)**	**Sintering Temp (K)**	**Neck Dia(nm)**	**Sintering Temp (K)**	**Neck Dia(nm)**	**Sintering Temp (K)**	**Neck Dia(nm)**	**Sintering Temp (K)**	**Neck Dia(nm)**
22.5	303.499315	0.9208	593.37144	0.8868	889.525805	0.8931	1203.52765	1.1216	1496.8404	1.1008
23	303.18982	0.9415	594.55769	0.9007	890.9535	0.8792	1199.3093	1.0869	1493.2457	1.0869
23.5	306.149775	0.9415	600.52052	0.8799	885.693035	0.8792	1203.91625	1.0869	1507.29975	1.0662
24	302.50299	0.9346	600.40638	0.8871	894.44563	0.8654	1190.0717	1.0869	1498.8475	1.1008
24.5	302.914245	0.9346	605.85015	0.8799	898.88856	0.8446	1191.6645	1.1008	1497.9601	1.1008
25	299.60755	0.9208	609.65104	0.873	900.86397	0.8585	1189.3804	1.0938	1501.0407	1.0662
25.5	295.66761	0.9069	607.979675	0.873	905.8159	0.8793	1187.46175	1.0938	1503.7159	1.1008
26	294.88953	0.9138	604.80031	0.873	913.50211	0.8862	1193.3383	1.1008	1504.5412	1.1008
26.5	295.033155	0.9069	603.22626	0.8526	912.877945	0.8862	1200.99735	1.1008	1492.7581	1.1008
27	296.94367	0.9	595.1502	0.8667	912.36331	0.8862	1204.8215	1.0869	1488.1244	1.08
27.5	298.72041	0.9069	595.984315	0.8595	905.37062	0.9139	1195.22345	1.0869	1487.89275	1.08
28	303.31991	0.9138	599.75249	0.8664	901.73067	0.8723	1214.6637	1.0869	1508.7421	1.1216
28.5	303.100785	0.9069	592.729015	0.8664	897.82064	0.9	1209.62525	1.0731	1495.2154	1.1008
29	304.5117	0.8931	589.2601	0.8598	895.66253	0.9	1206.9909	1.0731	1513.3719	1.1008
29.5	305.252245	0.8931	596.820915	0.8592	893.041835	0.8862	1191.52495	1.0938	1503.97405	1.08
30	305.42152	0.9	597.4891	0.8661	884.97224	0.8723	1207.5868	1.08	1505.4456	1.0869

II. Nonisothermal Sintering: Heat is given to the nanoparticles externally. The temperature of nanoparticle pair is increased from 300K to 1500K during heating for 30ps of time [27]. Therefore, the rate of heating is maintained at 4.0×10^{13}K/s. Table 2.3 shows the change in Temperature and Neck diameter w.r.t. time. This has been observed in the Temp. vs. Time graph (Fig. 2.6) that temperature of the model increases linearly with time sintering. Diameter of neck has been measured in each time step (Table 2.3).

Table 2.3: Change in temperature and neck diameter w.r.t. time during non-isothermal sintering simulation

Time Step (ps)	Temperature (K)	Neck Dia (nm)
0	300	0
0.5	160.491795	0.2631
1	174.04439	0.3738
1.5	179.72938	0.5469
2	188.15251	0.5469
2.5	199.098505	0.5538
3	208.43238	0.5608
3.5	222.83764	0.5608
4	232.94885	0.54
4.5	246.451035	0.5608
5	258.70272	0.6508
5.5	272.50579	0.6715
6	282.09319	0.6715
6.5	300.959245	0.6992
7	313.08727	0.81
7.5	328.58598	0.8238
8	346.74825	0.8238
8.5	367.61537	0.8308
9	384.70339	0.8515
9.5	404.335025	0.8446
10	433.91344	0.8723
10.5	453.723625	0.8931
11	477.67482	0.8792
11.5	503.545195	0.8238
12	528.23007	0.8308
12.5	555.561275	0.817
13	584.05184	0.8238
13.5	607.570055	0.8169
14	633.49229	0.8308

Time Step (ps)	Temperature (K)	Neck Dia (nm)
14.5	663.83903	0.8169
15	688.75793	0.8169
15.5	718.82017	0.8169
16	757.41547	0.8031
16.5	786.98	0.8169
17	809.34255	0.8031
17.5	848.305935	0.7962
18	885.48608	0.8238
18.5	916.12666	0.8308
19	942.50446	0.8515
19.5	978.6449	0.8377
20	1000.4366	0.8654
20.5	1029.452	0.8585
21	1065.1001	0.8931
21.5	1083.7145	0.9277
22	1116.551	0.9277
22.5	1141.06545	0.9762
23	1162.9049	0.9831
23.5	1181.58715	1.0177
24	1215.99	1.0315
24.5	1237.8765	1.0523
25	1248.3121	1.0523
25.5	1275.29245	1.08
26	1290.913	1.0731
26.5	1326.42095	1.1008
27	1334.0039	1.1146
27.5	1356.8519	1.1354
28	1383.9152	1.1008
28.5	1388.9004	1.1008
29	1402.3109	1.1354
29.5	1422.2597	1.1492
30	1444.2245	1.1423

c) Result and Discussion

○ Growth of Neck between two Copper nano-particles during isothermal sintering

From the output results of Molecular Dynamics simulation study of isothermal sintering of pair of copper nano-particles, it has been observed that initially temperature of pair of particles decrease up to 0.20ps and after that temperature increases linearly w.r.t. time. The temperature vs. time curves are shown in Fig. 2.5. The initial temperature of the atomistic model is maintained at the above set of temperatures and then to randomize the atoms are given velocity using Maxwell-Boltzmann distribution. The overall heating time is 30ps with a time step of 1.0fs.

Change in neck diameter during isothermal sintering is shown in Fig. 2.7. Initially, fast neck growth has been observed during isothermal sintering at the considered temperature. Afterwards, during sintering in isothermal consideration at 300K, 600K and 900K temperature, neck diameter gets stabled after 10ps and during sintering at 1200 and 1500 K neck gets stabled after 15ps.

- **Growth of Neck between two Copper nano-particles during nonisothermal sintering**

During nonisothermal sintering of copper nanoparticle pair, temperature increases, in 30ps of time, from 300K to 1444K. Fig. 2.8 shows the gradual neck growth during nonisothermal sintering. At the initial stage, pair of nano-particle is kept at 300K. Slight oscillation in temperature is observed up to 400fs time. After that, temperature increases gradually up to 1444K following linear path in the Temp. vs. Time graph (Fig. 2.6). Particles are heated continuously for 30ps time.

Table 2.4 and Fig. 2.9 shows the change in particle diameter (D1) and change in distance D2 (in Fig. 2.4). Initially, distance of the centres of nano-particles is kept (D1+0.02)nm as shown in Fig. 2.4. Just after starting of heating, the nanoparticle pair come in contact with one another. Later, with increment in temperature, the grain boundary and surface atoms of each nanoparticles started travelling together for minimizing the surface tension. Surface atoms and grain boundary atoms travel towards the point of contact of two particles which leads to form neck between the nanoparticles. Due to the displacement of nearby atoms of contact point, neck growth initiates. As crystalline structure of surface atoms is lost and fusion of outer surface of the nanoparticles is initialized.

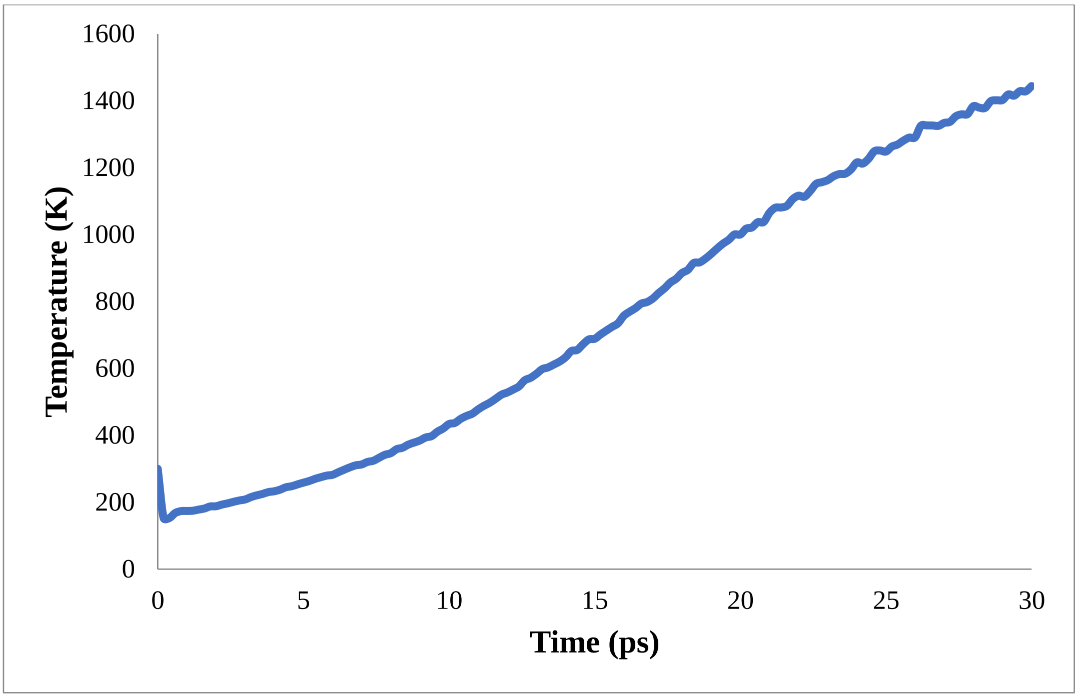

Fig. 2.6: Temperature vs Time graph for non-isothermal sintering from temperatures 300K- 1500K (following Table 2.3)

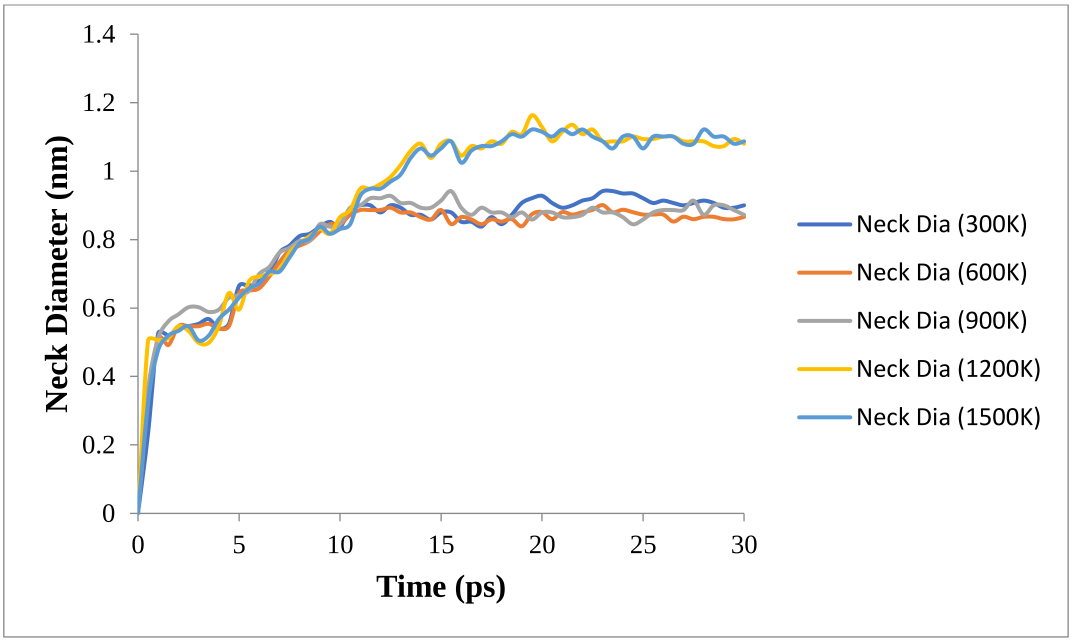

Fig. 2.7 Neck diameter vs time graph during isothermal sintering at set of temperatures (following Table 2.2)

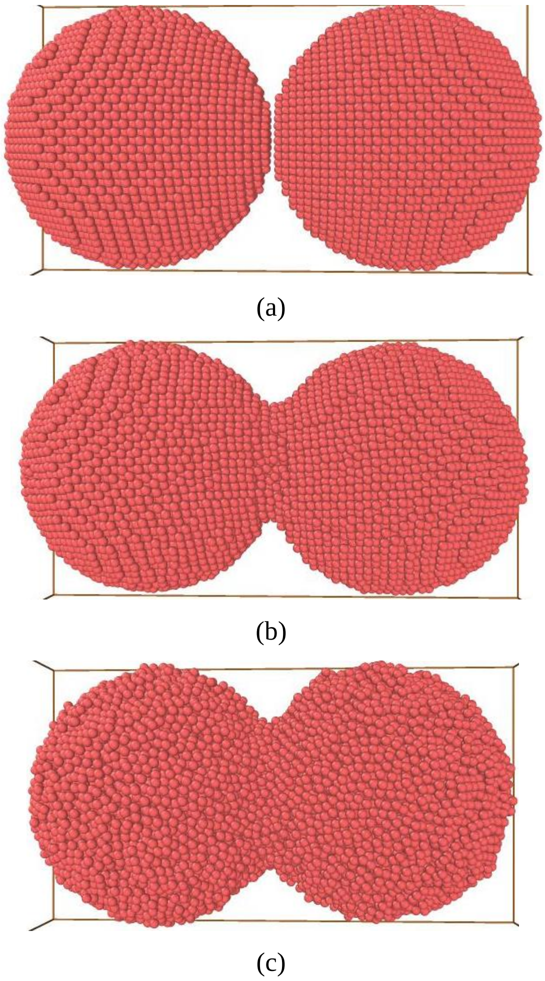

(a) Initial configuration, (b) at 15 ps, (c) at 30 ps

Fig. 2.8: Configuration changes of Cu-Cu pair during sintering

Table 2.4 Change in D1 (diameter of particle) and D2 (Fig. 2.4)

Time Step (ps)	D1 (nm)	D2 (nm)
0	1.8192	3.6662
0.5	1.8123	3.6662
1	1.8123	3.6662
1.5	1.8053	3.6662
2	1.7915	3.6662
2.5	1.7915	3.6662
3	1.8123	3.6593
3.5	1.8123	3.6385
4	1.8262	3.6107
4.5	1.8262	3.6037
5	1.8123	3.5899
5.5	1.8123	3.5829
6	1.8192	3.5968

Time Step (ps)	D1 (nm)	D2 (nm)
6.5	1.8192	3.569
7	1.8192	3.5551
7.5	1.8192	3.5412
8	1.8192	3.5204
8.5	1.8262	3.5065
9	1.8262	3.5065
9.5	1.8262	3.4996
10	1.8262	3.4996
10.5	1.8401	3.5204
11	1.8331	3.5343
11.5	1.8331	3.5343
12	1.8331	3.5551
12.5	1.8331	3.5551
13	1.8123	3.576
13.5	1.8123	3.576
14	1.8123	3.6315
14.5	1.8262	3.6315
15	1.8262	3.6523
15.5	1.8123	3.6523
16	1.8123	3.6454
16.5	1.8331	3.6315
17	1.8192	3.6246
17.5	1.8192	3.6454
18	1.8192	3.6385
18.5	1.8401	3.6176
19	1.8262	3.6037
19.5	1.8262	3.576
20	1.847	3.576
20.5	1.8539	3.5482
21	1.8539	3.5482
21.5	1.8539	3.5274
22	1.8748	3.5204
22.5	1.8748	3.4996
23	1.8678	3.4996
23.5	1.8678	3.5204
24	1.8678	3.4857
24.5	1.8678	3.4996
25	1.8678	3.5204
25.5	1.8678	3.5135
26	1.8609	3.4996

Time Step (ps)	D1 (nm)	D2 (nm)
26.5	1.8609	3.5204
27	1.8609	3.5204
27.5	1.8609	3.5204
28	1.8609	3.5204
28.5	1.8609	3.5204
29	1.8887	3.5204
29.5	1.8956	3.5204
30	1.8956	3.5204

The dimensional change of the nanoparticles is measured and changes in configuration during sintering are investigated. Measured dimensions of D1 and D2 (Fig. 2.4) and neck diameters are mentioned in Table 2.4 and Table 2.3 respectively. Figs. 2.9 and Fig. 2.10 are showing the change in D1, D2 and neck diameter w.r.t. time.

From the Fig. 2.9 it is observed that total length (D2) has been decreased with increment in sintering time due to movement of atoms towards the neck plane formed at the point of contact of two particles. Also, this has been observed that the diameter of particles (D1) has no such significant change in dimension with sintering time. Fig. 2.10 shows significant change in neck diameter, all through sintering time of 30ps.

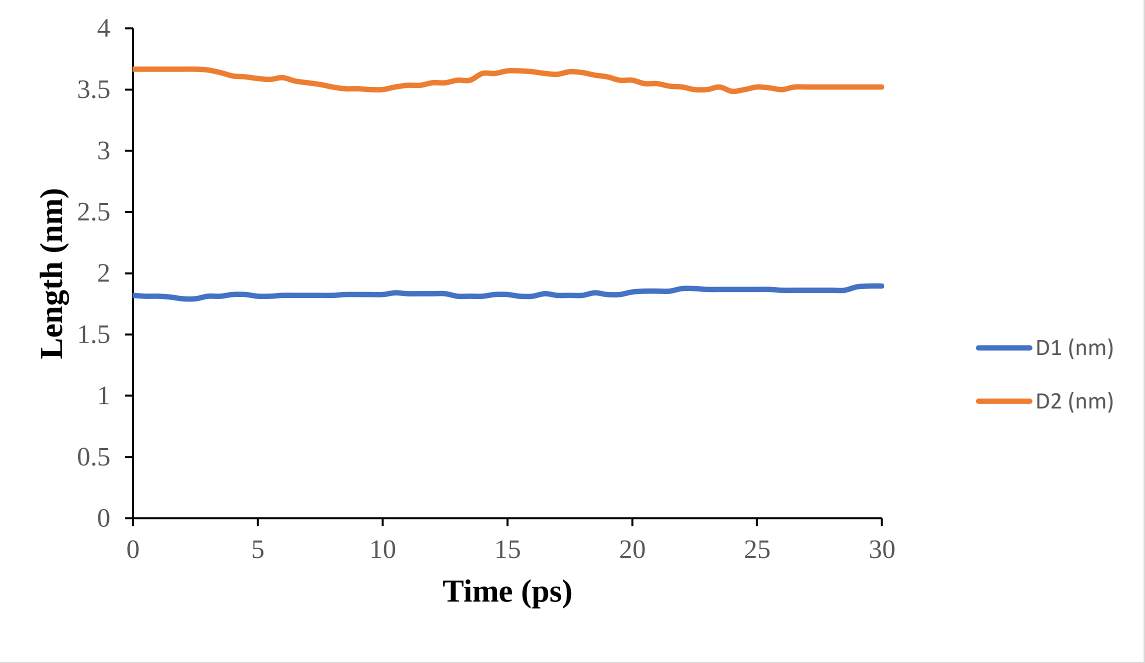

Fig. 2.9 Change in dimension of D1 and D2 in non-isothermal sintering process

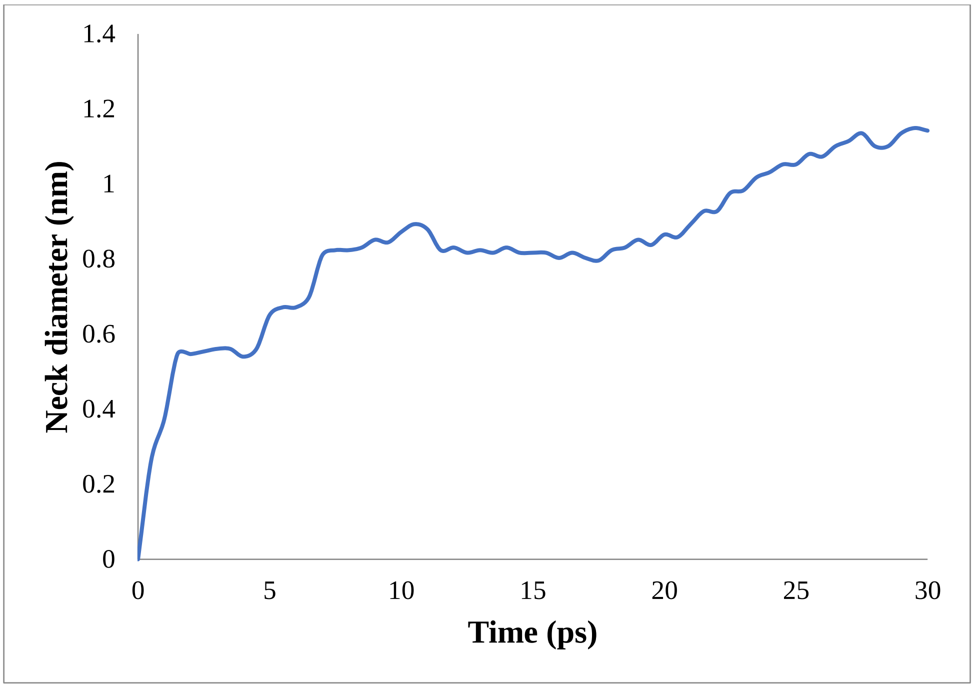

Fig. 2.10 Neck diameter vs. Time graph during non-isothermal sintering (following Table 2.3)

2.5.2 Molecular Dynamics Simulation-Based Virtual Experiments to explore atomic displacement during growth of neck in laser sintering of nano-particles using same heating rate

In order to study and establish relation between the neck growth in sintering of different sized nanoparticle pairs undergoing similar heating rates, MD simulation-based virtual experiments were conducted. In this case, sintering of spherical identical copper nanoparticles, three separate models are created. In this MD simulation of sintering, periodical boundary conditions are used.

At first, a cuboid-shaped three-dimensional simulation box is created. Inside the simulation box pair of spherical identical nanoparticles has been created. The centres of gravity of both the particles are present horizontally at equal y-coordinate and z-coordinate. The centres of gravity are at a distance of the particle diameter, i.e. there is no gap between two particles. Initially, the particles are kept at room temperature, i.e. 300K. The atoms are randomized to achieve temperature control using Verlet algorithm. Due timesteps have been used as 1.0fs. The neck growth in each case has been observed during sintering. The steps of neck growth according to Frenkel’s theory [13] of sintering are shown in Fig. 1.4.

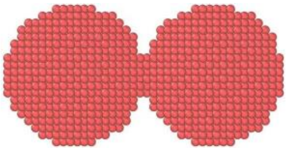

(a) Pair of copper nanoparticles of size 1nm

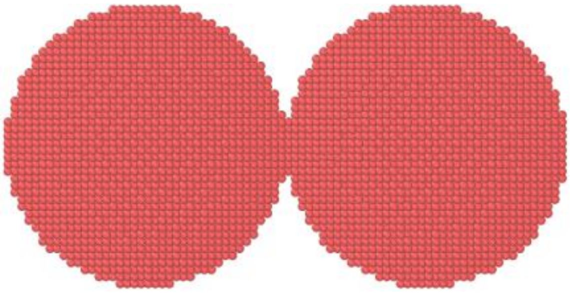

(b) Pair of copper nanoparticles of size 2nm

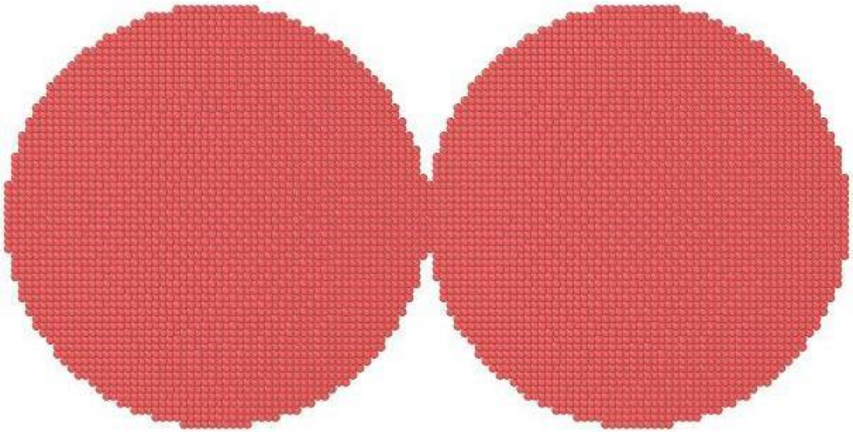

(c) Pair of copper nanoparticles of size 3nm

Fig. 2.11: Initial Copper nano-particles pair models of size 1nm, 2nm and 3nm particle size (figures are not in scale)

a) Atomistic Model Development

For virtual experiments of laser sintering using molecular dynamics simulation, three different atomistic models of copper nanoparticles pairs have been developed to explore sintering mechanisms. In each of the three models both the particles are. The first atomistic model contains, pair of 1nm diameter copper particles in 3D cuboidal shaped simulation box. Similarly, the second and third models contain pair of spherical and identical copper particles of diameters 2nm and 3nm respectively in 3D cuboidal shaped simulation box. During creation of atomistic models, periodic boundary conditions are considered in all direction. Each particle of the first model contain 2103 number of atoms i.e. 4206 atoms for two particles. Similarly, number of atoms of each particle in second model is 16779 i.e. in two particles 33558 atoms. In the third model, each particle contains 56606 atoms and total 113212 atoms in two particles. Fig. 2.11 is showing three of the initially developed models. Along with sintering mechanisms, growth in neck area has also been studied due to dislocation of atoms in various sintering mechanisms. The atoms are randomised using Maxwell–Boltzmann distribution and initially particles are kept in room temperature.

b) Simulation for Laser Sintering

Continuous heating using laser beam irradiation is considered during sintering of pair of copper nano-particles in each of the three models. Particles heater thoroughly for the time period of 30ps with time step of 0.001ps and list of neighbouring atoms are updated. For all the three models, same rate of heating, 4.0×10^{13}K/s is maintained. No heat loss is considered throughout the process of sintering simulations [29] for each model.

c) Results and Discussion

i) Snap shots and Vectorplots of copper nano-particle pair during sintering

During laser sintering each of the model of pair of Cu nano-particles are heated continuously, at the rate of 4×10^{13} K/s and temperature is increased following a linear equation from 300K to 1500K. Heating is done for 30ps with time step of 0.001ps. Figs. 2.12, 2.13 and 2.14 are showing the snapshots of pairs of 1nm, 2nm and 3nm copper nanoparticles, respectively, at time steps 5.6ps, 12ps, 18.4ps, 24.8ps and 30ps. After completion of sintering at 30ps time, three models are compared and are found that they have reached at three different temperatures 1426.3587K (1nm pair), 1437.0025K (2nm pair) and 1391.1457K (3nm pair) after 30ps heating.

The snapshots of three models after 30ps time are compared and it is observed that growth of neck is more through and better in smaller size nanoparticle pair than larger size pair of nanoparticles. The snapshots of 1nm pair of copper particles exhibit better shape and stronger bonding between particles than other two pairs after formation of fully developed neck after 30ps heating the nanoparticles. Also, the change in diameter of neck size with time of sintering is more significant more in the pair of 1nm particles. Substantial change in neck diameter with heating time has also been observed during heating pair 2nm particles at the same rate, and growth of neck is also smooth and consistent. But very less change neck diameter has been observed in pair of 3nm particles. The size of neck is almost same throughout the process of sintering.

Spherical like shape has been achieved after completion of heating for 30ps of time, in the case of sintering of 1nm pair of copper particles. This phenomenon indicates strong bonding of adjacent particles. This happens due to atom diffusion from the outer surface and finally melting occurs. Neck formation is started just 2.4ps of time after heating started. Melting phenomenon is not the expected phenomenon of sintering process.

The visions during sintering of pairs of nanoparticles of different size 1nm, 2nm and 3nm are shown in Fig. 2.12, Fig. 2.13 and Fig. 2.14, respectively, at five different time-steps of 5.6ps, 12ps, 18.4ps, 24.8ps and 30ps. Vector plots illustrate directions of the atom movements. Fig. 2.15, Fig. 2.16 and Fig. 2.17 are showing the vectors of movement of atoms throughout the process of sintering of copper nanoparticle pairs of size 1nm, 2nm and 3nm respectively, at time steps 5.6ps, 12ps, 18.4ps, 24.8ps and 30ps. Directions and magnitudes of atom displacement vectors are represented by the arrowheads in Fig. 2.15, Fig. 2.16 and Fig. 2.17. with reference to the primary location of that similar atom.

The results of three cases sintering of copper nanoparticle pair are compared. Observations reveals that after 5.6ps time, the atom movement directions on the surface of 1nm nanoparticle pair are significantly more than in 2nm and 3 nm nanoparticle pairs. The atom movement could be hardly distinguished after 5.6ps in the cases of 2nm and 3nm particle pairs. Growth of neck is also affected by the atom movement phenomenon. The history of growth of neck is shown in Fig. 2.19 and Fig. 2.20 and in Table 2.5. During sintering 2nm nanoparticle pair, the atom movement is become noteworthy after 18.4ps whereas after 24.8ps atom notable movement is observed in the pair of 3nm particle. In all the cases, atom followed a whirling path during dislocation. The atoms move towards neck through the whirling path. The whirling path direction in the adjacent particles are in opposite with respect to one another.

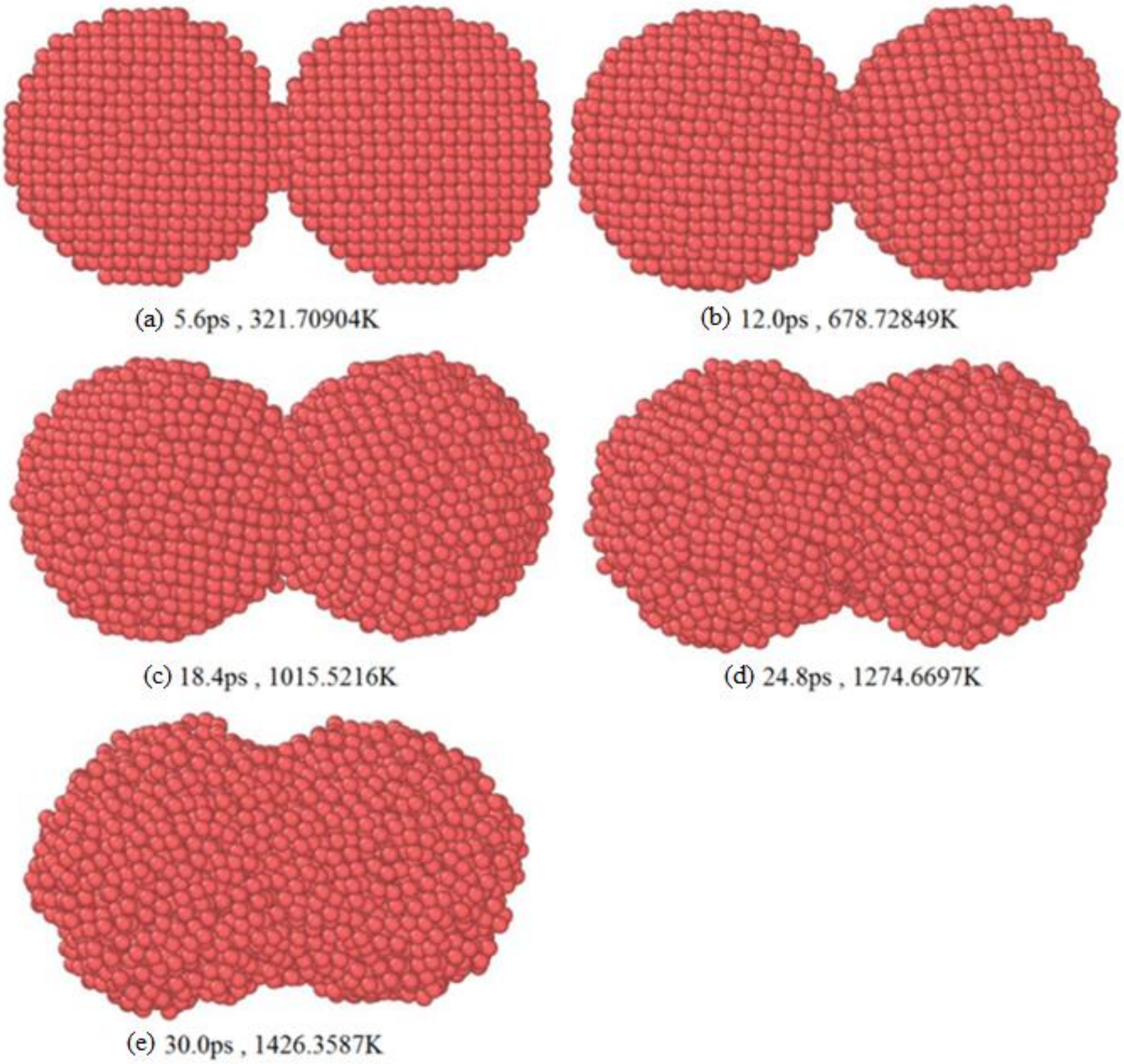
(a) 5.6ps , 321.70904K

(b) 12.0ps , 678.72849K

(c) 18.4ps , 1015.5216K

(d) 24.8ps , 1274.6697K

(e) 30.0ps , 1426.3587K

Fig. 2.12: Snap shots of sintering the 1nm nanoparticle pair at time steps 5.6ps, 12ps, 18.4ps, 24.8ps and 30ps

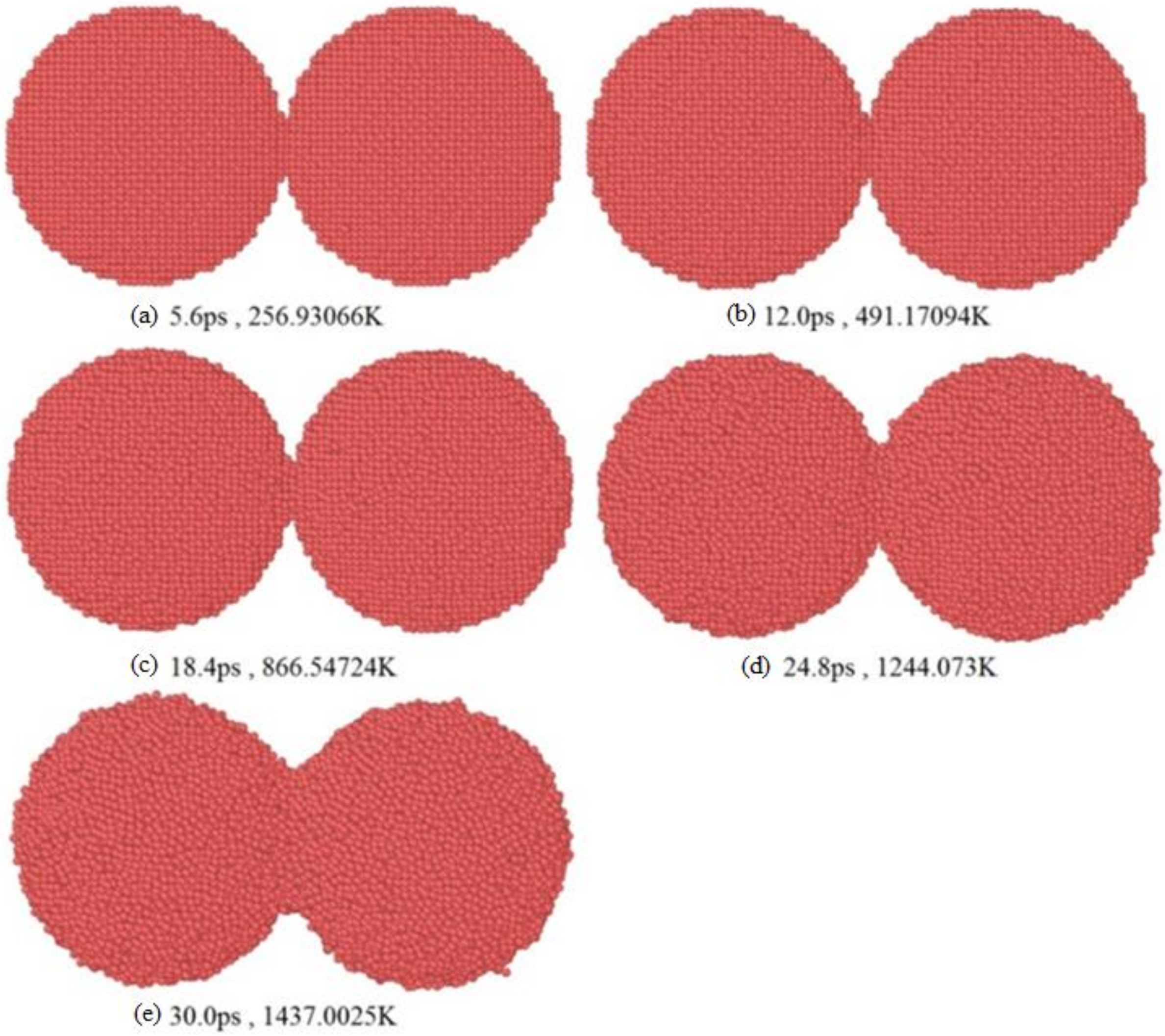
(a) 5.6ps , 256.93066K
(b) 12.0ps , 491.17094K
(c) 18.4ps , 866.54724K
(d) 24.8ps , 1244.073K
(e) 30.0ps , 1437.0025K

Fig. 2.13: Snap shots of sintering the 2nm nanoparticle pair at time steps 5.6ps, 12ps, 18.4ps, 24.8ps and 30ps

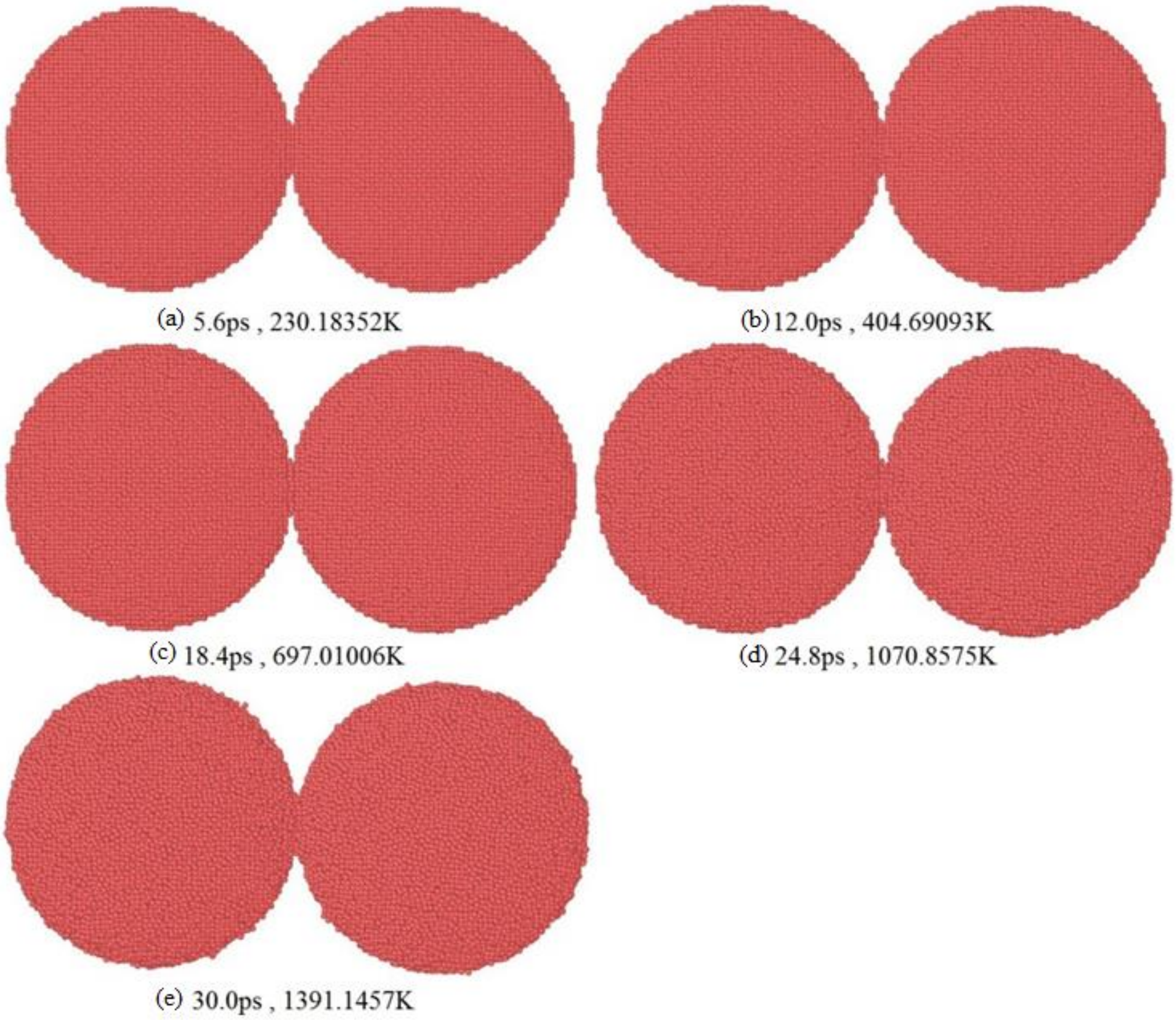

(a) 5.6ps , 230.18352K

(b) 12.0ps , 404.69093K

(c) 18.4ps , 697.01006K

(d) 24.8ps , 1070.8575K

(e) 30.0ps , 1391.1457K

Fig. 2.14: Snap shots of sintering the 3nm nanoparticle pair at time steps 5.6ps, 12ps, 18.4ps, 24.8ps and 30ps

Fig. 2.15, Fig. 2.16 and Fig. 2.17 shows the vector plots of atom displacement. Vector plots reveal that in the left particle the whirling direction of atoms is anticlockwise whereas clockwise rotation is seen in the right particle. Due to dislocation of atoms the fusion in nanoparticles occurs. Surface stresses of the molten metal tend to propel the atoms to merge and create one single sphere-shaped particle. From the displacement vectors it is observed that movement of surface atoms are more significant than atoms of other atoms of the particles. Random atom movement is observed at higher temperature. Using same rate of heating, the neck formation is more thorough in smaller size nanoparticle pair. But melting phenomenon increases with decrement in particle size which is not desired during process of sintering.

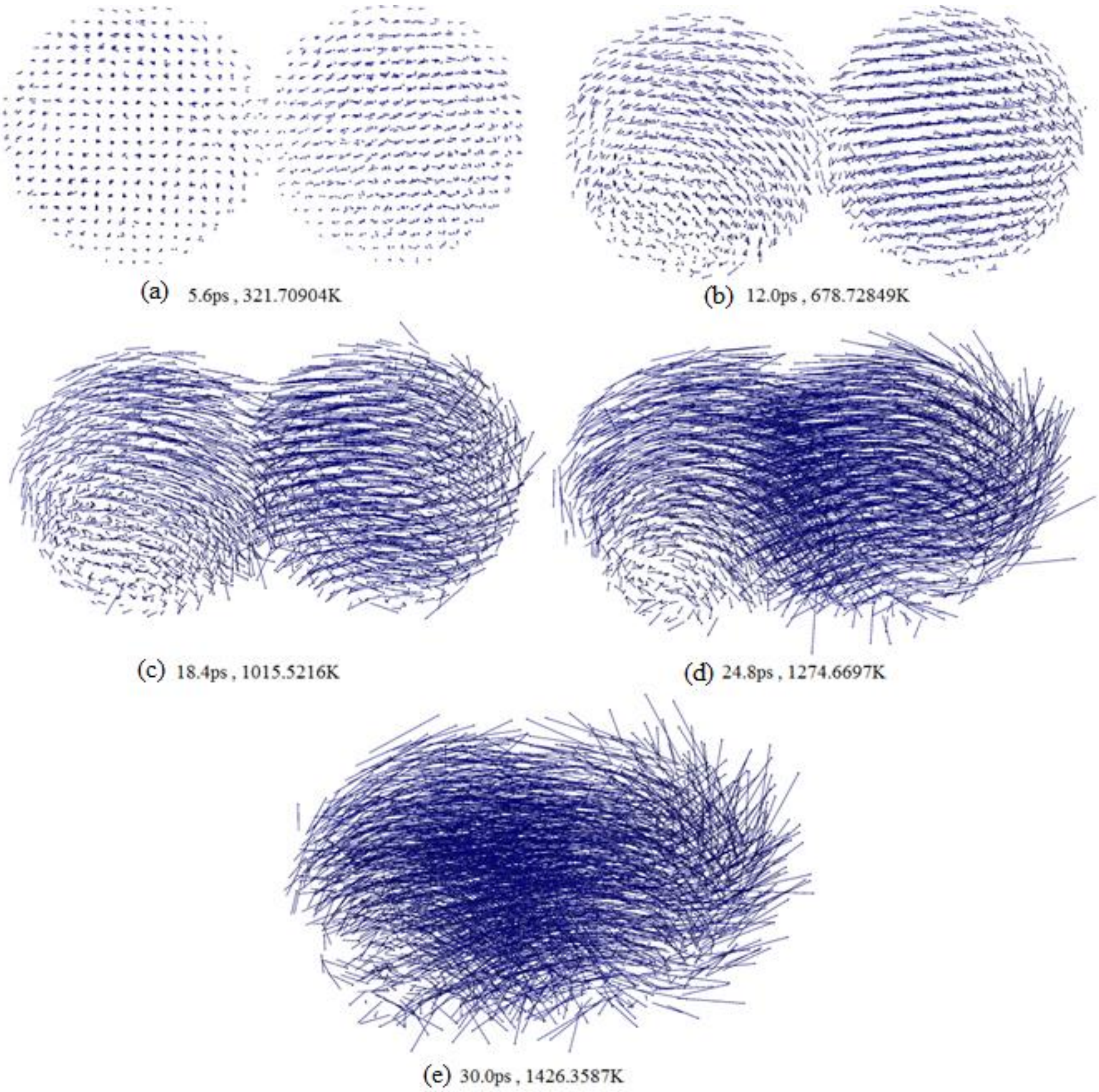

Fig. 2.15: Vector plots of atom displacements during sintering of 1nm pair of nanoparticles at 5.6ps, 12ps, 18.4ps, 24.8ps and 30ps time

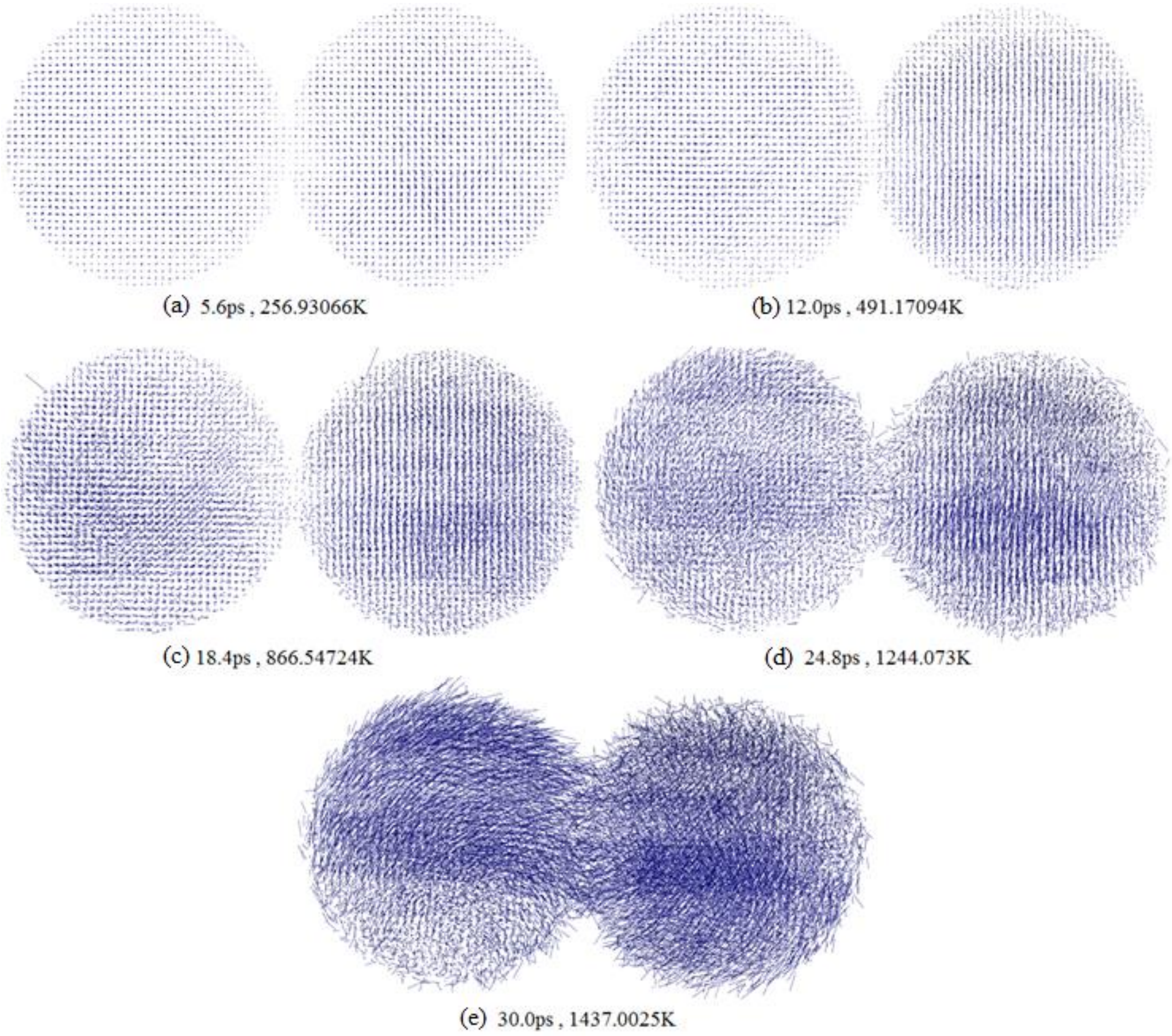

(a) 5.6ps , 256.93066K

(b) 12.0ps , 491.17094K

(c) 18.4ps , 866.54724K

(d) 24.8ps , 1244.073K

(e) 30.0ps , 1437.0025K

Fig. 2.16: Vector plots of atom displacements during sintering of 2nm pair of nanoparticles at 5.6ps, 12ps, 18.4ps, 24.8ps and 30ps time

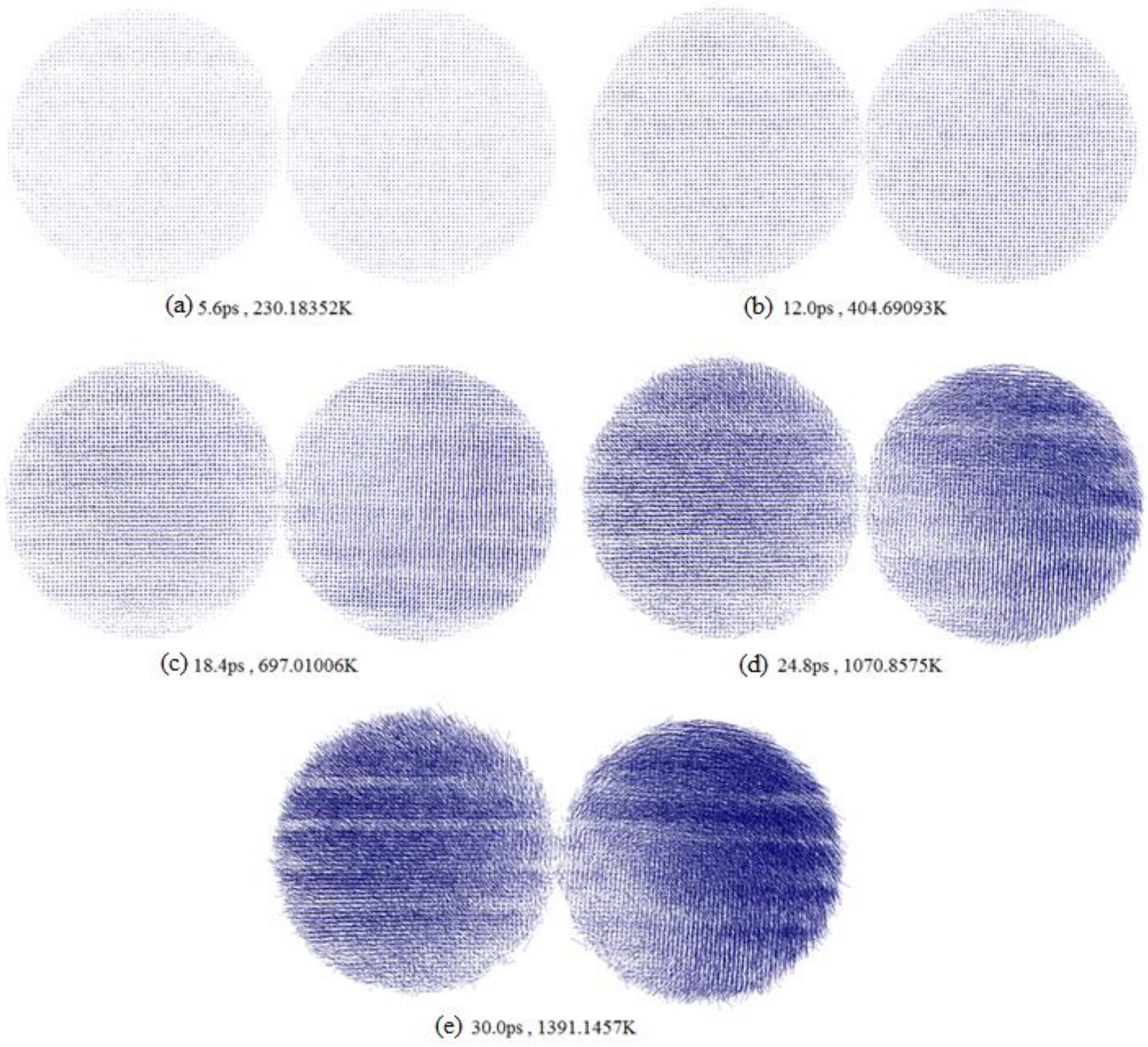

(a) 5.6ps , 230.18352K

(b) 12.0ps , 404.69093K

(c) 18.4ps , 697.01006K

(d) 24.8ps , 1070.8575K

(e) 30.0ps , 1391.1457K

Fig. 2.17: Vector plots of atom displacements during sintering of 3nm pair of nanoparticles at 5.6ps, 12ps, 18.4ps, 24.8ps and 30ps time

ii) Growth of Neck throughout the process of Laser sintering of pairs of copper nanoparticle

During sintering change of temperature with respect to time is shown in Fig. 2.18. The initial temperature of the pairs of nanoparticles is set at room temperature i.e. 300K. It is observed that temperature drops at the initial stage of simulation and later, linearly increment in temperature is noted up to 30ps time.

Table 2.5 Change of Temperature, Neck diameter, Neck growth (%) and MSD w.r.t. Time

Timestep (ps)	Temperature (K)			Neck diameter (nm)			Neck growth (%)			Mean square displacement ($Å^2$)		
	1nm	2nm	3nm	1nm	2nm	3nm	1nm	2nm	3nm	1nm	2nm	3nm
0	300	300	300	0.00	0.00	0.00	0.00	0.00	0.00	1.16×10^{-23}	2.22×10^{-23}	1.02×10^{-21}
0.8	180.7908	171.0183	165.1926	0.21	0.31	0.15	21.00	15.50	5.00	0.0267603	0.0205451	0.0153513
1.6	198.6147	176.4134	170.4202	0.31	0.41	0.15	31.00	20.50	5.00	0.0510288	0.0239746	0.0162587
2.4	214.3622	189.3499	178.6482	0.32	0.43	0.27	32.00	21.50	9.11	0.116478	0.036707	0.0185895
3.2	239.439	203.1574	189.4481	0.33	0.43	0.27	33.00	21.50	9.11	0.199965	0.0502361	0.0225461
4	266.2378	219.4462	201.9867	0.33	0.42	0.40	33.00	21.00	13.44	0.253413	0.0731412	0.0280057
4.8	296.5938	234.4928	214.979	0.34	0.43	0.40	34.00	21.50	13.44	0.285753	0.0975698	0.0349444
5.6	321.709	256.9307	230.1835	0.33	0.44	0.37	33.00	22.00	12.33	0.312384	0.127477	0.0428464
6.4	359.2549	276.9553	245.7128	0.31	0.45	0.44	31.00	22.50	14.56	0.367335	0.153909	0.0533404
7.2	404.4353	300.7012	263.5118	0.31	0.45	0.44	31.00	22.50	14.56	0.471521	0.175338	0.0682416
8	439.7414	326.3766	281.9086	0.32	0.45	0.47	32.00	22.50	15.56	0.6546	0.188398	0.0838563
8.8	485.1308	354.0505	303.6004	0.32	0.45	0.47	32.00	22.50	15.56	0.914731	0.189843	0.100562
9.6	526.2677	386.4892	325.0112	0.32	0.44	0.47	32.00	22.00	15.56	1.25864	0.187482	0.121302
10.4	583.6942	418.8552	350.4539	0.33	0.45	0.48	33.00	22.50	16.11	1.7152	0.184851	0.14305
11.2	618.2348	458.8383	376.9094	0.34	0.45	0.51	34.00	22.50	17.00	2.32893	0.187385	0.162693
12	678.7285	491.1709	404.6909	0.41	0.45	0.47	41.00	22.50	15.56	3.14979	0.216597	0.189945
12.8	723.5269	536.0515	433.0569	0.43	0.45	0.47	43.00	22.50	15.56	4.23667	0.251598	0.217059
13.6	776.0726	573.3612	465.3983	0.45	0.45	0.48	45.00	22.50	16.11	5.603	0.341524	0.234724
14.4	823.6552	621.6449	498.9964	0.48	0.47	0.46	48.00	23.50	15.22	7.20286	0.419383	0.270265
15.2	873.5786	661.087	531.7095	0.54	0.47	0.47	54.00	23.50	15.56	9.18051	0.559144	0.31491
16	924.1169	719.4238	572.6176	0.57	0.45	0.50	57.00	22.50	16.67	11.4265	0.666093	0.336608
16.8	947.1217	756.2601	611.6388	0.59	0.46	0.48	59.00	23.00	15.89	13.9623	0.835342	0.383338
17.6	987.9876	813.0195	649.613	0.6	0.45	0.55	60.00	22.50	18.44	16.8456	0.943085	0.469389
18.4	1015.522	866.5472	697.0101	0.64	0.45	0.55	64.00	22.50	18.44	20.1134	1.10619	0.537059

Timestep (ps)	Temperature (K)			Neck diameter (nm)			Neck growth (%)			Mean square displacement (Å^2)		
	1nm	2nm	3nm	1nm	2nm	3nm	1nm	2nm	3nm	1nm	2nm	3nm
19.2	1040.193	912.9134	743.683	0.61	0.46	0.55	61.00	23.00	18.44	23.6482	1.23537	0.629521
20	1069.581	967.5443	785.1169	0.62	0.46	0.55	62.00	23.00	18.44	27.3512	1.36383	0.78574
20.8	1105.953	1010.654	832.5464	0.66	0.47	0.54	66.00	23.50	18.11	31.6102	1.54228	0.955035
21.6	1133.216	1070.332	886.8577	0.66	0.49	0.54	66.00	24.50	18.11	36.4302	1.65231	1.13138
22.4	1165.989	1100.309	935.0486	0.74	0.56	0.53	74.00	28.00	17.56	41.4484	1.90135	1.39755
23.2	1198.675	1155.775	979.9693	0.72	0.58	0.51	72.00	29.00	17.00	46.6483	2.06946	1.71367
24	1232.603	1191.624	1035.705	0.78	0.7	0.54	78.00	35.00	17.89	52.4304	2.41286	2.01924
24.8	1274.67	1244.073	1080.858	0.77	0.74	0.52	77.00	37.00	17.33	58.8977	2.76263	2.42566
25.6	1285.32	1278.249	1140.218	0.79	0.78	0.52	79.00	39.00	17.33	65.6035	3.27886	2.92547
26.4	1295.297	1311.681	1185.323	0.84	0.84	0.54	84.00	42.00	17.89	72.2947	3.93379	3.41691
27.2	1338.133	1340.788	1234.916	0.82	0.86	0.54	82.00	43.00	17.89	79.4001	4.70062	3.95436
28	1369.412	1374.143	1284.785	0.81	0.88	0.52	81.00	44.00	17.33	87.2264	5.74586	4.63313
28.8	1395.793	1402.031	1327.352	0.83	0.93	0.58	83.00	46.50	19.33	96.2466	6.98816	5.39352
29.6	1425.236	1420.439	1367.002	0.89	1.01	0.60	89.00	50.50	20.11	106.477	8.58799	6.12576
30	1426.359	1437.003	1391.146	0.89	1.07	0.60	89.00	53.50	20.11	113.89229	9.470066	6.761794

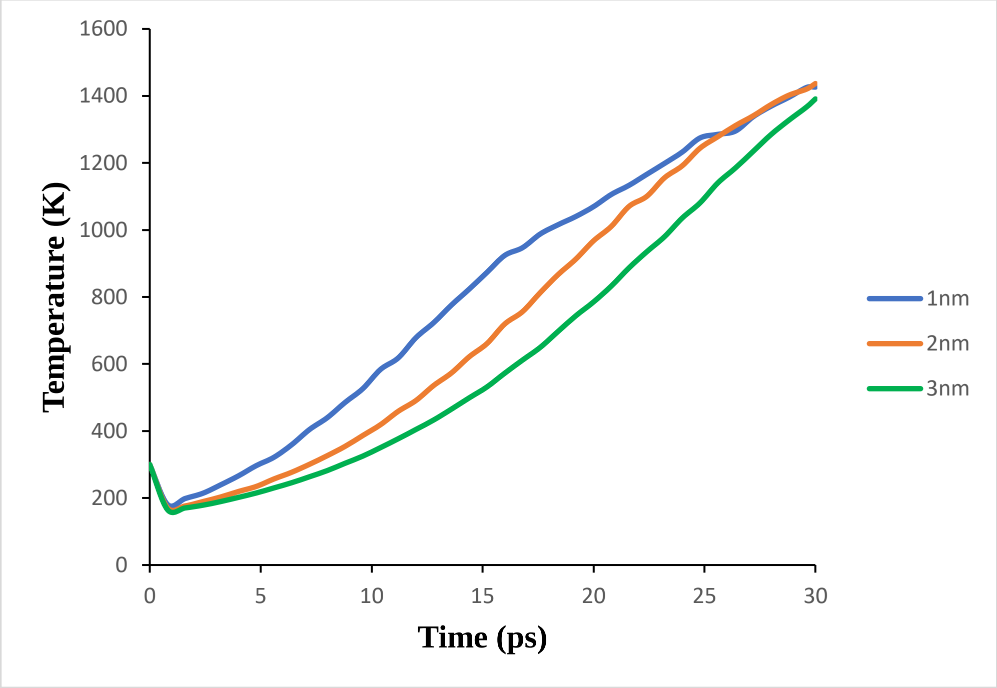

Fig. 2.18: Change in Temperature w.r.t. Time during sintering of pairs of copper nanoparticles (following Table 2.5)

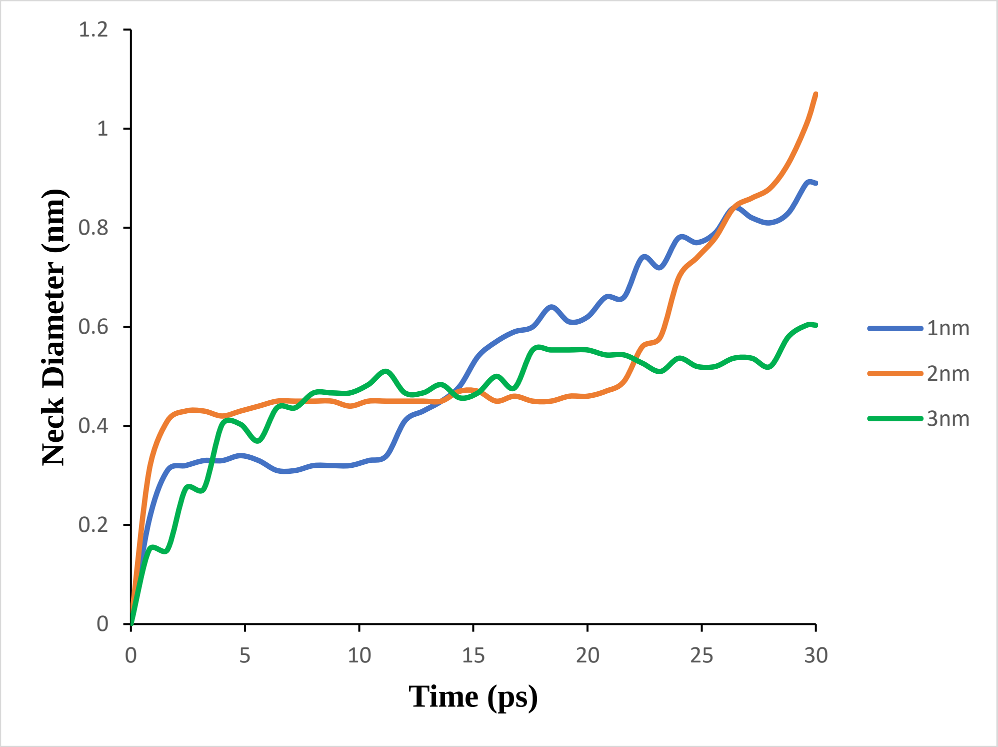

Fig. 2.19: Neck size Variation with Time throughout the process of laser sintering of copper nanoparticle pairs (following Table 2.5)

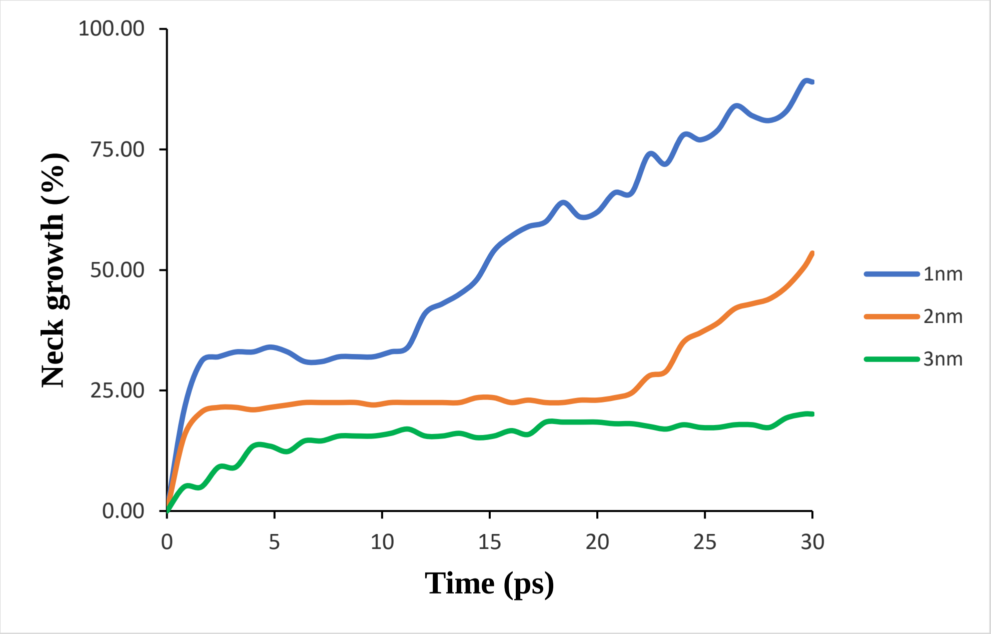

Fig. 2.20: Percentage of neck growth with reference to particle size and variation of neck growth percentage with time of heating during laser sintering of nanoparticle pairs (following Table 2.5)

Table 2.5 shows the change in change of Temperature, Neck diameter, percentage of Neck growth and mean square displacement (MSD) w.r.t. sintering time. Fig. 2.19 and Fig. 2.20 shows the effect of size of particle over growth of neck growth. After 10ps of time, smooth and rapid growth of neck is visible during sintering of copper particle pair of size 1nm. But melting phenomenon also occurs, which is not desired in sintering. Neck growth during sintering 3nm pair of copper particle is almost stagnant after 17ps of time i.e. very less change in neck size with respect to time is observed. Consistent and smooth neck growth has been observed during sintering of 2nm pair of copper particles. Up to 20ps of time, neck growth is slow and after that rapid growth of neck has been observed. Also, melting phenomenon is almost nil in the case 2nm particle pair.

iii) Mean Square Displacement of atoms throughout the process of laser sintering of pairs of copper nanoparticles

The mean square displacement (MSD) is the distance of the position, that an atom dislocates throughout the process of laser heating with respect to initial or any of the reference position [14], [86]:

$$MSD = \frac{1}{N}\sum_{i=1}^{N}\left[r_i(t) + r_i(0)\right]^2 \qquad \dots (2.27)$$

Where, N = Number of atoms are considered for averaging at a fixed time *t* with reference to a reference position *r*. Output data is a vector which consist of four quantities. Among them first three of the quantities are the squared displacement of three components of the displacement vector, i.e. dx×dx, dy×dy and dz×dz. The fourth quantity is the summation of squared displacements of the components of displacement vector, i.e. (dx×dx + dy×dy + dz×dz). From the initial position or from a reference position, atom displacement is measured.

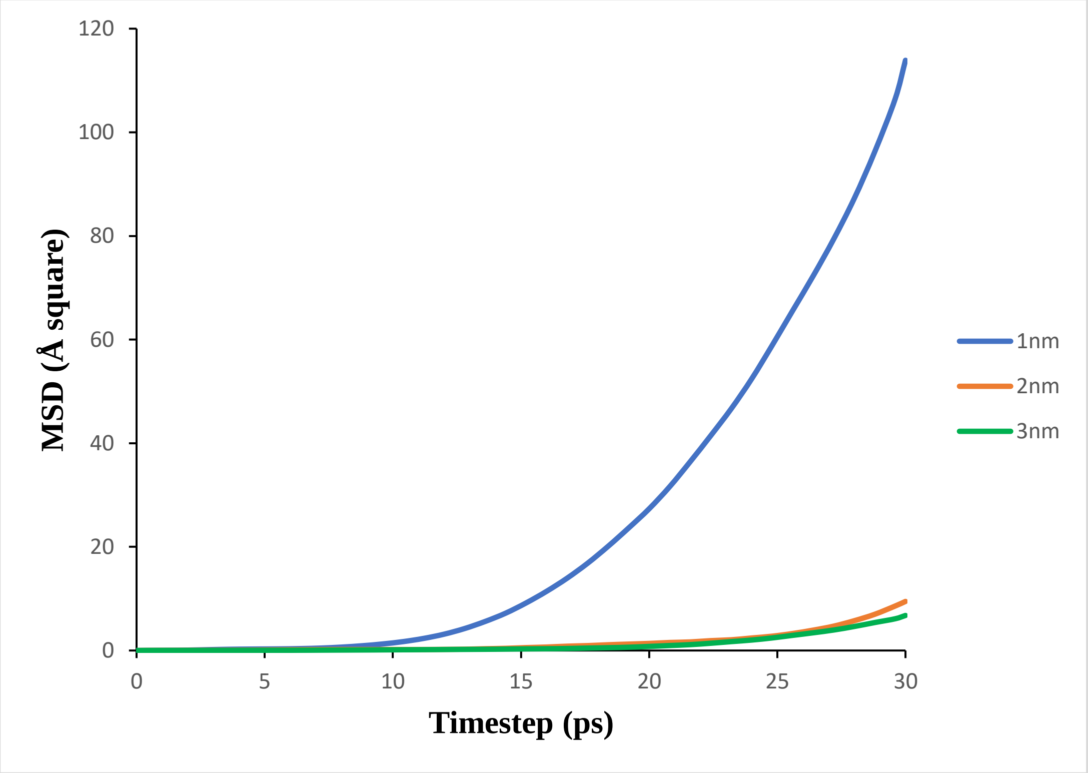

Fig. 2.21: Mean Square Displacement (Å^2) vs Time (picosecond) curve throughout the process of laser sintering of pairs of nanoparticles (following Table 2.5)

In the present research, displacement of atom is measured from the initial coordinate of that atom when heating started. Fig. 2.21 is showing MSD vs Time graph. This graph shows change in dislocation of atoms with w.r.t. time. From the graph it is revealed that atom displacement increases with time. From this it can be concluded that atom diffusion coefficient is directly proportional to the slope of the MSD vs Time curve. In Fig. 2.21, the

MSD of atoms of pairs of copper nanoparticles are compared during the sintering process. Graph shows that initially MSD of atoms is almost zero. Later, MSD is increased with time and it is maximum at the finishing point. The case of sintering of pair of 1nm copper particles, after 10ps of time significant change in MSD is noted and rapid increment is observed. This huge displacement from initial position reveals the phenomenon of thorough melting and vaporisation of material. Melting and vaporisation is not desired in the case of sintering. On the other hand, smooth MSD vs Time curve have been observed during sintering of 2nm and 3nm pairs of copper nanoparticles. Also, in both the cases the curve is near to zero MSD line during the sintering process. This indicates that the atom displacement is very small during the process of sintering. This phenomenon indicates melting and vaporisation phenomenon is almost negligible during sintering of pairs of 2nm and 3 nm copper particles. Because of this, rate of neck growth is low.

2.5.3 Molecular Dynamics Simulation-based Virtual Experiments to explore effect of particle size to minimize porosity level during laser sintering of nanoparticles under same heating rate

MD simulation-based virtual experiments of laser-sintering of copper nanoparticles are conducted. Three different models of four identical nanoparticles are prepared and Laser-sintering of copper nanoparticles of these three different models are conducted in non-isothermal conditions under same heating rate. The first model is prepared with four identical spherical nanoparticles of size 0.72nm, the second model is prepared with four identical spherical nanoparticles of size 1.82nm and the third model is prepared with four identical spherical nanoparticles of size 3.64nm are developed. Porosity has been estimated from sintering simulation of the models.

a) Atomistic model development

3D simulation box of $8 \times 8 \times 8$ nm^3 is created for each model. Periodic boundary conditions are applied on all the faces of the simulation box. Inside the simulation box the atomistic model of four copper nanoparticles are developed. The spherical Copper nanoparticles of face centered cubic (FCC) crystal structure are created inside the simulation box.

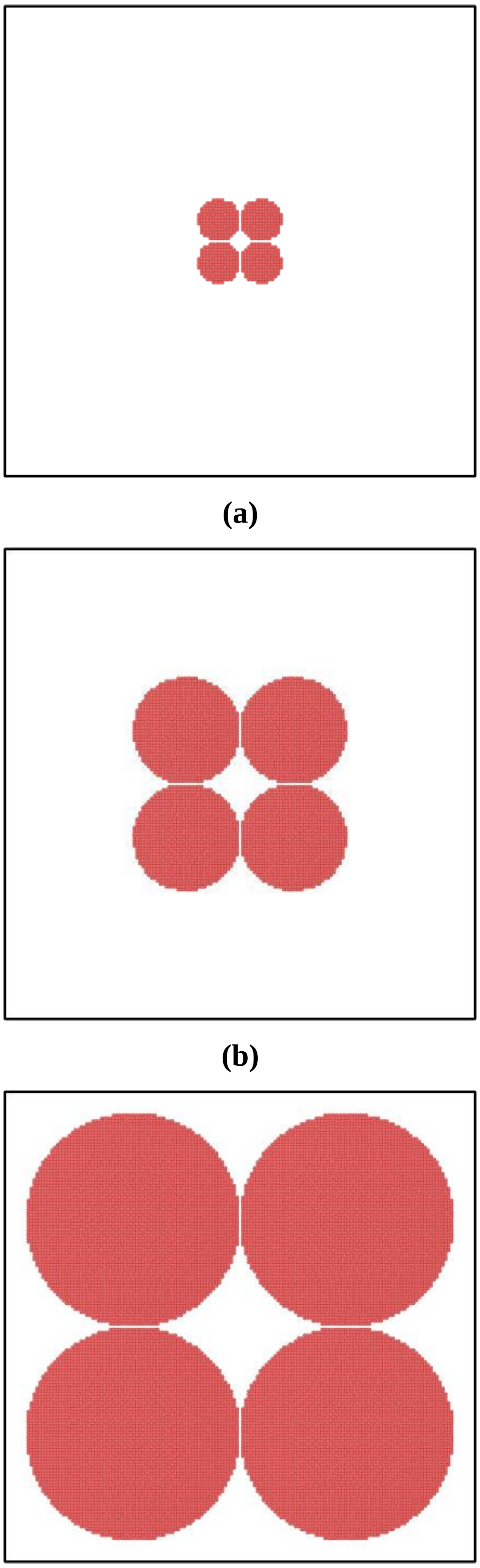

(a)

(b)

(c)

Fig. 2.22: Atomistic models of four Copper nanoparticles (a) each particle diameter 0.72nm, (b) each particle diameter 1.82nm and (c) each particle diameter 3.64nm (no gap is kept between particles)

In model (1), four spherical identical copper nanoparticles of size 0.72nm are created and they were kept in touch with each other (shown in Fig. 2.22(a)). Similarly, model (2) and model (3) are created with the spherical identical copper nanoparticles of sizes 1.82nm and 3.64nm respectively, shown in Fig. 2.22(b) and 2.22(c). Four sphere-like and identical nano-particles are present in the model (1), model (2) and model (3). Each of the particle contains 778 number of atoms in model (1) and 3112 total number of atoms. Similarly, each particle of Model (2) and (3) contain 12588, and 100964 atoms, respectively. Total number of atoms in the models (2) and (3) are 50352 and 403856, respectively. The porosity development in these models are studied during SLS.

b) Sintering Simulation Model

Initially, in each model, four identical spherical copper nanoparticles are kept in contact (as shown in Fig. 2.22) and the centre distance of the two adjacent particles are kept diameter of the particle at approximately in room temperature (300 K).

Verlet algorithm is used during randomisation of atoms to achieve control over temperature. During simulation, the copper nanoparticles of each model are subjected to continuous heating by laser beam irradiation for of 30ps of time and list of neighbouring atoms are updated at every 0.001ps time step. The heating rate is kept as 4×10^{13} K/s. During heating temperature of particles are increased from 300K to 1500K. Also, no heat loss is considered during the simulation study. The porosity level has been kept under observation in each case during sintering.

c) Results and Discussions

In each of the model is heated using the heating rate of 4×10^{13}K/s and temperature is increased from 300K to 1500K following linear equation. The four nanoparticles of each model is heated for 30ps time with time step of 0.001ps. The snapshots of sintered models of 0.72nm, 1.82nm and 3.64nm are shown in the Fig. 2.23, Fig. 2.24 and Fig. 2.25, respectively, at four timesteps 0ps, 10ps, 20ps and 30ps. Pore areas of three models are compared after 30ps of time of sintering, the snapshots reveal that they reach in different quantity of pore areas. From the Table 2.6 and Fig. 2.26, it is observed that in the model of four 0.72nm particles, pore is filled up by molten materials after 14ps time and no pore area is observed after 14ps. This phenomenon reveals that particles are fully melted and joined with each other. Whereas, in the model of 1.82nm particles, pore area gradually decreases and after 22ps of time no such remarkable change of pore area is visible. In the model of 3.64nm particles, pore area gradually decreases and after 21ps of time a remarkable increment in pore area is visible.

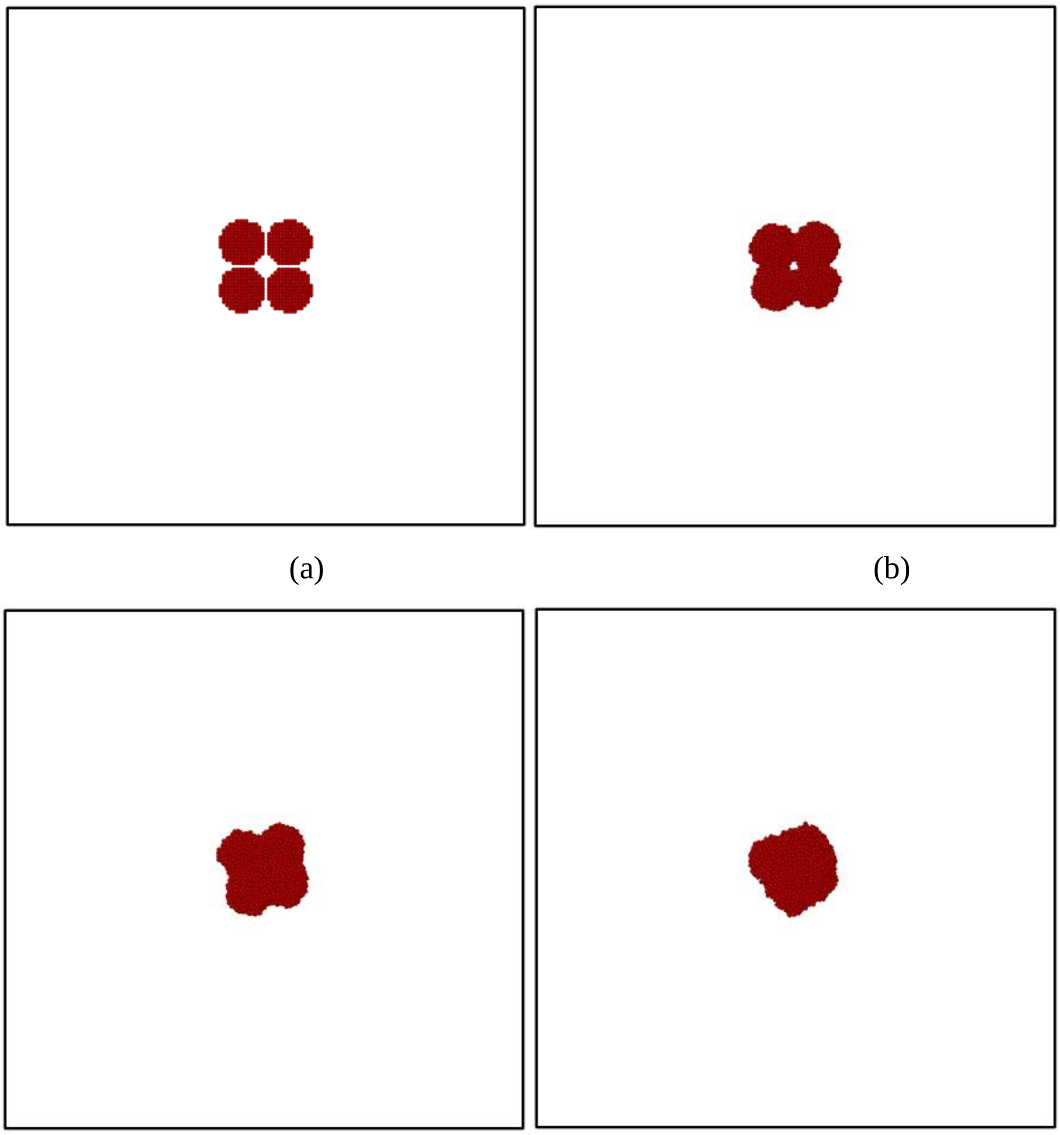

Fig. 2.23: Snapshots of sintering simulation of the model of 0.72nm sized nanoparticles at time steps (a) 0ps, (b) 10ps, (c) 20ps and (d) 30ps

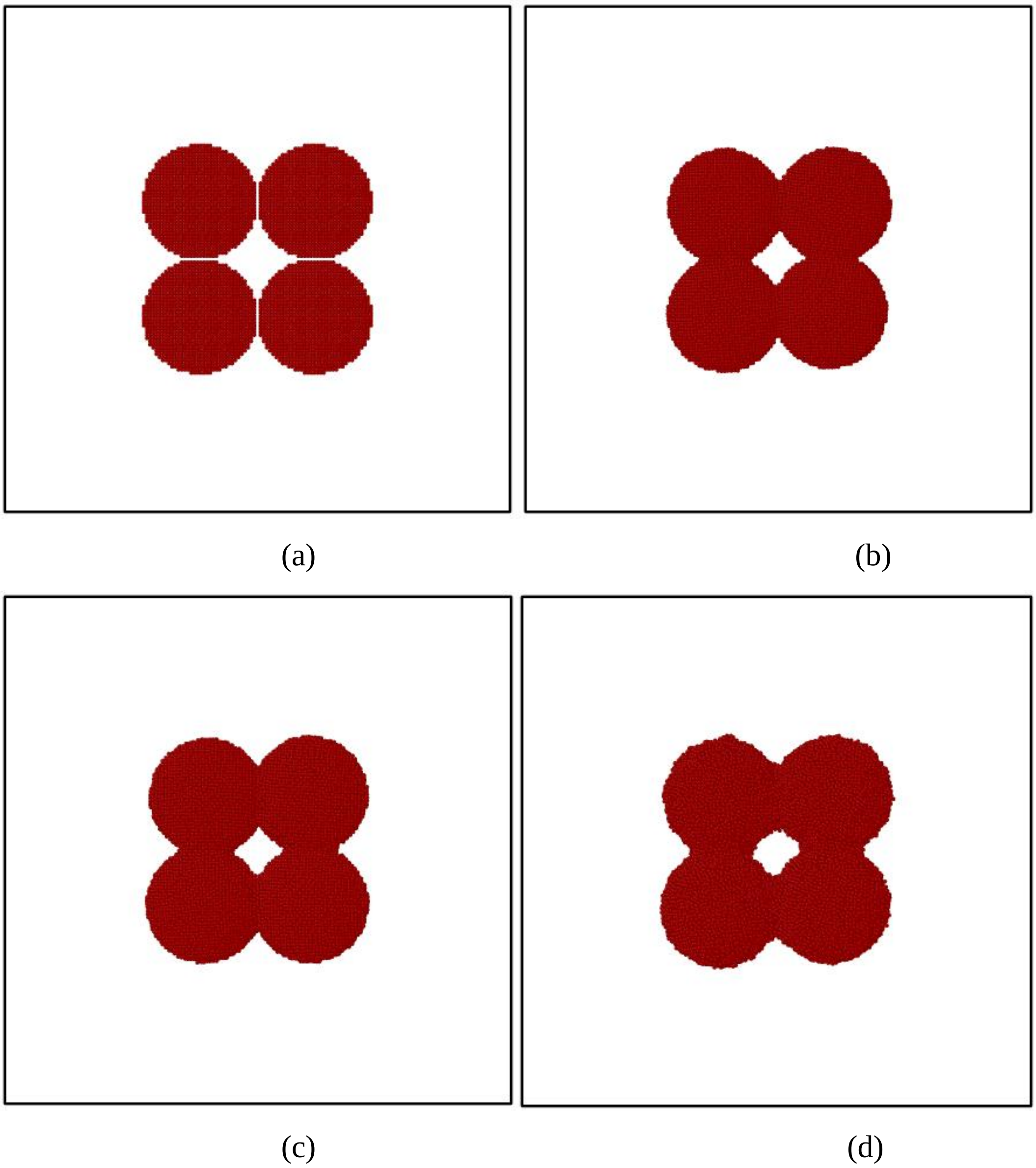

Fig. 2.24: Snapshots of sintering simulation of the model of 1.82nm sized nanoparticles at time steps (a) 0ps, (b) 10ps, (c) 20ps and (d) 30ps

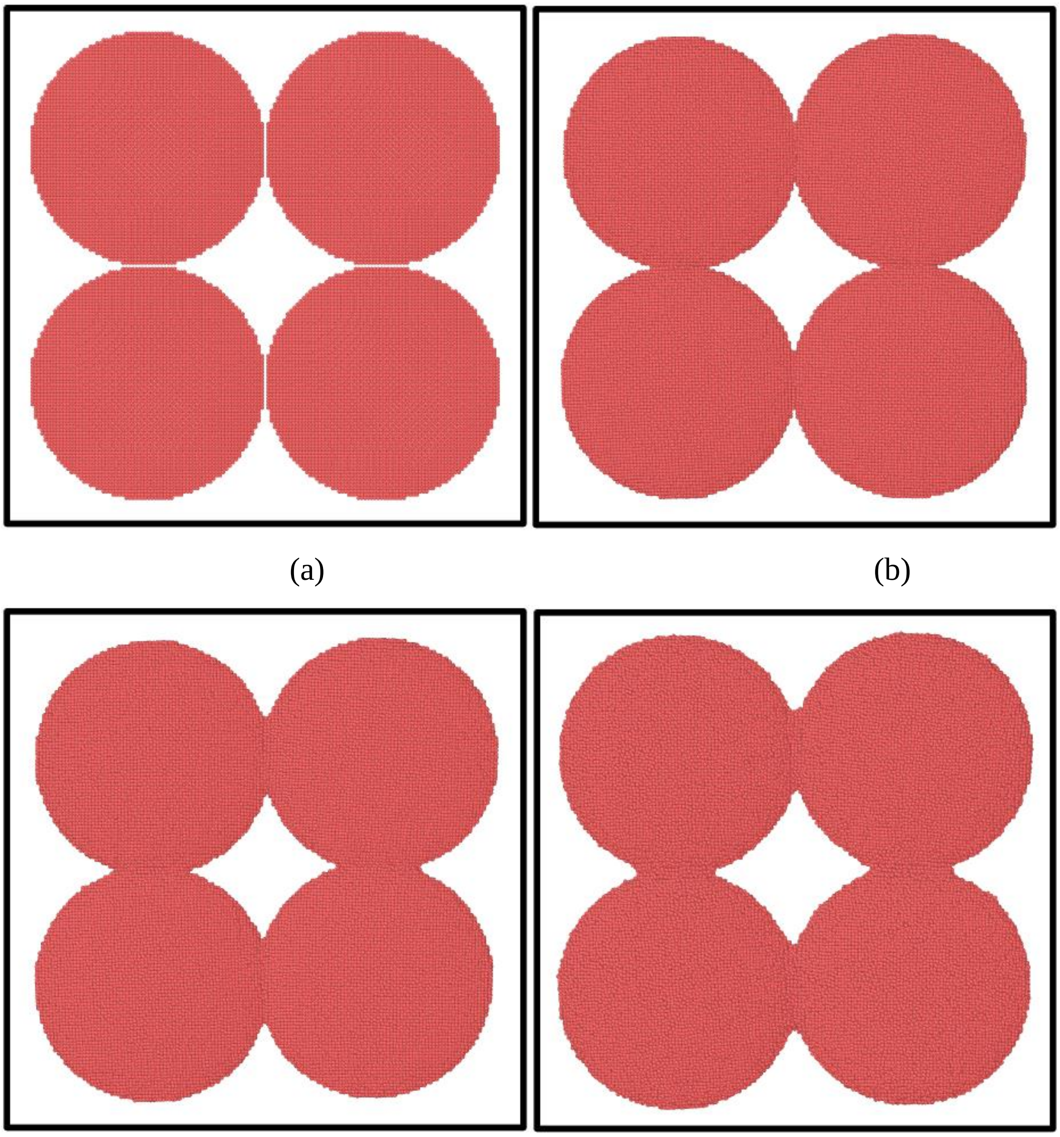

(a) (b)

(c) (d)

Fig. 2.25: Snapshots of sintering simulation of the model of 3.64nm sized nanoparticles at time steps (a) 0ps, (b) 10ps, (c) 20ps and (d) 30ps

From the snapshots (Fig. 2.23, Fig. 2.24 and Fig. 2.25), Table 2.6 and Fig. 2.26 it is observed that, at the end of sintering the 0.72nm particles melted and joined with each other and tend to become a single spherical particle. This phenomenon reveals full melting of particles, which was representing the condition of Selective Laser Melting (SLM). During sintering particle should not be fully melted, particles should be fused at less than its melting temperature and joined together. Whereas, in same heating rate 3.64nm particles and 1.82nm particles fused and joined with each other but not fully melted.

Table 2.6: Comparison of pore area in different models during sintering simulation

	Pore Area (nm square)		
Time step (ps)	**0.72nm nanoparticle model**	**1.82nm nanoparticle model**	**3.64nm nanoparticle model**
0	0.081	0.627	2.666
0.5	0.081	0.627	2.666
1	0.060	0.611	2.638
1.5	0.046	0.593	2.629
2	0.033	0.567	2.616
2.5	0.016	0.542	2.596
3	0.011	0.520	2.582
3.5	0.012	0.505	2.553
4	0.01	0.482	2.528
4.5	0.012	0.451	2.503
5	0.013	0.427	2.487
5.5	0.017	0.393	2.472
6	0.014	0.361	2.453
6.5	0.015	0.335	2.426
7	0.016	0.315	2.412
7.5	0.014	0.306	2.401
8	0.010	0.298	2.401
8.5	0.010	0.314	2.357
9	0.010	0.311	2.333
9.5	0.009	0.320	2.297
10	0.008	0.316	2.247
10.5	0.008	0.319	2.215
11	0.006	0.331	2.138
11.5	0.004	0.345	2.096
12	0.004	0.356	2.061
12.5	0.004	0.373	1.999
13	0.0003398	0.386	1.948
13.5	0.0003398	0.395	1.936
14	0.0003398	0.401	1.905
14.5	0	0.407	1.867
15	No pore	0.390	1.836
15.5	No pore	0.378	1.827
16	No pore	0.374	1.827
16.5	No pore	0.373	1.840
17	No pore	0.367	1.822
17.5	No pore	0.358	1.802
18	No pore	0.352	1.813
18.5	No pore	0.331	1.812
19	No pore	0.303	1.799

	Pore Area (nm square)		
Time step (ps)	**0.72nm nanoparticle model**	**1.82nm nanoparticle model**	**3.64nm nanoparticle model**
19.5	No pore	0.290	1.806
20	No pore	0.271	1.810
20.5	No pore	0.258	1.795
21	No pore	0.257	1.779
21.5	No pore	0.256	1.807
22	No pore	0.249	1.822
22.5	No pore	0.253	1.844
23	No pore	0.258	1.835
23.5	No pore	0.251	1.844
24	No pore	0.267	1.868
24.5	No pore	0.272	1.901
25	No pore	0.265	1.942
25.5	No pore	0.260	1.982
26	No pore	0.272	2.010
26.5	No pore	0.278	2.054
27	No pore	0.278	2.069
27.5	No pore	0.286	2.097
28	No pore	0.289	2.137
28.5	No pore	0.298	2.187
29	No pore	0.296	2.214
29.5	No pore	0.304	2.235
30	No pore	0.300	2.252

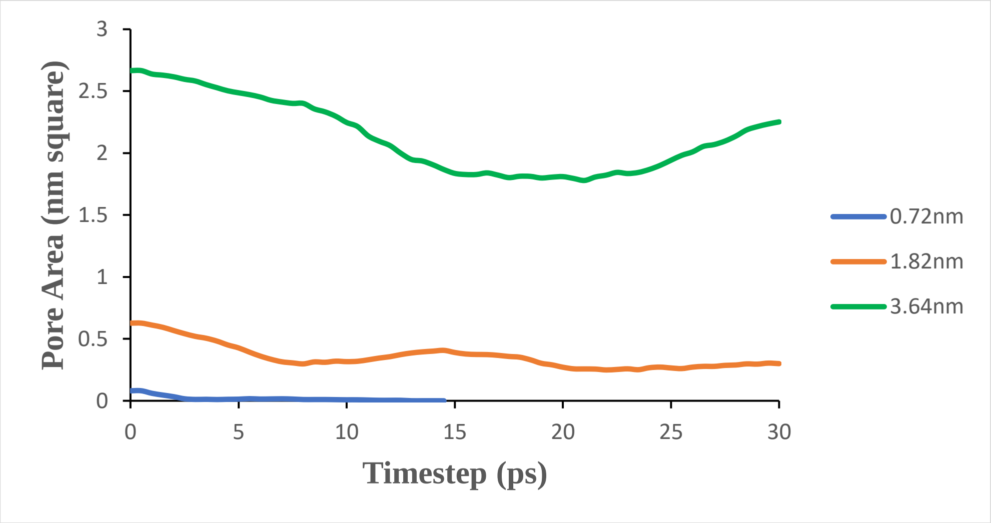

Fig. 2.26: Pore area (nm^2) vs Time (picosecond) graph during laser sintering for different models of four nanoparticle (following Table 2.6)

2.6 Summary

Molecular Dynamics-based simulation study shows that neck formation and porosity play a crucial role in laser sintering of nano-particles are optimized.

Virtual experiment of laser sintering of 1.82nm pair of copper nanoparticle is performed using Molecular Dynamics simulation by heating particles for 30ps from temperature 300K to 1444K. After completion of sintering maximum neck diameter of 1.20nm has been achieved which is about 70% of particle diameter. This indicates strong bonding between adjacent particles.

Virtual experiments of laser sintering of 1nm copper particle pair, 2nm copper particle pair and 3nm copper particle pair have been performed separately to observe the effect of particle size on growth of neck during sintering at same rate of heating. The vector plots of the atom movement during sintering reveals that surface atoms displaces towards the contact point of adjacent particles with a whirling nature of movement. The vector plots and mean square displacement of atoms also reveal that neck growth during sintering 2nm particle pair is consistent and smooth and negligible melting phenomenon occurs. Whereas, during sintering 1nm particle pair, neck formation is rapid and it has a tendency to form a single spherical particle from the two. Ultimately melting and vaporisation occurs which is not a desired phenomenon of sintering. During sintering of 3nm particle pair, neck growth is very slow or almost stagnant due to small movement in atoms. Ultimately formed neck is only 20% of particle diameter which reveals very weak bonding between two adjacent particles.

Three different atomistic models of four identical copper nanoparticles are prepared and virtual experiments of SLS are conducted using Molecular Dynamics simulations to investigate the effect of particle size in minimizing porosity level. Model (1) consists of four 0.72nm copper particles, Model (2) consists of four 1.82nm particles and Model (3) consists of four 3.64nm particles. Porosity formation between adjacent Copper nanoparticles of three different models are compared while the copper nanoparticles are heated under same heating rate. In the results it is observed that the atomistic model consisting of particle size of 1.82nm shows better neck formation and porosity level.

Whereas full melting takes place during heating the atomistic model of 0.72nm copper particles and no pore is visible and in the case of atomistic model of 3.64nm particles pore area is more due to less melting of material. The neck growth mechanism and porosity formation during sintering copper nanoparticles of the same layer has been established in this Molecular Dynamics simulation study.

The present research work is focused on the SLS of submicron sized metallic powder particles. The MD simulation-based virtual experiments have demonstrated successful neck growth and the effect of particle size in minimizing porosity level during sintering of nanosized powder particles. However, MD simulation showed good result in the range of nanometer. To conduct MD simulation-based virtual experiments in the range of micrometer length scale would take several days due to low processing power of the available computation facility. Further, to understand size effect at micrometer scale, experiments were conducted for this size of particles. During practical experiments of SLS, pulsed as well as continuous wave laser has been used to scan submicron sized metal powder.

CHAPTER – 3

INVESTIGATION OF SELECTIVE LASER SINTERING OF MICRO-SCALE COPPER POWDER USING NANOSECOND PULSED ND:YAG LASER

MD simulation-based virtual experiments has been conducted for selective laser sintering of nanometer range copper-based powder particle. MD simulation-based virtual experiments of selective laser sintering of micro-scale copper powder could not be possible to conduct due to the unavailability of simulation devices. In this chapter, investigation of neck growth mechanism and porosity formation is performed during selective laser sintering of copper-based powder of 5μm average grain size. Nanosecond pulsed Nd:YAG laser irradiation is used to conduct experiments.

3.1 Experimental Setup

a) Nano-second pulsed Nd-YAG Laser Setup

The multi-purpose laser processing setup (shown in Fig.-3.1), has been developed at Micro Systems Technology Laboratory, CSIR-CMERI, Durgapur, which has been used for micro laser sintering experiments. In this system, nano second pulsed diode pumped Nd-YAG laser system has been integrated with 3D scanner to impart laser scanning over 100mm × 100mm travel in X-Y direction. The system mainly consists of a Nd:YAG q-switched pulsed laser of which maximum output power of 7W, a scanner system (QUANTA-SYSTEM) with a computer system for controlling different process conditions.

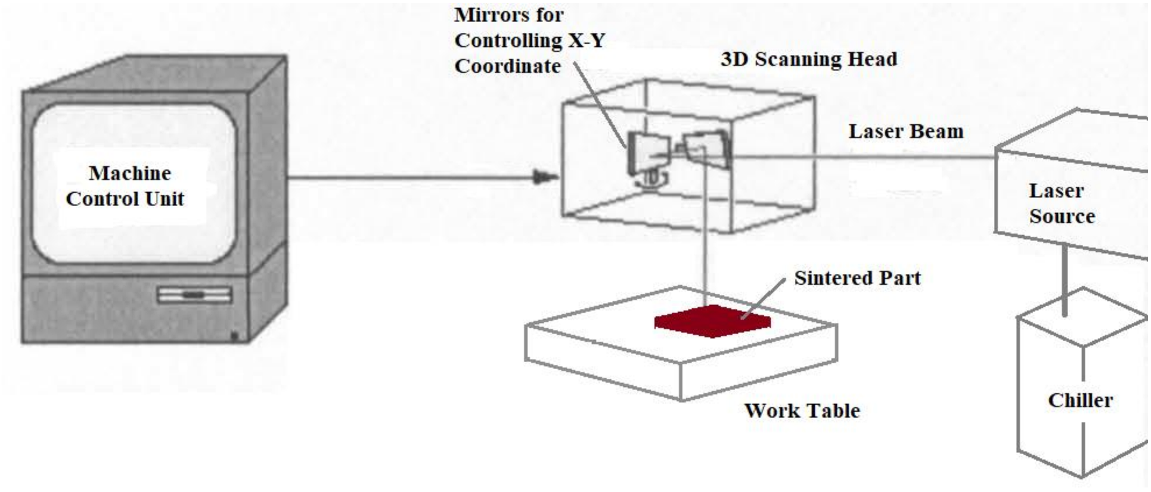
Mirrors for
Controlling X-Y
Coordinate
3D Scanning Head
Laser Beam
Machine
Control Unit
Laser
Source
Sintered Part
Work Table
Chiller

(a)

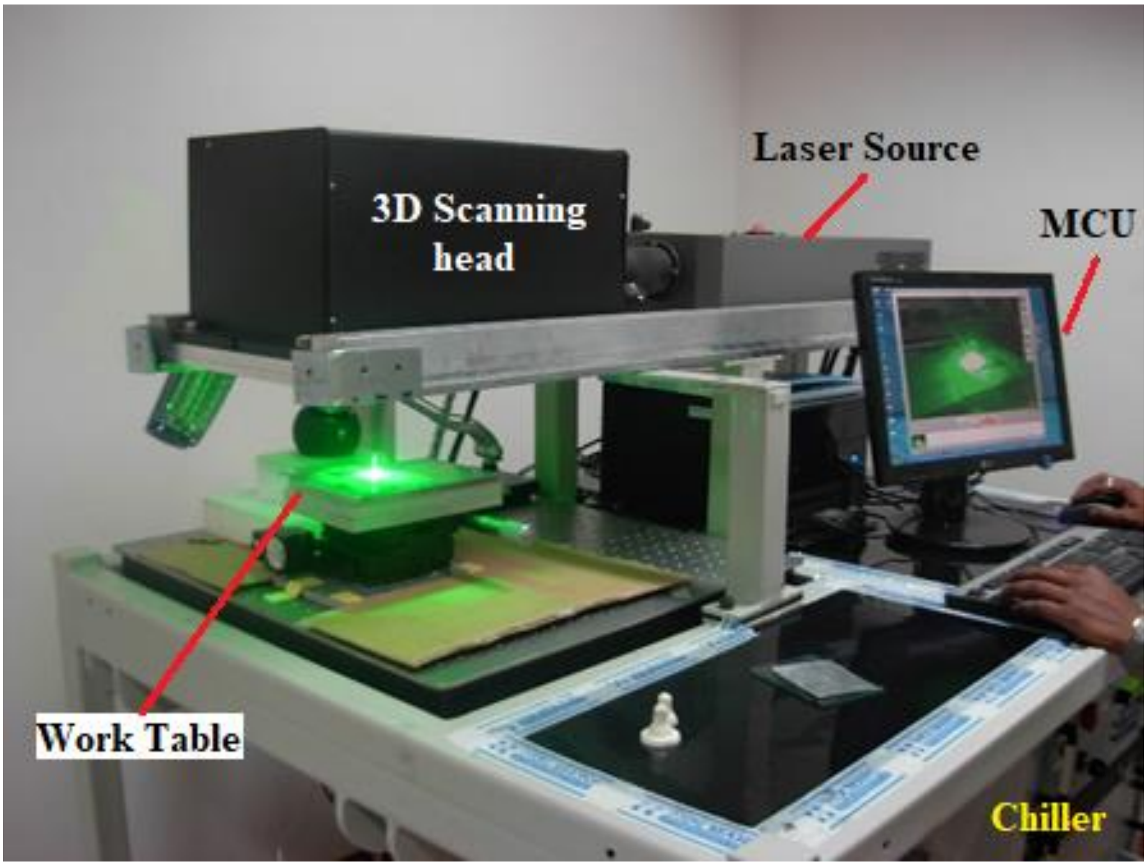

(b)

Fig. 3.1: (a) Schematic diagram of various parts of Nanosecond pulsed diode pumped Nd:YAG laser and 3D scanning head; (b) Pictorial view of Nanosecond pulsed diode pumped Nd:YAG laser system integrated with 3D scanner (QUANTA-SYSTEM)

Table 3.1: Specification of Nano-second pulsed Nd-YAG Laser Setup

i) **Laser Source:** Diode Pumped Nd:YAG, Green Laser	
Laser Head:	Model-Heera XT
Laser Material:	Nd:YAG
Average Laser Power:	12W
Pulse Width:	45ns
Wave Length:	532nm
Direct Beam Diameter through laser head:	600µm

Beam Diameter through Galvano Scanner:	10-50 µm
3D Galvano Scan area:	100×100 mm^2
Beam Quality:	M2 = 1.2 µrad
Beam pointing stability:	25 µrad
Repetition rate:	>50 kHz
Spatial Mode:	TEM00
Pulse to Pulse stability:	±2%
Cooling system:	Chiller, closed loop, filters, cartridge included
Control unit and software:	Vista based software, possible Active-X on COM server for Lab View integration
Integration and interface to workstation:	Start signal available, RS232 port for bi-directional communication
ii) **3D Scan Head:**	
Beam expander, 63mm to 100mm focusing lens, Dielectric mirrors integration with Control Software and Control board	

b) Optical Microscope

(a) (b)

Fig. 3.2 Optical Microscope

Table 3.2: Specification of Optical Microscope:

i) Model Name: OLYMPUS BX51M (Fig. 3.2(a))		
Optical System		UIS
Eyepiece		UIS
Interfaces		USB
Illumination		Reflection type
		Source of light: 100W, 12V (Built-in)
Focus		Motor-powered focus with 25mm stroke length Fine stroke of 100µm per revolution
Height range of Sample		65 mm (Max)
Stages		X-Y stage: 76mm × 52mm, with torque tuning arrangement
ii) Model Name: Leica DMI4000 B (Fig. 3.2(b))		
Display		W × H = 77 cm × 49 cm
Interfaces		USB and RS232
Illumination		Inverted type
		Source of light: Mercury lamp of 100 W
Focus		Controlled manually (both fine and coarse)
Stage	Mechanical	Immovable stage, Manual controlled, three-plate cross-stage
	Motorized	Spindle stage, Motor controlled three-plate cross-stage

3.2 Materials and Methods

During Practical Experiments of Selective Laser Sintering, micro-scale Copper powder is used. To overcome some difficulties during sintering micro-scale copper particles, Silicon Oil is used as binder material.

Table 3.3: Copper Powder

Material	Copper (Powder form)
Purity	99 %
Average grain size	5µm
Boiling Temp	2840K (lit.)
Melting Temp	1356.4K (lit.)
Density	8.94g/cc at 298K (lit.)

Table 3.4: Silicon oil as Binding Material

Binding Material	Silicon oil
Chemical Composition:	$[-\mathrm{Si}\ (\mathrm{CH_3})_2\mathrm{O}\ -]_n$
Grade:	For oil bath at more than 250ºC
Viscosity:	950 – 1050 cSt (at 25ºC)
Specific Gravity:	0.950 – 0.980 (at 25ºC)
Refractive index:	1.400 – 1.406 (at 25ºC)

Experimental Methods

For experiments copper powder of average grain size 5µm is chosen and is scanned selectively using diode pumped Q-switched Nd:YAG nanosecond pulsed laser. Various process parameters during selective laser sintering of copper powder are considered as Laser Power, Scanning Speed, Binding Materials, Hatch Spacing. With the help of pulsed Nd:YAG laser copper powder are scanned in two different phases. Initially, dry copper powder is scanned under the laser beam and later copper powder is blended with binding material to overcome some difficulties faced during dry sintering procedure.

a) Sintering Dry Copper Powder

Coating of 5µm Copper powder is quite difficult. The difficulty is caused by lumps of powder formed with moisture. Therefore, powder is preheated for 60 minutes in a temperature-controlled heating oven at temperature of 150ºC to remove moisture content. The near dry copper powder is coated on Aluminum base plate almost consistently with the help of soft buffs attached to a circular disc. The different processing parameters include spot size, laser power, pulse width, scanning speed and minimum scan spacing. The layer of almost dry copper powder is scanned at three different laser powers keeping other parameters constant as shown in Table 3.5. The hatch strategy and hatch space used during laser scan is shown in Fig. 3.3. During scanning of dry copper powder, it is observed that, the dry powder particles displaced and flow away from the powder bed from the path of laser scan.

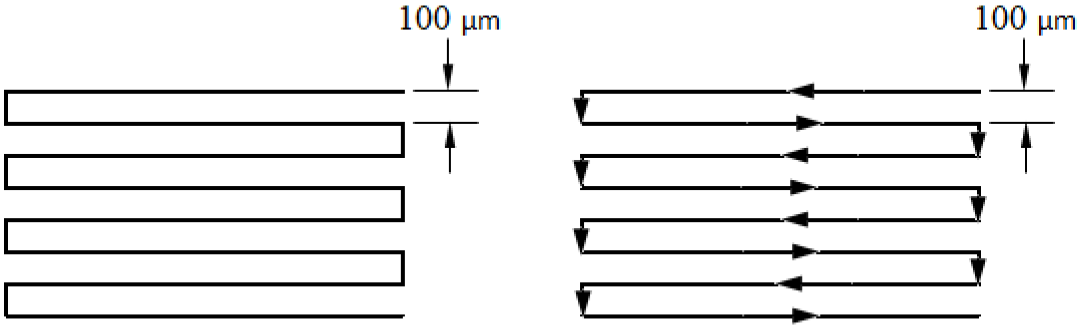

Fig. 3.3: Type of hatch and hatch space during Selective Laser Sintering of Micro-Scale Copper Powder Using Pulsed Nd-YAG Laser

Table 3.5: Various Laser Parameters used for SLS of almost dry Copper Powder in Diode Pumped Nanosecond-pulsed Nd:YAG laser

Power (W) (50%)	Scanning speed (mm/s) (80%)	Frequency (kHz)	Spot size (µm)	Pulses (ns)	Hatch space (µm)
2.5	20	3.009	200	4000	100
3.5	20	3.009	200	4000	100
4.5	20	3.009	200	4000	100

b) Sintering Copper Powder blended with binding material

Displacement problem of submicron size loose powder has been resolved to a great extent by using two material components. Copper powder is blended with binder material. The various binder material e.g. water, Polydimethylsiloxane (PDMS) and Silicon Oil is used. It is observed that Silicon oil as binder during sintering work successfully. Silicon oil is blended with copper powder in weight ratio of 2 : 3 (Silicon oil : Copper Powder). The copper powder blended with silicon oil is coated over a glass slide. At this condition laser sintering is successfully performed by adding material layer-layer-layer with an average layer thickness of 70µm. A part of 10mm×10mm×1.2mm with a free-standing rib section of 800µm thick to the height of 500µm at the top surface has been successfully sintered up to 21 layers. Fig. 3.4 shows the first miniaturized laser sintered part built using 5µm copper powder. The size of sintered part is 10mm×10mm×1.2mm. For all layers the various laser parameters used are shown in the Table 3.6.

Table 3.6: Various Laser Parameters used for SLS of Copper Powder blended with Silicon Oil (binder material) in Diode Pumped Nanosecond-pulsed Nd:YAG laser

No. of Layers	Power (W) (80%)	Scanning speed (mm/s) (80%)	Frequency (kHz)	Spot size (μm)	Pulses (ns)	Hatch space (μm)	Total no. of scans per layer
21	7	20	3.009	200	4000	100	10

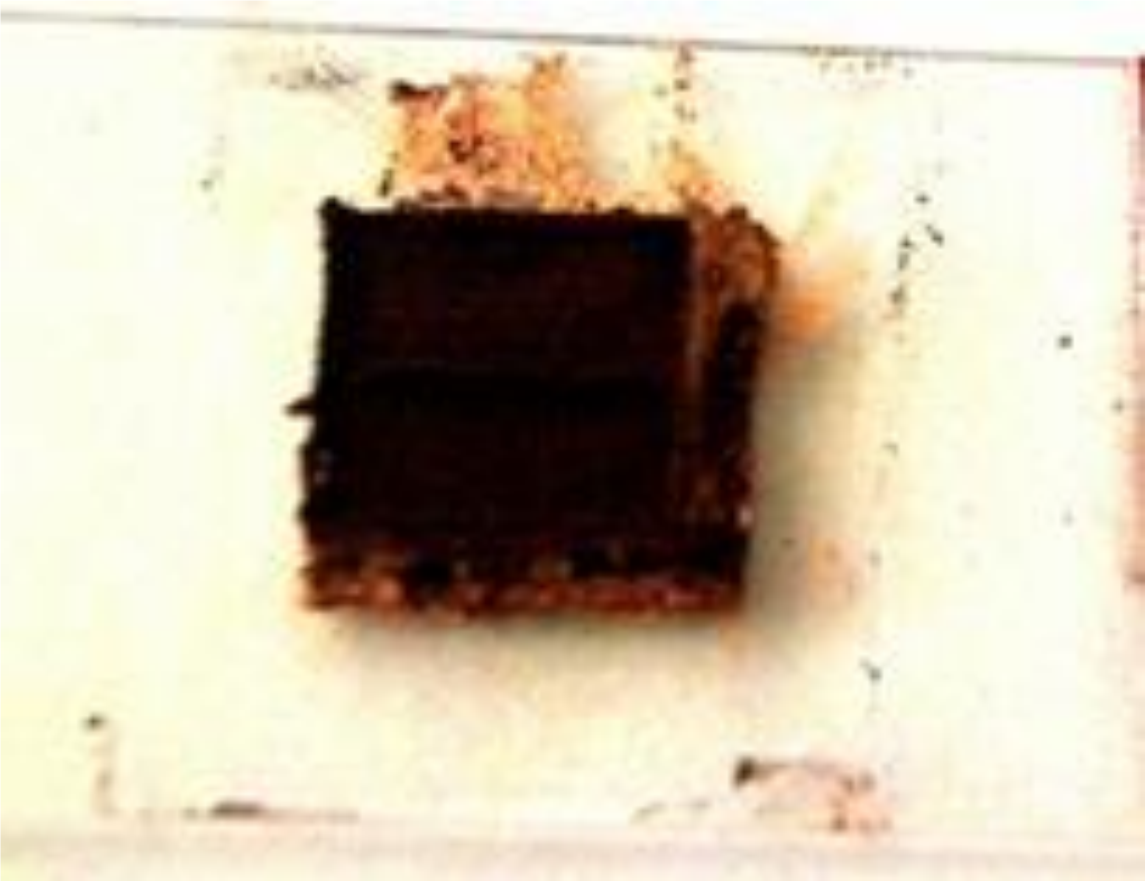

Fig. 3.4: Miniaturized laser sintered part of Copper Powder blended with Silicon Oil

After sintering of 21 layers one over the other the sintered part is separated from the base i.e. the glass slide. Then the laser sintered part is placed inside the oven, and then cured slowly at 350ºC at controlled rate for several hours as an attempt to remove residue of silicone oil.

3.3 Results and Discussions

a) Observations during and after sintering of copper powder

Keeping loose dry powder on the base plate becomes a daunting task, as it flies out of the track of laser scanning. This is attributed to the balling effect formed due to surface tension during the liquid phase sintering. The layers of dry copper powder before and after sintering are observed under optical microscope. The Fig. 3.5(a) shows the microscopic view of the layer of dry Copper Powder before sintering. The Fig. 3.5(b) shows the sintered copper powder in dry condition. Loose dry powder has been flying out during scanning successive layers of dry copper powder using pulsed laser irradiation. Due to surface tension of molten metal is shrunk, during sintering. Due to this shrinking phenomenon, the balling effect occurs during sintering process. This makes the sintering process more critical. In the Fig. 3.5(b) the balling effects during sintering is clearly visible.

Later, Silicon Oil as binder material is blended with the copper powder and is scanned under laser beam to overcome the dislocation of copper powder from that track of laser scan. Fig. 3.6(a) is showing the microscopic view of layer of Copper powder blended with Silicon Oil before sintering. The view of sintered part under optical microscope is shown in Fig. 3.6(b). Selectively Laser Sintered Micropart is shown in Fig. 3.4 and it is found to be weak and fragile. It also contains the residue of silicon oil. Therefore, sintered part is cured at 350ºC for several hours inside the controlled temperature electric heating oven that helps in removing the residues of binding materials.

b) Characterization of sintered part

The Sintered part produced by scanning dry copper powder and mixture of copper powder and silicon oil are observed under optical microscope and Scanning Electron Microscope (SEM) for further analysis. Fig. 3.7 is showing SEM micrographs of sintered part using binder material. It shows promising results with respect to sintering, formation of near spherical particles recoiled from the molten melt are clearly observed although complete removal of silicon oil is not possible at these conditions. For further analysis the sintered parts are inspected under SEM.

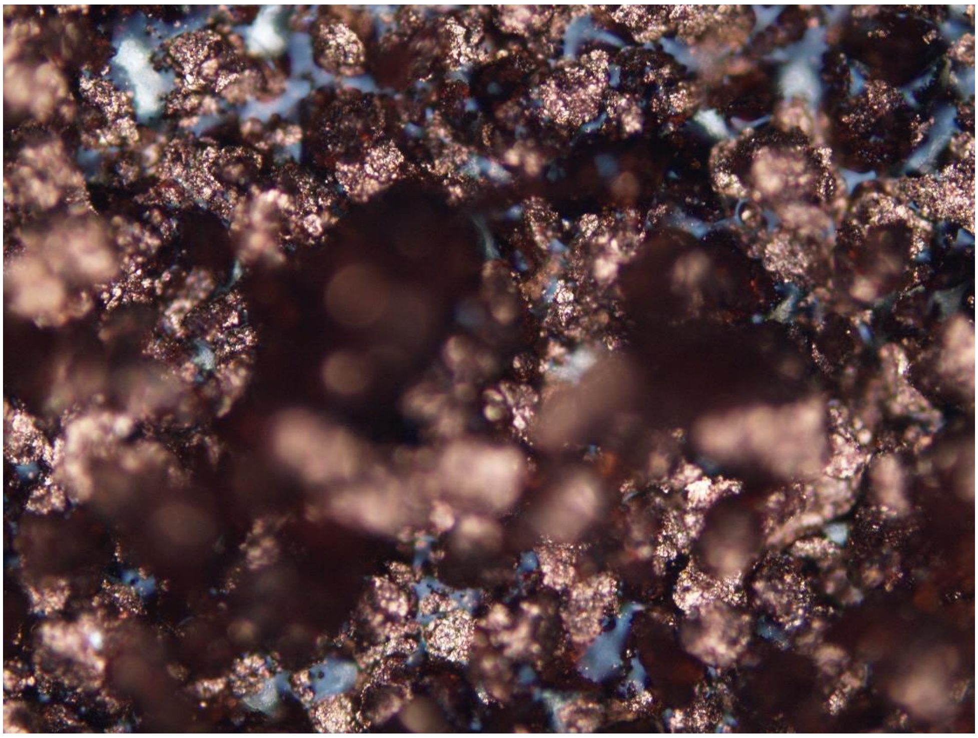

(a) Layer of Copper powder;

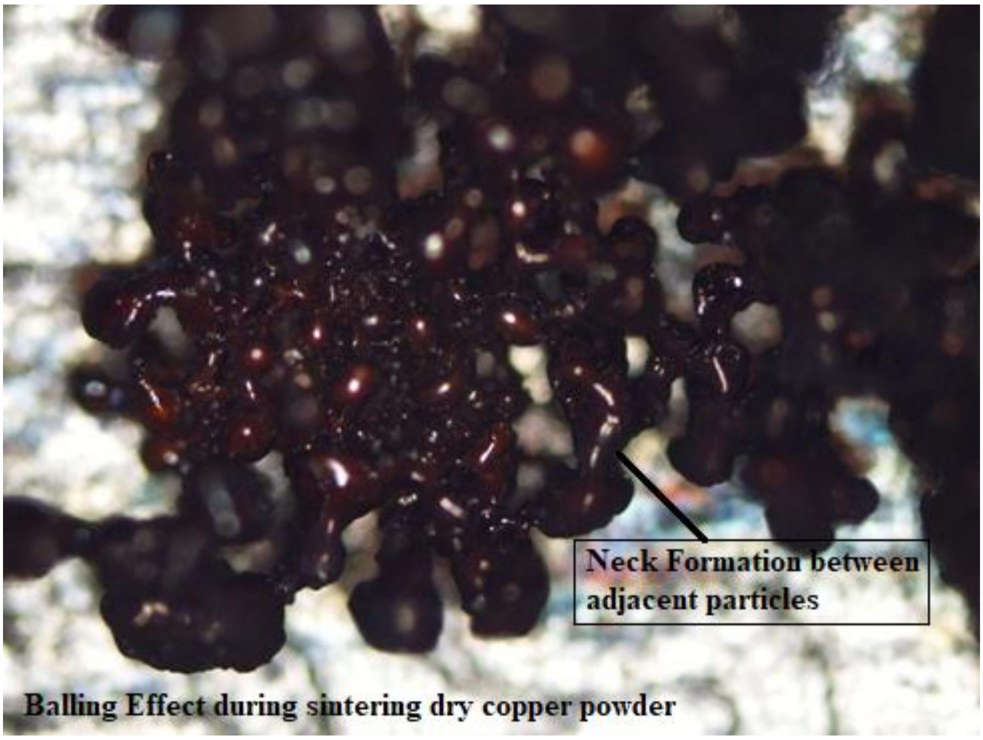
Neck Formation between adjacent particles
Balling Effect during sintering dry copper powder

(b) Sintered dry copper powder;

Fig. 3.5: Micrographs of selective laser sintered dry copper powder of 5µm average particle size

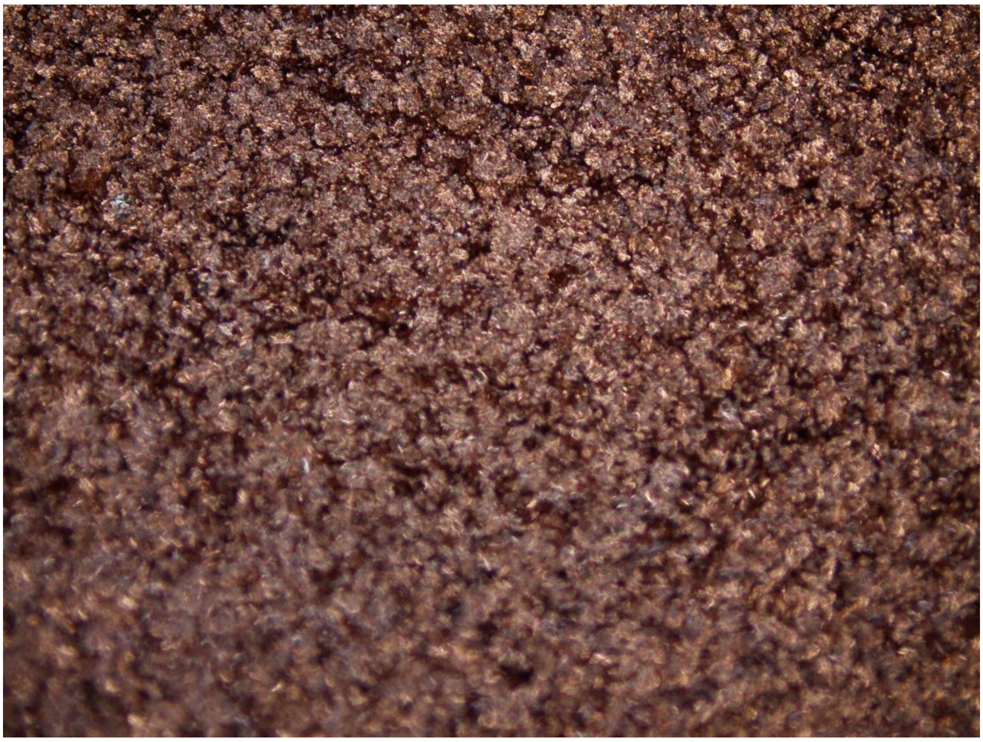

(a) Copper powder with Silicon oil (before sintering);

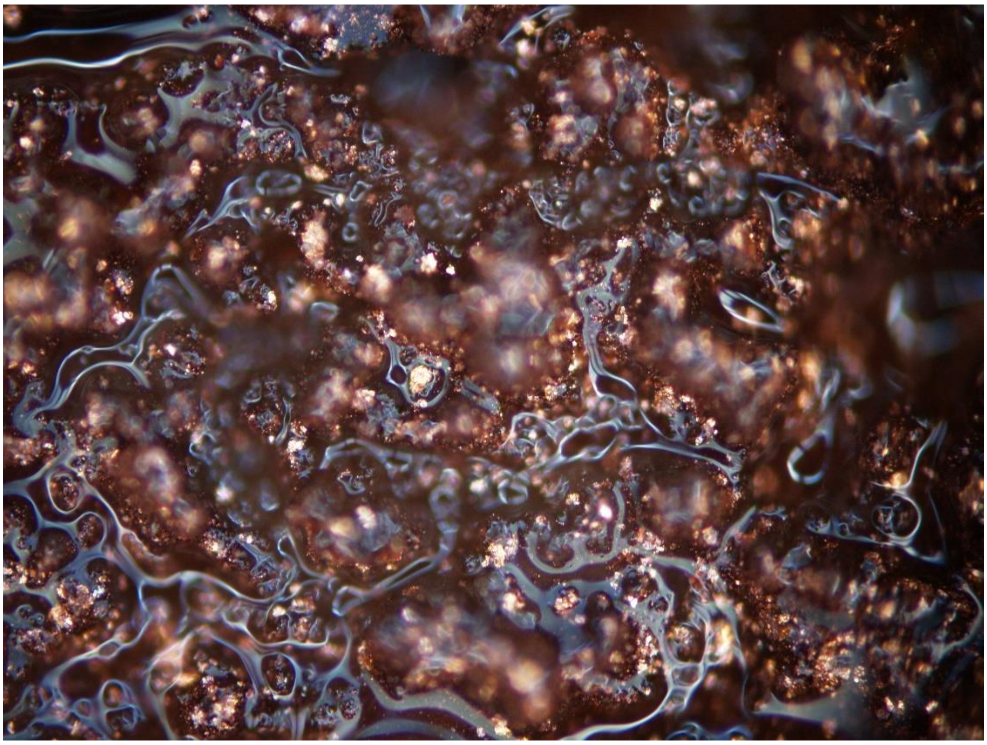

(b) Sintered powder layer with Silicon oil binder;

Fig. 3.6: Micrographs of selective laser sintered copper powder of 5µm average particle size blended with silicon oil

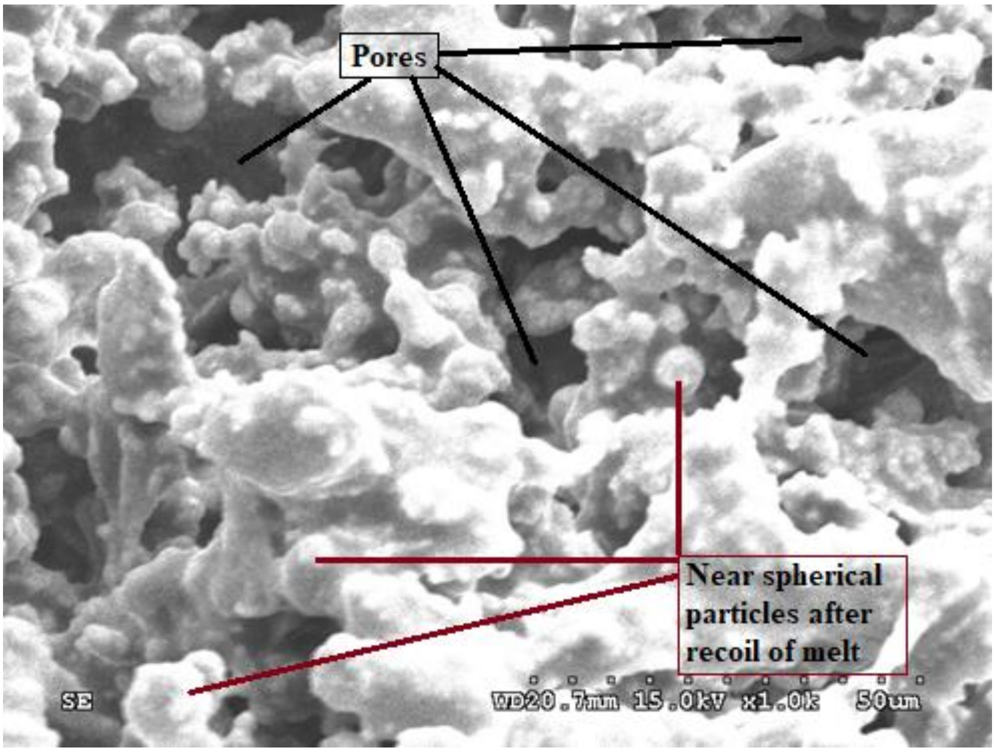
Pores
Near spherical particles after recoil of melt
SE
WD20.7mm 15.0kV x1.0k 50um

(a) Near spherical particle after recoil of melt and porosity

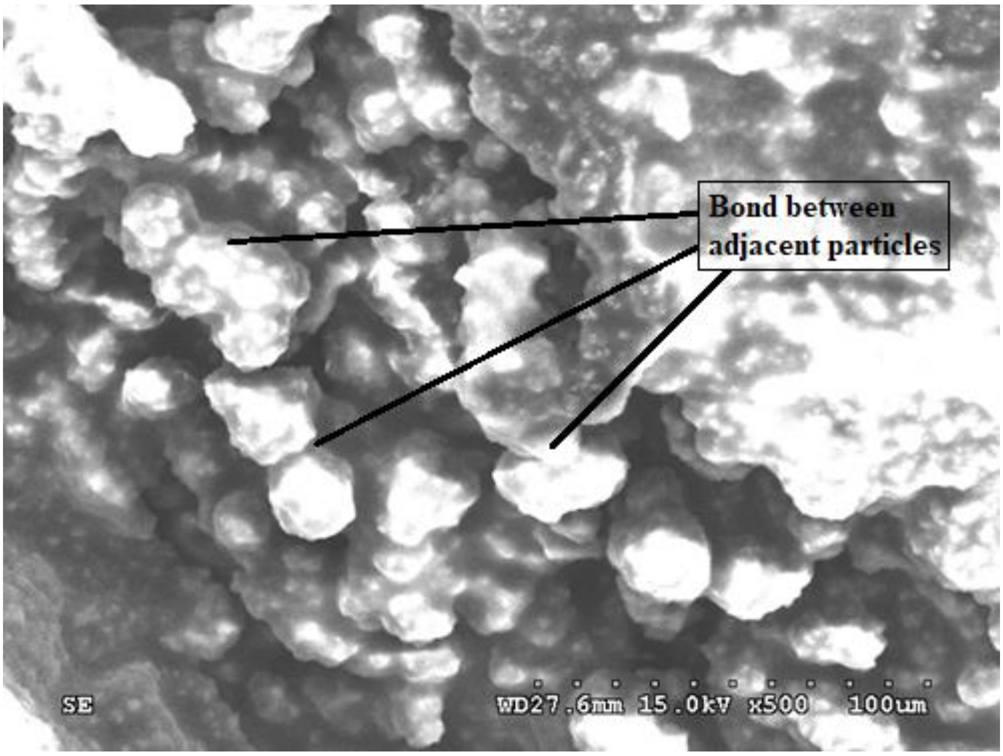
Bond between adjacent particles
SE
WD27.6mm 15.0kV x500 100um

(b) Bonding between adjacent particle

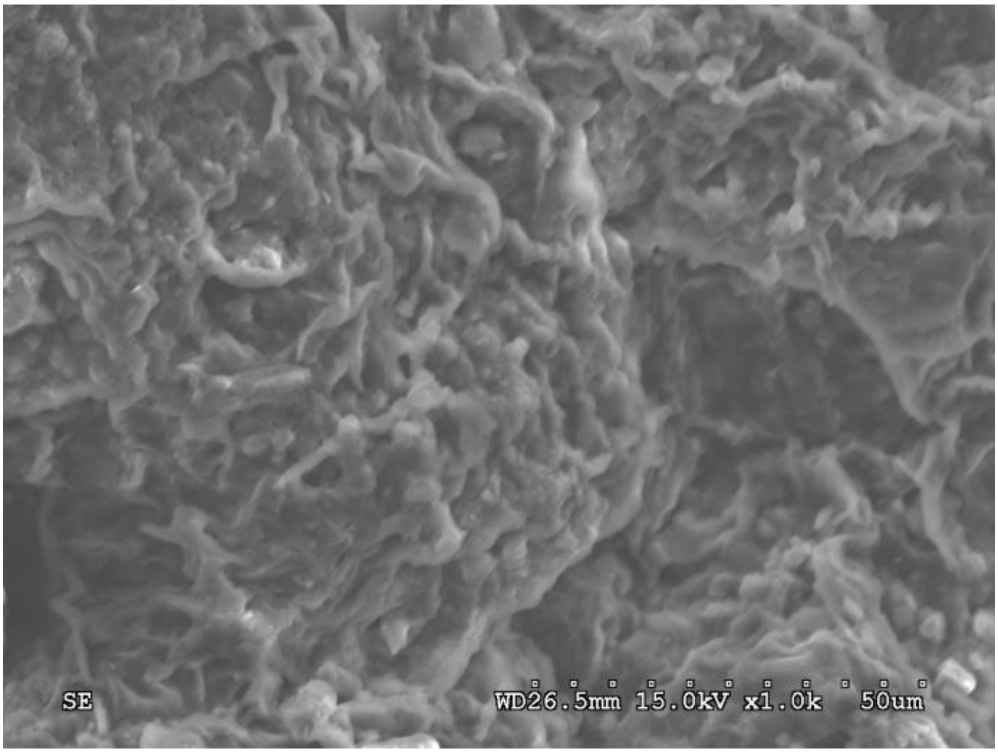
SE
WD26.5mm 15.0kV x1.0k 50um

(c) Uniform eruption on sintered surface

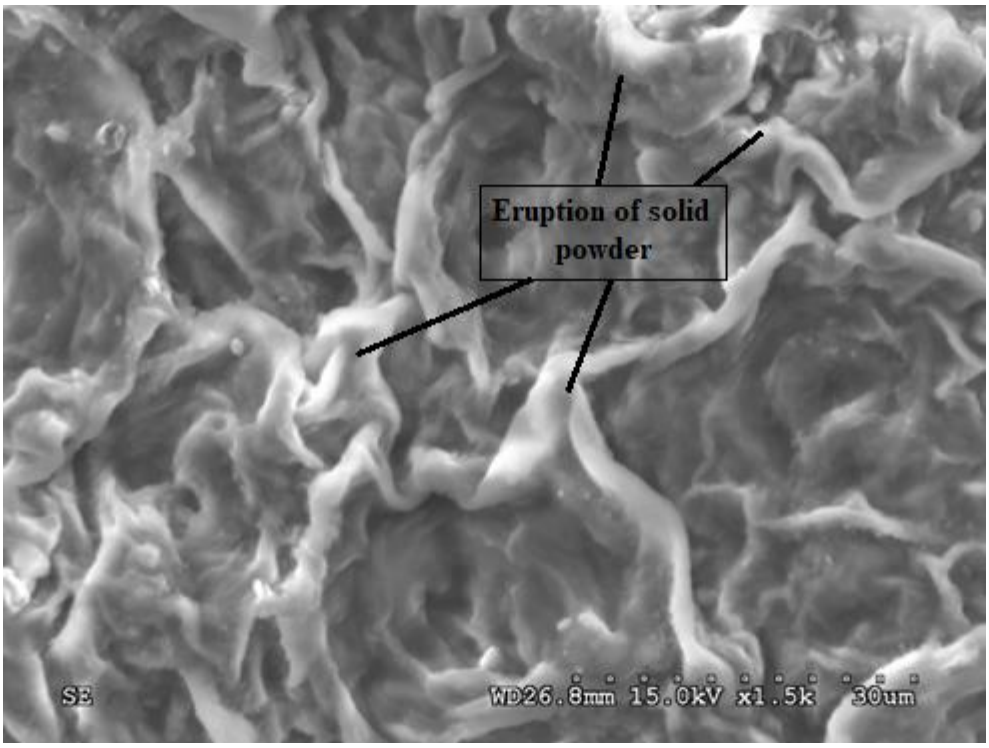
Eruption of solid powder
SE
WD26.8mm 15.0kV x1.5k 30um

(d) High intensity processing shows eruption of solid powder

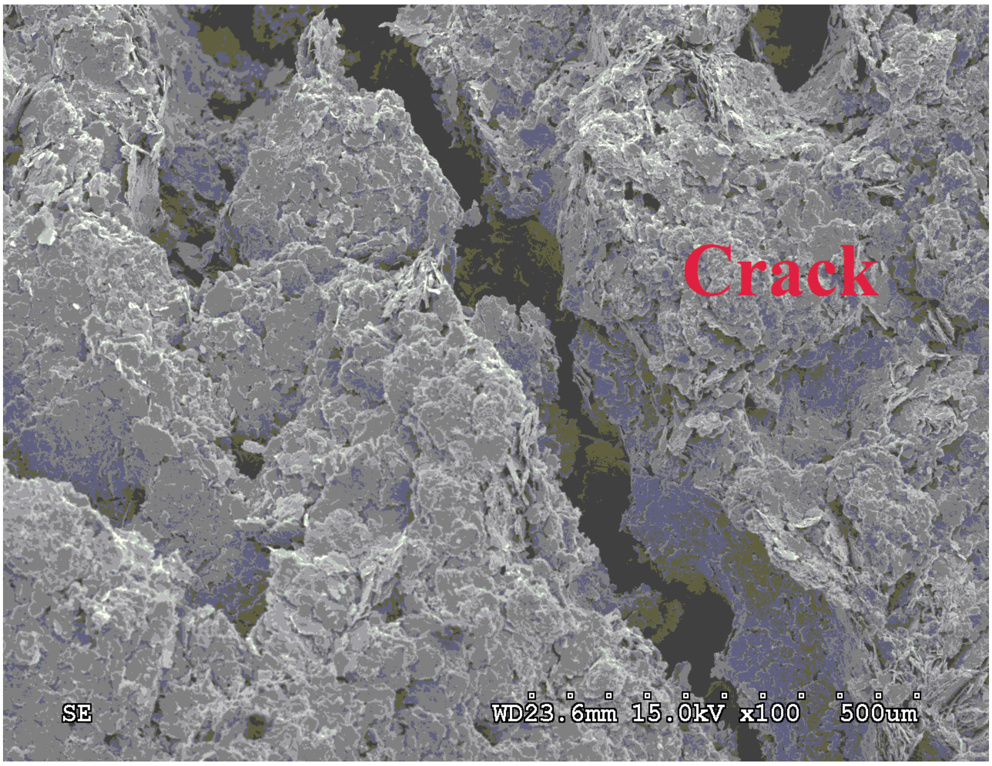
Crack
SE
WD23.6mm 15.0kV x100 500um

(e) Presence of internal cracks

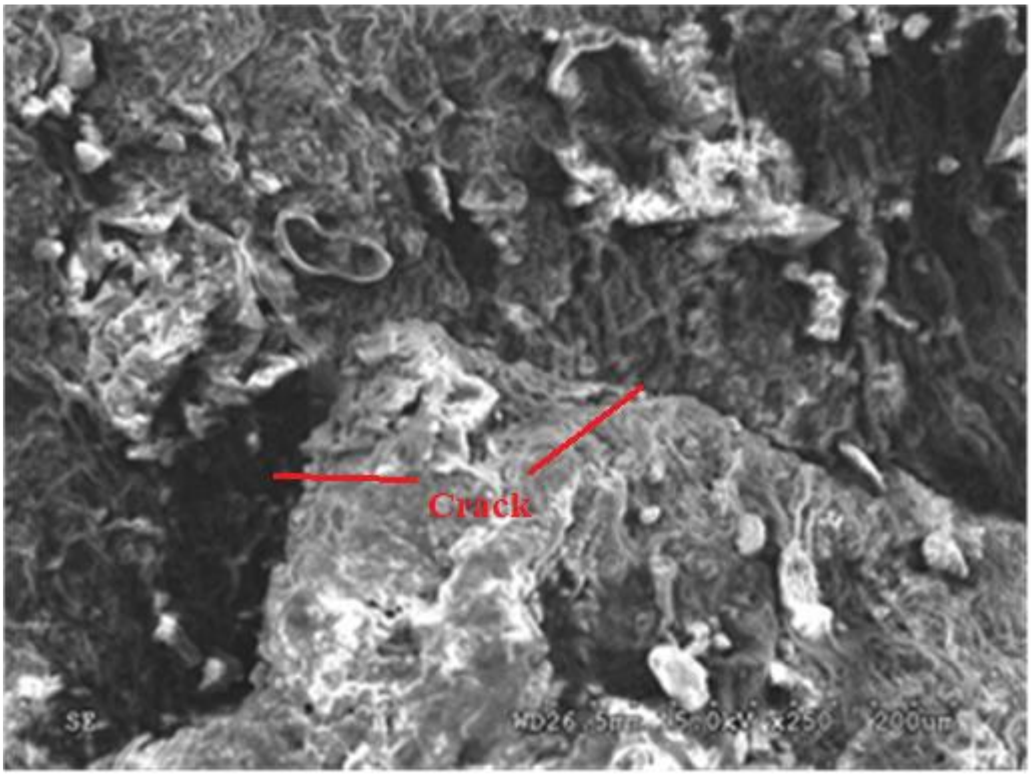
Crack
SE
WD26.5mm 15.0kV x250 200um

(f) Presence of internal cracks

Fig. 3.7: Micrographs of selective laser sintered copper powder of 5μm average particle size blended with silicon oil

i) Neck growth during sintering of dry powder is clearly visible from the microscopic view in Fig. 3.5(b). During sintering of copper powder with binder material neck growth is proper as visible in the SEM micrograph in Fig. 3.7(a) and 3.7(b). In Fig. 3.7(c) the SEM micrograph shows uniform eruption of material from the solid powder. High laser intensity with low frequency pulses cause more eruption and leave more rough surface that facilitate vertical cross linking between successive layers (Fig. 3.7(d)).

ii) Though bonding between adjacent particles is clearly visible. Still porosity is observed during sintering of copper powder in dry condition as well as with binder material. From the microscopic view (Fig. 3.5(b)) of dry sintered copper powder, it is observed that, due to shrinkage of powder particles (balling effect) large pores in large numbers are created. Using binder material, the shrinkage and balling phenomenon is avoided to some extent. Still porosity is visible in the SEM micrograph (Fig. 3.7(a)). One of the major limitations observed here is presence of surface and internal cracks (Fig. 3.7(e) and Fig. 3.7(f)).

c) Effect of process parameters

Dry copper powder is sintered in different laser power as shown in Table 3.5. But after laser scanning the dry copper powder layer with laser power of 7W, a few of powder particles are visible on the substrate. Powder particles has been flying away from the track of laser beam due to high intensity of laser. Later, laser power is decreased and at a laser power of 1.25W (i.e. 50% of 2.5W) good bonding between adjacent particles is visible in the microscopic view (Fig. 3.5(b)). It is observed that powder particles are flowing away from the powder layers due to intensity of laser. During condensation and solidification of molten metal shrinks. From the microscopic view it is observed that when the dry powder layer is scanned under the laser beam, a lot of pores are created after solidification of the sintered part. These pores are visible under optical microscope. Porosity and displacement from the track of laser scanning during sintering by using three different powers, very little difference is observed. To overcome these difficulties binder material is selected and mixed with powder material for sintering.

Application of binder material during sintering procedure, the porosity become less. Due to adhesiveness of binding material during scanning under laser beam powder particles could not flown away from the layer and sintering occurred effectively. It is also observed that during condensation and solidification of sintered part less shrinkage is taken place. Due to less shrinkage of powder material porosity become less and sintered part become much solid than the dry sintered part. Comparing microscopic view of dry sintered copper powder (Fig. 3.5(b)) and the SEM micrographs of sintered copper powder with binder material (Fig. 3.7), it is visible that bonding between adjacent particles and layers is increased as well as the porosity level is decreased in laser case.

3.4 Summary

Experimental investigation of selective laser sintering of 5µm copper particles have been performed to explore the neck formation and porosity formation between adjacent particles. Nanosecond pulsed Nd:YAG laser irradiation is used to conduct sintering experiments. Experiments are conducted in two different phases, in dry conditions (without binder) and in viscous conditions (with binder). Initially, dry copper powder is scanned under the pulsed laser beam and later copper powder is blended with binding material to overcome some difficulties faced during dry sintering procedure.

Initially, it is difficult to coat dry copper powder of 5µm average grain size. The difficulty is caused by lumps of powder formed with moisture. Therefore, powder is preheated for an hour in a temperature-controlled heating oven at temperature of 150ºC to remove moisture content. After removal of moisture, the lumps are broken and the loose powder is coated over an aluminium substrate with the help of soft buff fixed with circular disc. Sintering of dry copper powder has been performed using different laser power. In dry conditions sintered powder forms near spherical balls as a result of recoil of molten melt surrounding the solid material. Under the pressure induced by the laser pulse irradiation, dry powder particles are flying-off from the laser intensity track leaving gaps that make addition of successive layers difficult.

This problem has been solved by blending of copper powder with little quantity of silicone oil. This viscous paste makes coating of powder easy, resulting in consistent coating thickness in every layer. 21 layers of copper particles is successfully sintered, to build a rectangular part of 10mm×10mm×1.2mm having free standing rib section of 800µm thick to the height of 500µm. However, use of silicone oil demands higher laser power (7W) compared to 4.5W power used in dry conditions.

At the processed conditions, neck growth mechanism of sintering is appreciable; Formations of near spherical particles as a result if recoiling of molten melts is observed. The SEM micrographs show uniform and rough surface caused by material eruption that would facilitate effective cross linking between successive layers. However, in the present processing conditions, part of silicon oil did not undergo polymerization. This residue forms several surface and internal cracks making the sintered part fragile.

i) The selective laser sintering of submicron (5µm) sized copper powder using Q-switched nanosecond pulsed Nd:YAG laser has shown successful neck growth between adjacent particles. Neck formation is appreciable in both the cases of sintering i.e. sintering of copper powder with and without binder materials.

ii) Porosity formation showed major limitation of sintering during scanning of dry copper powder under laser beam. During sintering of dry copper powder, the sintered part forms near spherical balls as a result of recoil of molten melt surrounding the solid material. This phenomenon is known as balling effect. Due to balling effect a lot of pore areas are created during sintering. Using silicon oil as binder material, the phenomenon of balling effect has been avoided and porosity level is minimized.

iii) Presence of residual of silicon oil is observed in the sintered part and it is removed by heating the sintered part for several hours. Due to removal of residual of silicon oil, the sintered part become fragile and some internal crack is visible in the SEM micrographs.

Similar phenomenon of neck growth formation and porosity formation is observed during the SLS of 5µm copper powder using nanosecond pulsed laser which has been observed during MD simulation-based virtual experiments of laser sintering of nanosized copper particles. Porosity level is increased due to increment in particle size.

CHAPTER – 4

INVESTIGATION OF SELECTIVE LASER SINTERING OF MICRO-SCALE COPPER POWDER USING CONTINUOUS WAVE LASER

Virtual experiments employing Molecular Dynamics simulation has been performed for selective laser sintering of nanometer range copper-based powder particles. Virtual experiments of selective laser sintering of micro-scale copper-based powder employing Molecular Dynamics simulation is not possible to conduct due to the unavailability of simulation workstations. In this chapter, the same investigation of neck growth mechanism and porosity formation is performed during selective laser sintering of copper-based powder of 5μm average grain size. Continuous Wave Fibre Delivered Diode Laser and Continuous Wave Fibre Array Packages (FAP) Diode Laser irradiation are used to conduct experiments.

4.1 Experimental Setup

Experimental Sets up used in the present research are as follows:

1. Continuous Wave Fibre Delivered Diode Laser Setup
2. Continuous Wave Fibre Array Packages (FAP) Diode Laser Setup

4.1.1 Continuous Wave Fibre Delivered Diode Laser Setup

This set up is the multi-purpose laser processing setup (shown in Fig. 4.1) has been developed in the lab of CSIR-CMERI, Durgapur, which has been used for micro laser sintering experiments. This continuous wave (CW) 1200 W Fibre Delivered Diode Laser system is synchronized with computer interface. A three-axes CNC work table is associated with the laser system. Motion system of CNC work table is controlled by computer interface.

A) **Laser source:**

1. Diode laser fibre delivered (300 μm fibre dia.)
2. Power: 1200W
3. Focussing diameter: 480 μm at Focal length 150 mm
4. Wavelength: 976 nm
5. Make: Laser: Dilas
6. Profile: Gaussian
7. Distance from laser head to substrate: 100 mm

B) **CNC stage:**

1. platform: 400 × 400 mm
2. velocity: 0 – 75 mm/s

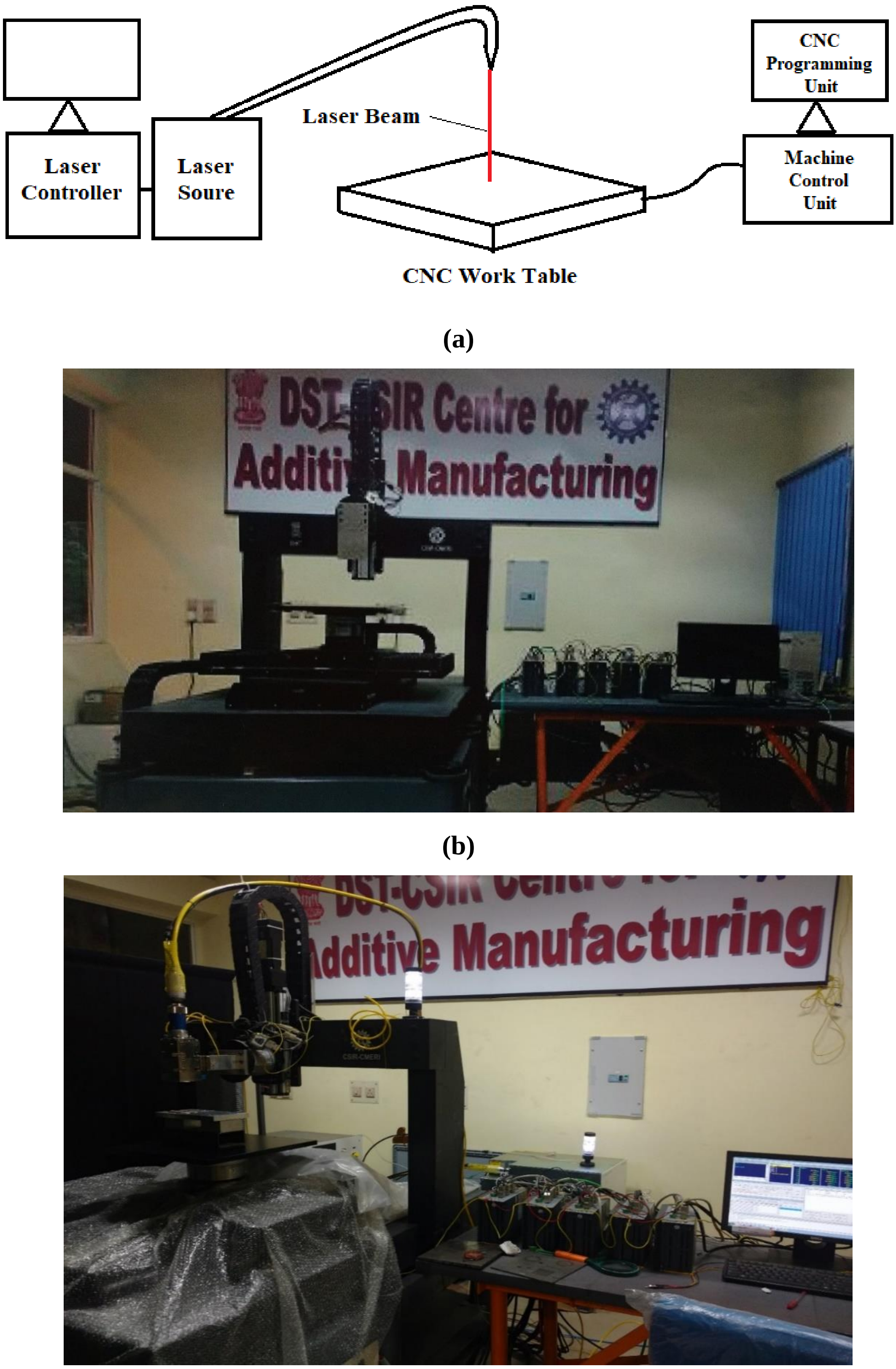
Laser Controller
Laser Soure
Laser Beam
CNC Programming Unit
Machine Control Unit
CNC Work Table
(a)
DST-CSIR Centre for Additive Manufacturing
(b)
DST-CSIR Centre for Additive Manufacturing
(c)

Fig. 4.1: (a) Schematic diagram of Continuous Wave Fibre Delivered Diode Laser Setup (b) and (c) Pictorial view of Continuous Wave Fibre Delivered Diode Laser Setup (Developed in CSIR-CMERI, Durgapur)

4.1.2 Continuous Wave Fibre Array Packages (FAP) Diode Laser Setup

This set up is the multi-purpose laser processing setup (shown in Fig. 4.2) has been developed at the lab of School of Laser Science and Engineering (SLSE), Jadavpur University, Kolkata. In this system continuous wave (CW) 30W Fibre Array Packages (FAP) diode laser system is synchronized with computer interface. Three-axes CNC work table is associated with this laser system. Motion system of CNC work table is controlled by computer interface.

Specification of Machine:

A) **Laser Source:**

1. Fibre Array Packages (FAP) diode laser
2. Power: 30W
3. Focusing Beam Diameter: 1011.5 µm

B) **CNC Stage:**

1. 400mm × 400mm
2. Velocity: 0 – 100 mm/s

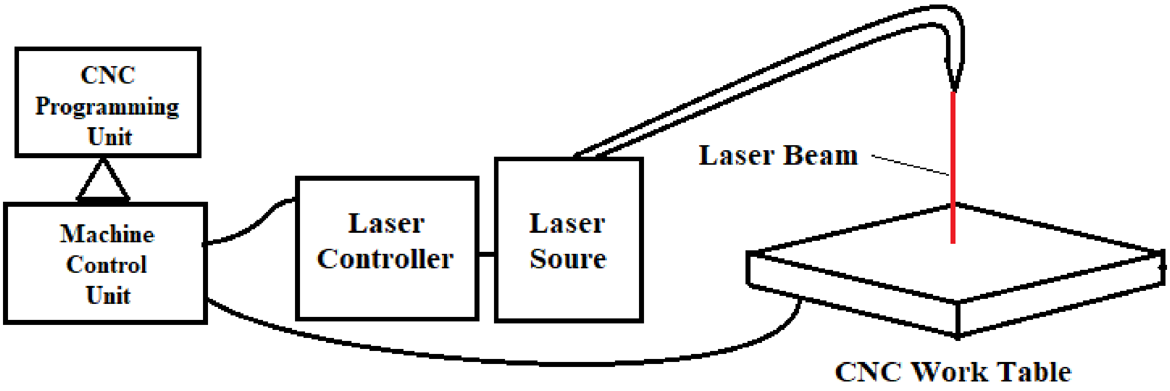
CNC Programming Unit
Machine Control Unit
Laser Controller
Laser Soure
Laser Beam
CNC Work Table

(a)

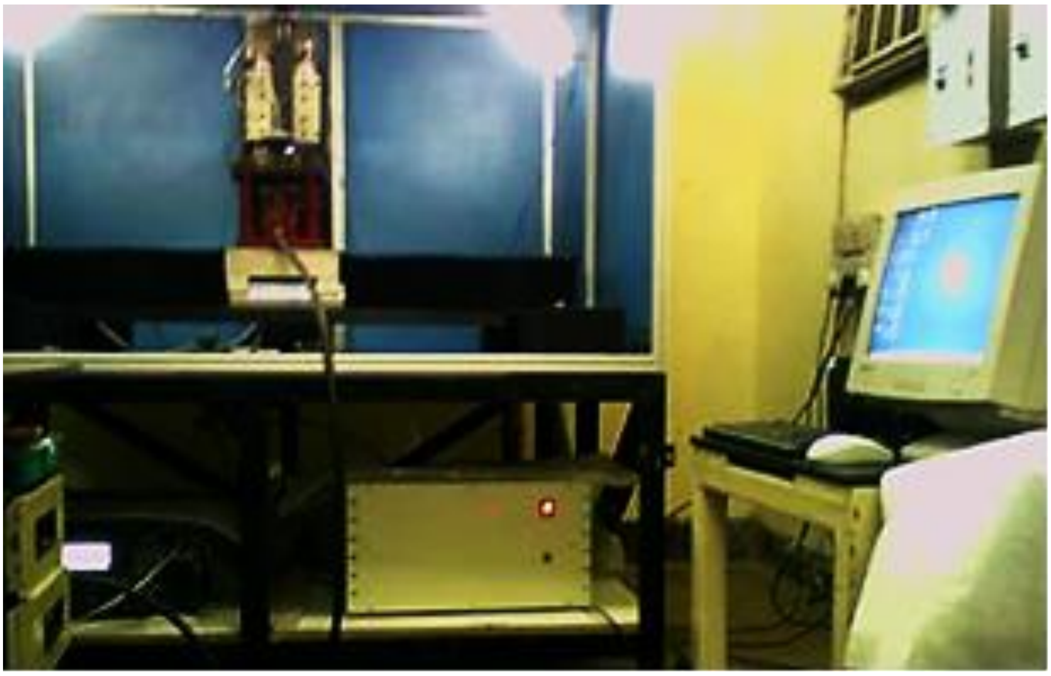

(b)

Fig. 4.2: (a) Pictorial view of Fibre Array Packages (FAP) Diode laser Set up (Developed at School of Laser Science and Engineering in Jadavpur University, Kolkata) (b) Schematic diagram of Fibre Array Packages (FAP) Diode laser Set up

4.2 Materials and Methods

During Practical Experiments of Selective Laser Sintering, micro-scale Copper powder is used. To overcome some difficulties during sintering micro-scale copper particles, Silicon Oil is used as binder material.

Table 4.1: Copper Powder

Material	Copper
Purity	99 %
Form	Powder
Resistivity	1.673μΩ-cm, 20 °C
Average grain size	5μm
Boiling point	2567°C (lit.)
Melting point	1083.4°C (lit.)
Density	8.94g/ml at 25 °C (lit.)

Table 4.2: Silicon oil as Binding Material

Binding Material	Silicon oil
Chemical Composition:	$[-\mathrm{Si}\ (\mathrm{CH_3})_2\mathrm{O}\ -]_n$
Grade:	For oil bath at more than 250ºC
Viscosity:	950 – 1050 cSt (at 25ºC)
Specific Gravity:	0.950 – 0.980 (at 25ºC)
Refractive index:	1.400 – 1.406 (at 25ºC)

Experimental Methods

Practical experiments of selective laser sintering of copper powder of average particle size of 5µm is performed by using two different Continuous Wave (CW) Lasers. In first case, sintering experiments are performed using Continuous Wave Fibre Delivered Diode Laser Setup and in the second case, the experiments are performed using Continuous Wave Fibre Array Packages (FAP) Diode Laser Setup.

4.2.1 Selective Laser Sintering using Continuous Wave (CW) Fibre Delivered Diode laser

In the first case, the experiments are performed in two phases. In the first phase, the dry copper powder has been sintered and in the second phase, copper powder with binder material is sintered by adopting selective laser sintering (SLS) methodology using Continuous Wave (CW) Fibre Delivered Diode laser at CSIR-CMERI, Durgapur. Experiments are performed using various laser intensity by varying laser power and scanning speed. Eleven number of parts are prepared using this experimental set up. Two samples are prepared by scanning dry copper powder and other nine samples are prepared by scanning copper powder blended with binder material.

A) Selective Laser Sintering of dry copper powder using CW Fibre Delivered Diode laser

Lumps of moist copper powder are kept in the temperature-controlled heating oven at 150ºC temperature for an hour to remove moisture from the copper powder. The almost dry copper powder is then coated over the Aluminium substrate with the help of soft buff. Dry copper powder layer is scanned under the Continuous Wave (CW) Fibre Delivered Diode Laser to develop sintered part of size 10mm×10mm×1.2mm. Two different part is developed by scanning 10 (ten) successive layers of dry 5µm sized copper powder are scanned using the different parameters as shown in Table 4.3. Hatch strategy is shown in Fig. 4.3. The microparts are found to be so much fragile that after removing from the substrate they are broken. Fig. 4.4 shows the pictorial view of micropart (S8).

During scanning with CW Fibre Delivered Diode Laser the copper powder particles are flying away the from the track of laser scan. Displacement of dry copper powder is similar to the case of displacement of particles in the case of scanning with pulsed Ng:YAG laser.

Table 4.3: Various laser parameters used for SLS of Dry Copper Powder using CW Fibre Delivered Diode Laser

Sample No.	Power (W)	Spot Dia (µm)	Scanning Speed (mm/s)	Hatch Space (µm)	No. of scan per layer
S8	14	480	12	400	5
S9	14	480	14	400	5

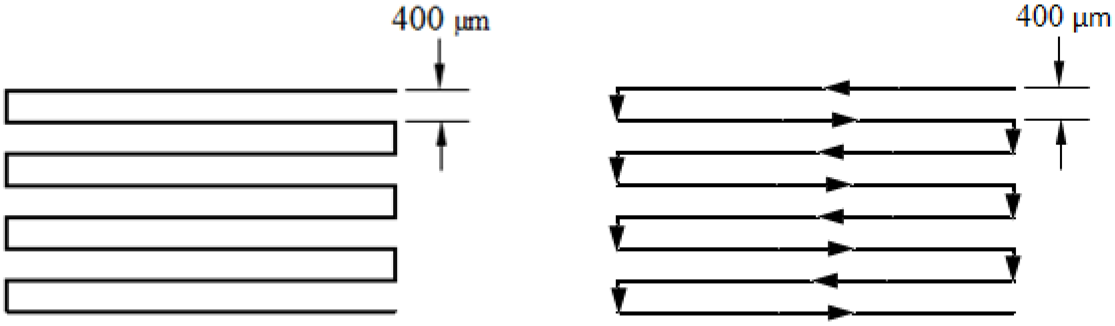

Fig. 4.3: Style of hatch and hatch space during Selective Laser Sintering of Micro-Scale Copper Powder Using Continuous Wave (CW) Fibre Delivered Diode Laser

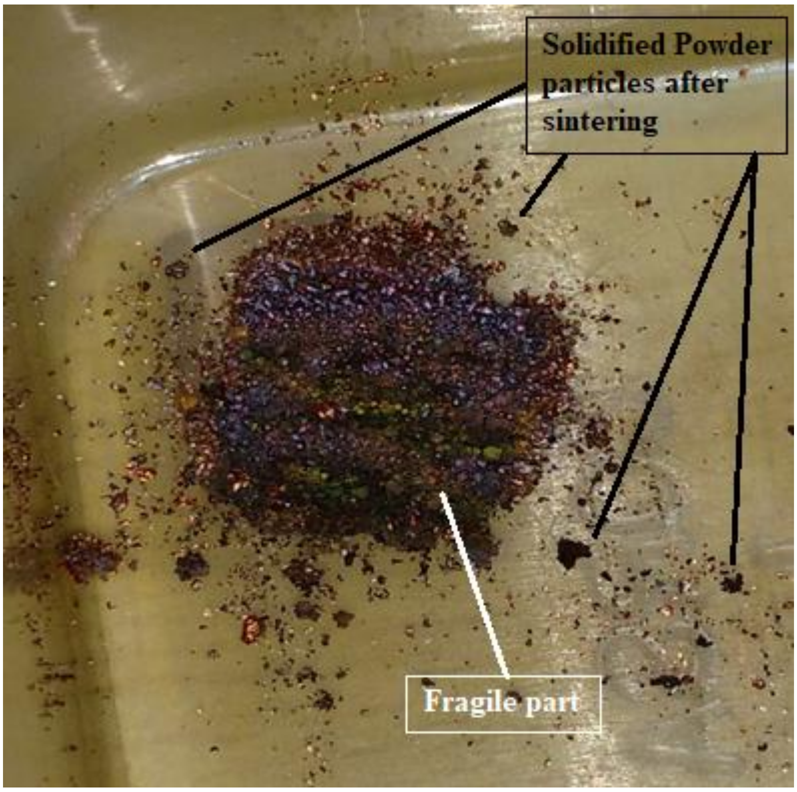

Fig. 4.4: Pictorial view of the micropart developed by selective laser sintering of dry copper powder of 5µm average particle size (Sample S8)

B) Selective Laser Sintering of copper powder blended with binder material using CW Fibre Delivered Diode laser

In the second phase, the copper powder of average grain size 5µm is blended with Silicon Oil at approximate weight ratio of 2:3 (Silicon oil : Copper Powder). The paste is coated consistently on the Aluminium substrate using sharp blade. The layer is scanned with CW Fibre Delivered Diode Laser. Nine number of part Samples are prepared of 10mm×10mm×1.2mm with a are developed by scanning 10 (ten) successive layers of Copper powder blended with Silicon Oil. During preparing part samples various parameters used during the selective laser sintering are shown in Table 4.4. Each layers of every sample are scanned with hatch style and hatch space as shown in Fig. 4.3. The pictorial views of parts of size 10mm×10mm×1.2mm are shown in Fig. 4.5. After sintering of 10 successive layers the sintered part is separated from the Aluminium substrate. Then the laser sintered part is placed inside the heating oven, and then cured slowly at 350ºC at controlled rate for several hours to remove residue of silicon oil.

Table 4.4: Various laser parameters for SLS of Copper Powder with Silicon Oil using CW Fibre Delivered Diode laser

Sample No.	Power (W)	Spot Dia (µm)	Scanning Speed (mm/s)	Hatch Space (µm)	No. of scan per layer
S1	20	480	16	400	5
S2	20	480	20	400	5
S3	20	480	24	400	5
S4	14	480	12	400	5
S5	14	480	14	400	5
S6	11	480	12	400	5
S7	11	480	14	400	5
S10	11	480	16	400	10
S11	11	480	16	400	10

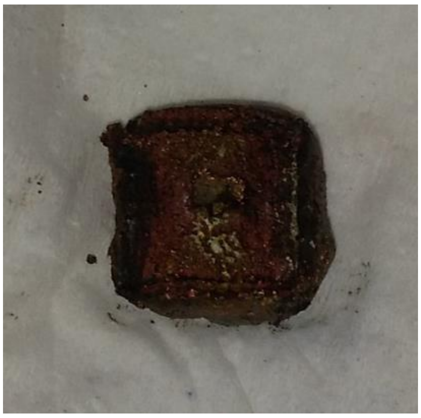
(a) Sample S1

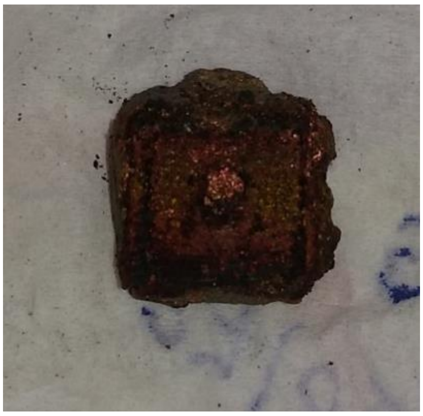
(b) Sample S2

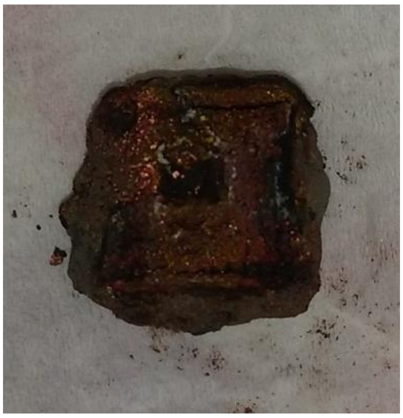
(c) Sample S3

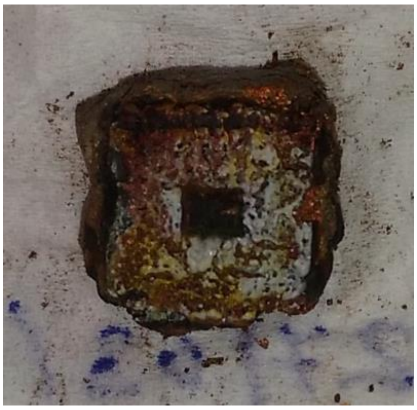
(d) Sample S4

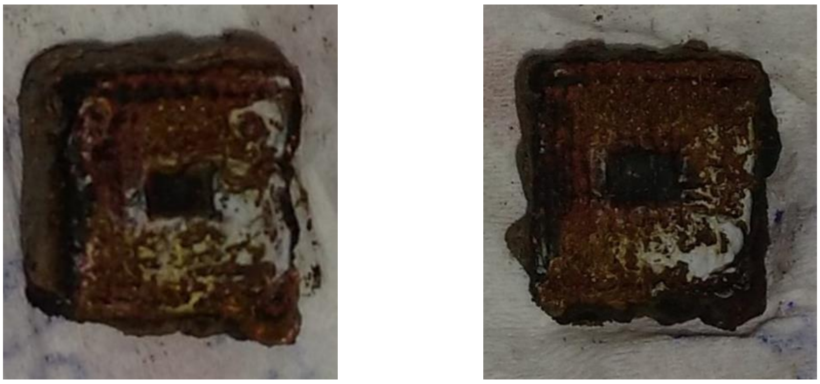

(e) Sample S5 (f) Sample S6

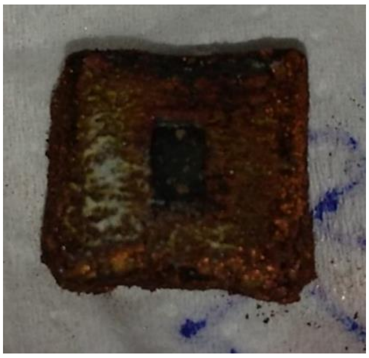

(g) Sample S7

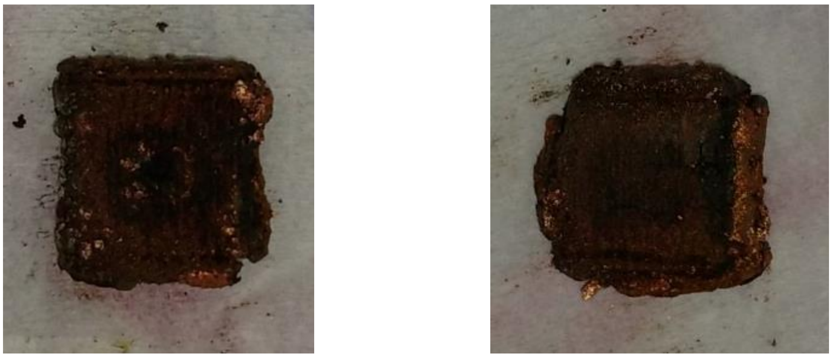

(h) Sample S10 (i) Sample S11

Fig. 4.5: Pictorial view of the part developed by selective laser sintering of copper powder with Silicon Oil Binder

4.2.2 Selective Laser Sintering of copper powder blended with binder material using Continuous Wave (CW) Fibre Array Packages (FAP) Diode Laser

In the second case, mixture of Copper powder of average particle size 5µm and silicon oil binder material is scanned under Continuous Wave (CW) Fibre Array Packages (FAP) Diode Laser. As discussed earlier, the coating of 5µm Cu powder is quite difficult due to formation of lumps of powder with moisture, powder is preheated for approximately 60 minutes in the temperature-controlled heating oven at 150ºC. The near dry copper powder is blended with binder material viz. Silicon Oil and coated on glass slide almost consistently with the help a sharp blade so as to obtain a flat powder surface. Initially, a glass slide is used as substrate material. But due to high intensity of CW laser, glass substrate is cracked. To overcome this difficulty Aluminium substrate is used as substrate material. Copper Powder is blended with Silicon Oil at approximate weight ratio of 2:3 (Silicon oil : Copper Powder). The layer of copper powder is scanned by Continuous Wave (CW) FAP Diode Laser. This procedure is repeated by adding and scanning the powder material layer-layer-layer with an average layer thickness of 200µm. Six parts of size 10mm×10mm×2mm has been developed by scanning 10 successive layers of copper powder using CW FAP Diode Laser at different scanning speeds. For six samples the various laser parameters used are shown in the Table 4.5. Fig. 4.6 is showing the strategy of hatch and hatch space used during laser scan. Fig. 4.7 is showing the six parts developed by using laser sintering. After sintering, the sintered parts are separated from the Aluminium substrate and observed under scanning electron microscope. The SEM micrographs of the sintered parts are shown in the Fig. 4.10. In the sintered parts presence of residual of silicon oil is not remarkable.

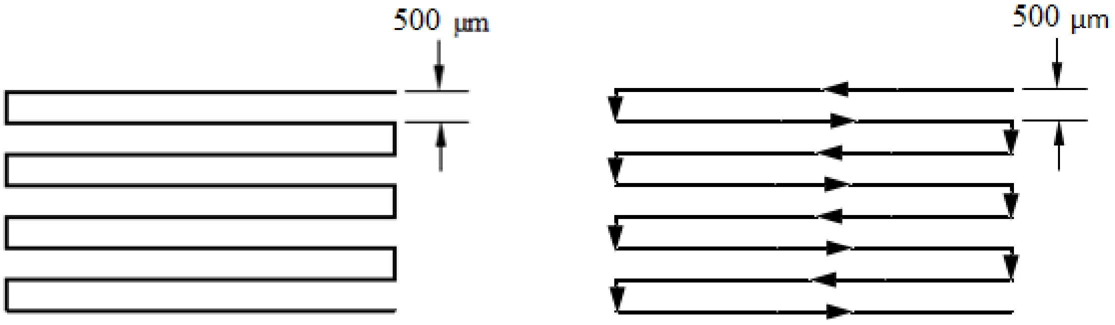

Fig. 4.6: Type of hatch and hatch space during Selective Laser Sintering of Micro-Scale Copper Powder Using Continuous Wave (CW) FAP Diode Laser

Table 4.5: Various laser parameters used for SLS of Copper Powder with Silicon Oil binder material in CW FAP diode laser

Sample no.	Total no. of layers	Power (W)	Scanning speed (mm/min)	Spot diameter (µm)	Hatch spacing (µm)	Total no. of scans per layer
J-1	10	13	500	1011.5	500	5
J-2	10	10	500	1011.5	500	5
J-3	10	10	800	1011.5	500	5
J-4	10	12.0	180	1011.5	500	5
J-5	10	13.65	180	1011.5	500	5
J-6	10	15.2	180	1011.5	500	5

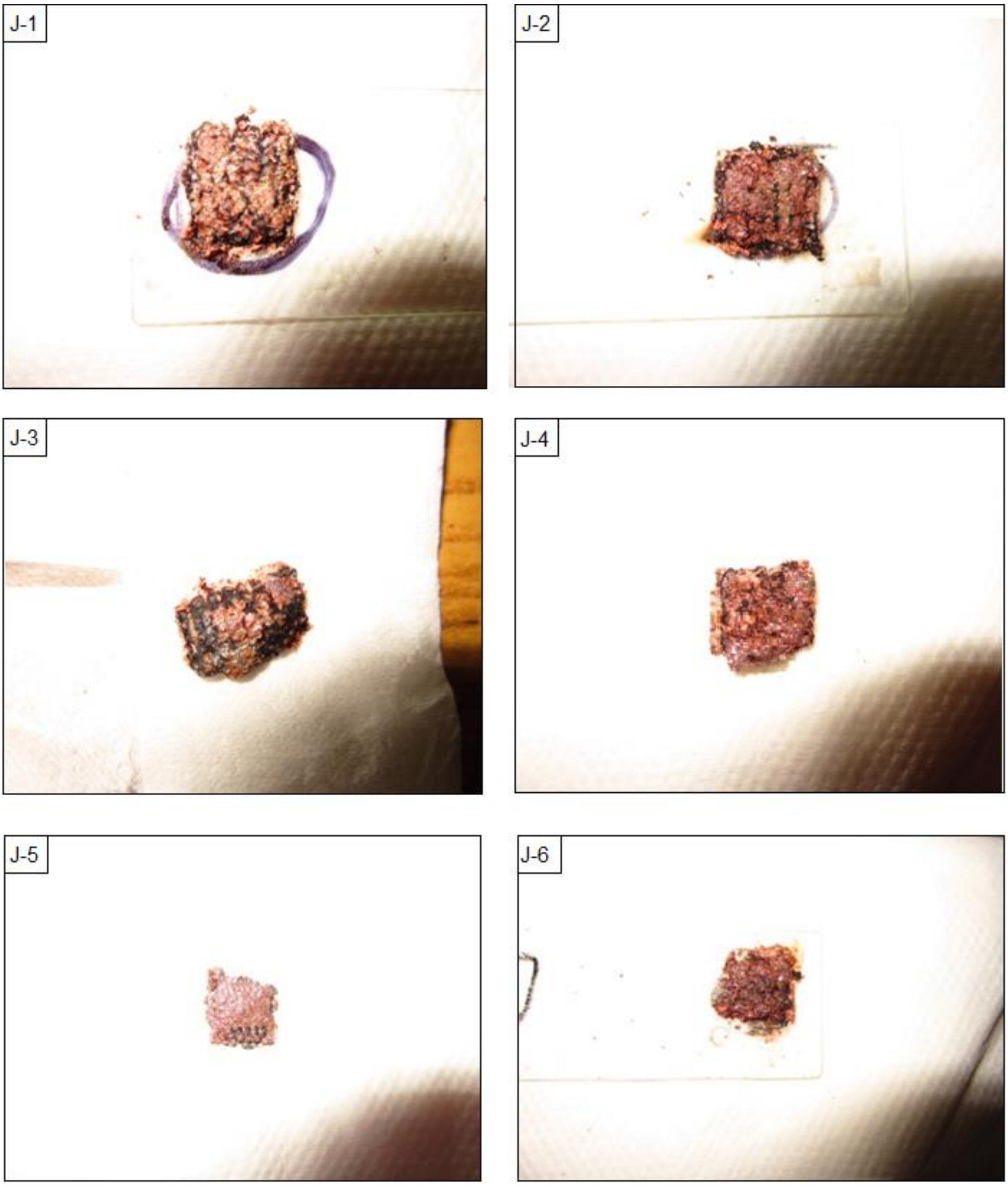

Fig. 4.7: Pictorial view of samples of selective laser sintered copper powder of 5µm average particle size blended with silicon oil (scanned under FAP CW Diode laser)

4.3 Results and Discussions

As experiments are conducted using different experimental sets up, results are discussed separately for two different cases.

4.3.1 Selective Laser Sintering using Continuous Wave (CW) Fibre Delivered Diode laser

a) Observations

In the first phase, dry Copper powder layers are scanned using Continuous Wave Fibre Delivered Diode Laser to develop two microparts. Various parameters, which are used for preparing Sample Nos. S8 and S9 the are shown in the Table 4.3. Only scanning speed is changed during sintering Dry Copper powder. Throughout the process of sintering dry copper powder layer, the phenomenon of flying out of dry copper powder from the track of laser scan has been observed. This phenomenon is similar to the laser scan using pulsed laser. Balling effect is also visible. Thicker layer of dry powder is created as laser power used in this case is very high. Due to higher thickness of powder layer, displacement of particles is quite low. Initially, the layers are looking dense and compact but with a lot of porous area. After completion of scanning 10 layers of dry powder it is observed that the micropart is very much fragile and it collapsed completely when microparts are separated from the substrate. It is clear from Fig. 4.4 that some solid lumps are present. These solid lumps are further investigated under SEM. The views of SEM in Fig. 4.8 reveal that neck formation properly occurred during dry sintering process.

Later Silicon Oil is blended with Copper powder and the layers are scanned using Continuous Wave Fibre Delivered Diode Laser to develop nine sintered parts. Table 4.4 is showing various laser parameters used during scanning. Fig. 4.5 is showing the pictorial views of developed sintered parts. Sintered parts are developed on aluminium substrates. The sintered parts are heated in a heating oven for several hours the samples around 250ºC to 300ºC temperature to remove the residue of Silicon oil from the developed part. After post processing the sintered parts are separated from the substrates and found quite stronger parts. These sintered parts are investigated under SEM. It is observed that silicon oil residuals are completely removed from the sintered part. Fig. 4.9 is showing SEM micrographs of the samples. SEM images of sintered parts show promising results of neck formation and porosity formation.

From the Table 4.4 it is observed that, during preparation of Sample No. S1, S2 and S3, successive layers are scanned with laser power of 20W with scanning speed of 16mm/s, 20mm/s and 24mm/s respectively. During preparation of Sample No. S4 and S5, successive layers are scanned with laser power of 14W with scanning speed of 12mm/s and 14mm/s respectively. During preparation of Sample No. S6, S7 and (S10 & S11) successive layers are scanned with laser power of 11W with scanning speed of 12mm/s, 14mm/s and 16mm/s respectively.

b) Characterization sintered parts

The sintered parts produced by scanning of dry copper powder and by scanning a mixture of dry powder and silicon oil are studied under scanning electron microscope. The SEM images of dry sintered parts and sintered part with silicon oil are shown in Fig. 4.8 and 4.9 respectively. Though the neck formation is visible in the dry sintered part, due to shrinkage and balling phenomenon the bonding become weak. Due to this reason dry sintered part collapsed during separation from the substrate. Due to the shrinkage of molten material porosity level become very high. Whereas, the sintered part using binder material is quite strong and porosity level become low. During cooling of the molten material, the viscous effects of binder material resist shrinkage of the material. Due to this reason porosity in the sintered part become low.

i) Neck growth during dry sintering is clearly visible in the SEM micrograph in the Fig. 4.8. Neck growth during sintering with binder material is quite better than the part of dry sintering. SEM images in Fig. 4.9 reveal that neck growth is uniform in all the cases. Due to change in laser power and scanning speed the laser energy density is varied. Due to high intensity of laser the surface become rough. Linking of the adjacent particles and successive layers is visible from the SEM micrographs.

ii) Though the bonding between adjacent particles and successive layers are visible from SEM micrographs (Fig. 4.9). Still porosity is observed in the SEM micrographs of all the samples. Samples prepared with higher power and low scanning speed of laser beam showed better result of dense structure. In these cases, porosity level is lower than the samples prepared by lower power and hinger scanning speed.

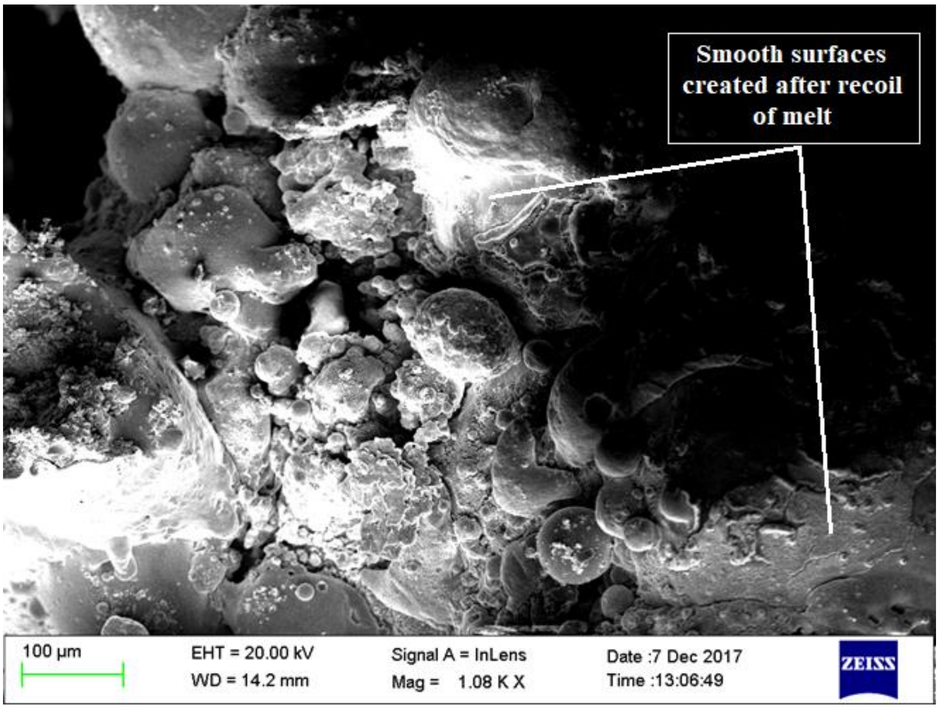
Smooth surfaces created after recoil of melt
100 µm
EHT = 20.00 kV
WD = 14.2 mm
Signal A = InLens
Mag = 1.08 K X
Date :7 Dec 2017
Time :13:06:49
ZEISS

(a) Sample S8

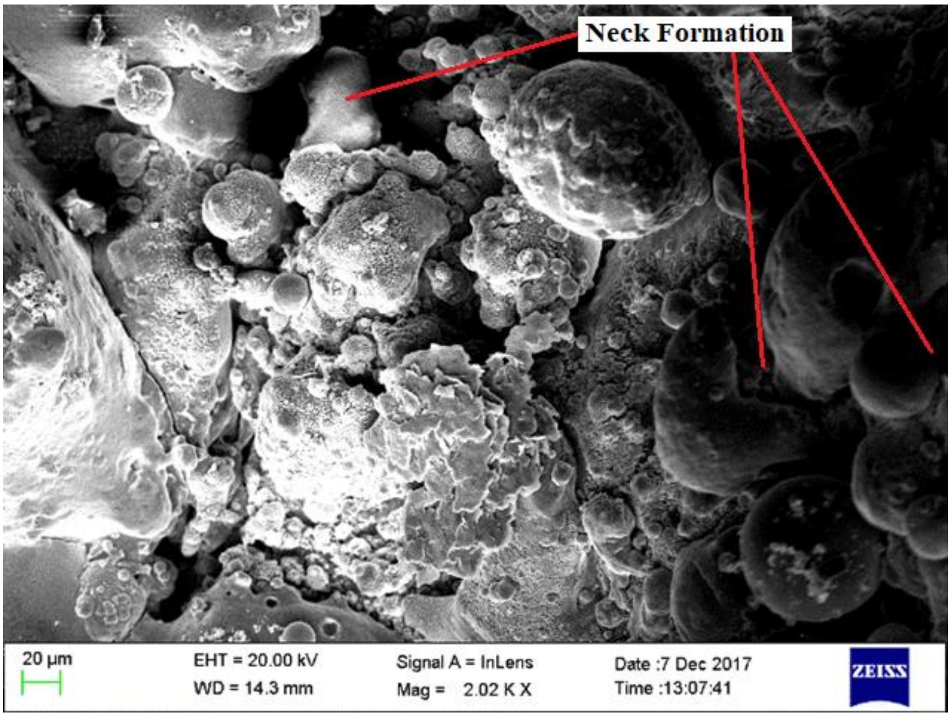
Neck Formation
20 µm
EHT = 20.00 kV
WD = 14.3 mm
Signal A = InLens
Mag = 2.02 K X
Date :7 Dec 2017
Time :13:07:41
ZEISS

(b) Sample S8

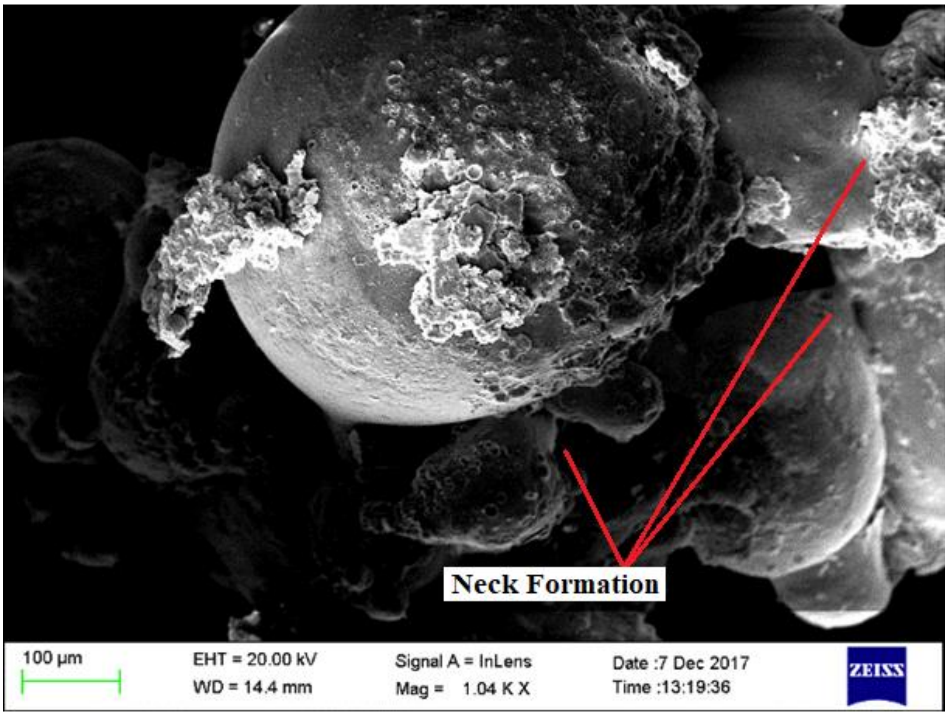
Neck Formation
100 µm
EHT = 20.00 kV
WD = 14.4 mm
Signal A = InLens
Mag = 1.04 K X
Date :7 Dec 2017
Time :13:19:36
ZEISS

(c) Sample S9

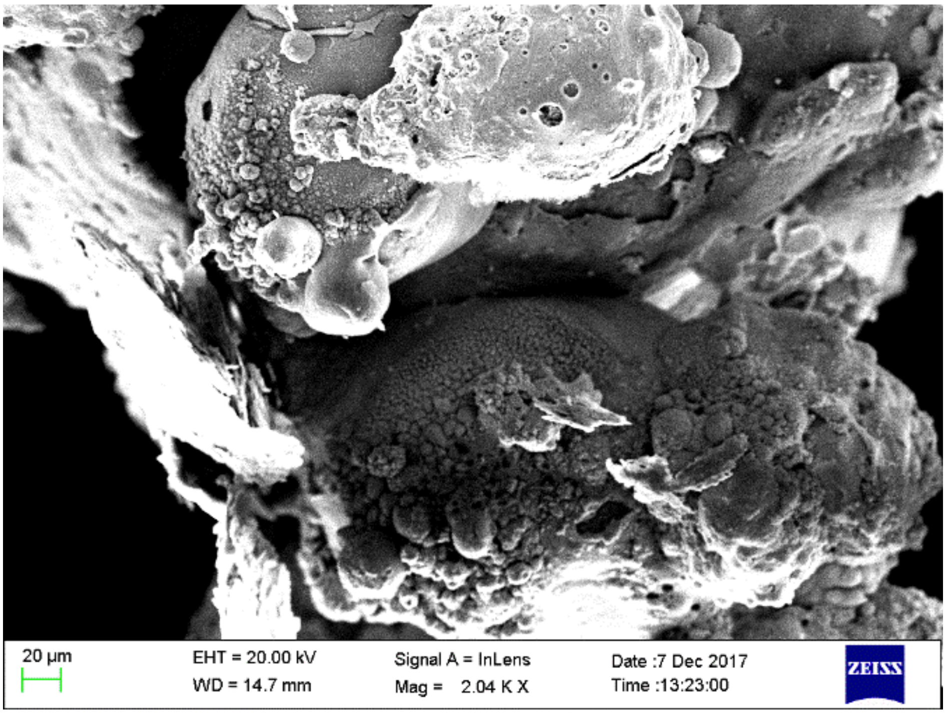
20 µm
EHT = 20.00 kV
WD = 14.7 mm
Signal A = InLens
Mag = 2.04 K X
Date :7 Dec 2017
Time :13:23:00
ZEISS

(d) Sample S9

Fig. 4.8: SEM Micrographs of selective laser sintered dry copper powder of 5µm average particle size (scanned under CW Fibre Delivered Diode laser)

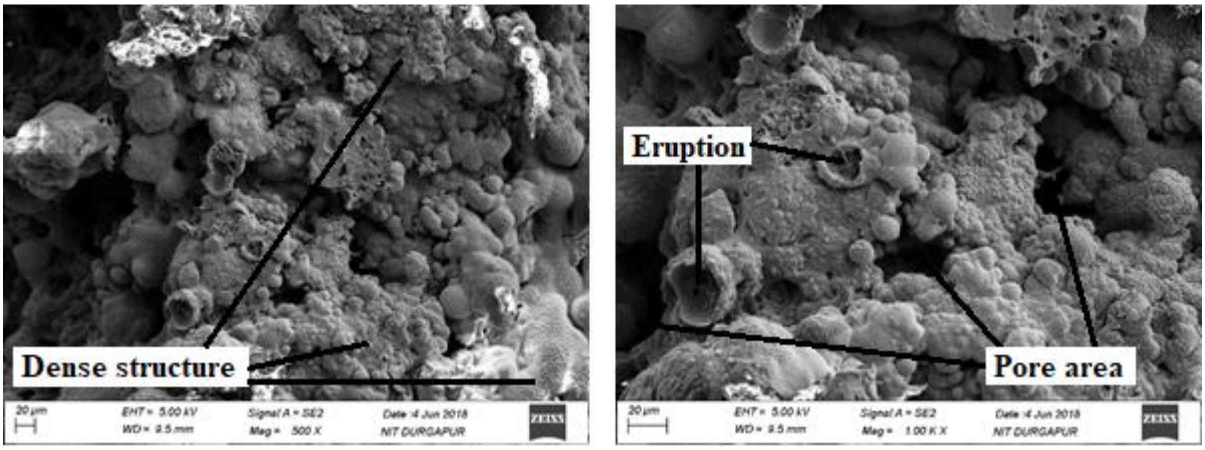
Dense structure
20 µm
EHT = 5.00 kV
WD = 9.5 mm
Signal A = SE2
Mag = 500 X
Date :4 Jun 2018
NIT DURGAPUR
ZEISS
Eruption
Pore area
20 µm
EHT = 5.00 kV
WD = 9.5 mm
Signal A = SE2
Mag = 1.00 K X
Date :4 Jun 2018
NIT DURGAPUR
ZEISS

(a) Sample S1 (b) Sample S1

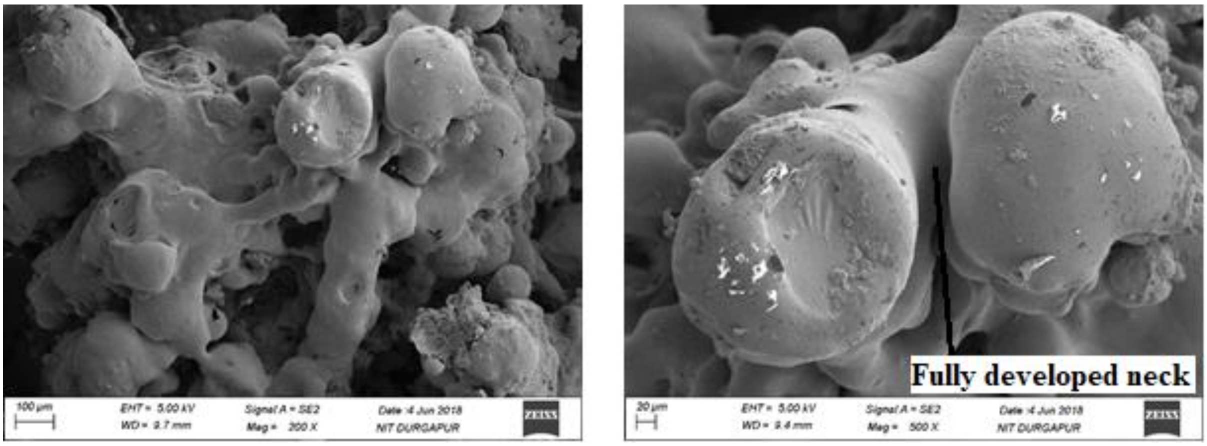
100 µm
EHT = 5.00 kV
WD = 9.7 mm
Signal A = SE2
Mag = 200 X
Date :4 Jun 2018
NIT DURGAPUR
ZEISS
Fully developed neck
20 µm
EHT = 5.00 kV
WD = 9.4 mm
Signal A = SE2
Mag = 500 X
Date :4 Jun 2018
NIT DURGAPUR
ZEISS

(c) Sample S2 (d) Sample S2

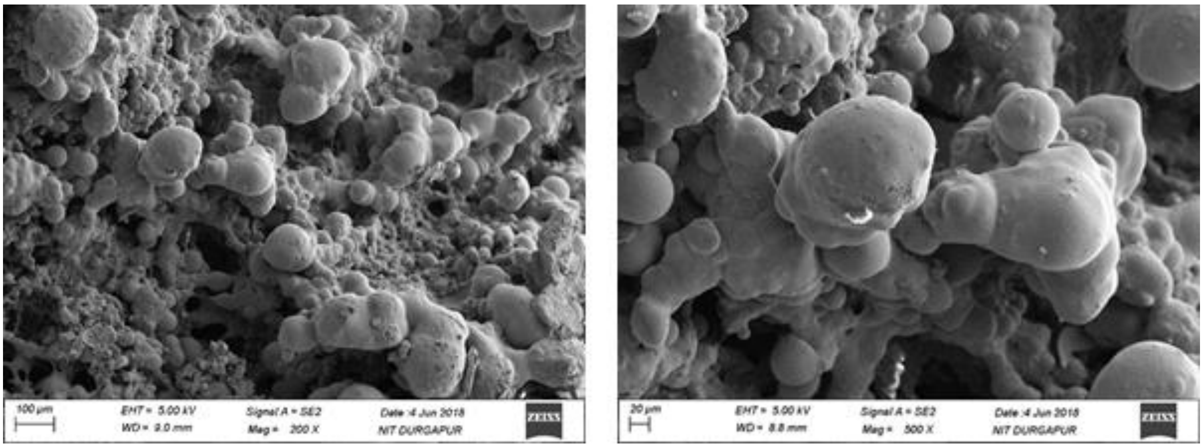
100 µm
EHT = 5.00 kV
WD = 9.0 mm
Signal A = SE2
Mag = 200 X
Date :4 Jun 2018
NIT DURGAPUR
ZEISS
20 µm
EHT = 5.00 kV
WD = 8.8 mm
Signal A = SE2
Mag = 500 X
Date :4 Jun 2018
NIT DURGAPUR
ZEISS

(e) Sample S3 (f) Sample S3

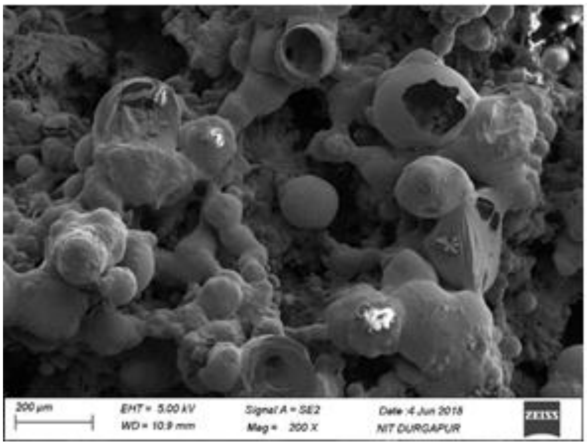
200 µm
EHT = 5.00 kV
WD = 10.9 mm
Signal A = SE2
Mag = 200 X
Date :4 Jun 2018
NIT DURGAPUR

(g) Sample S4

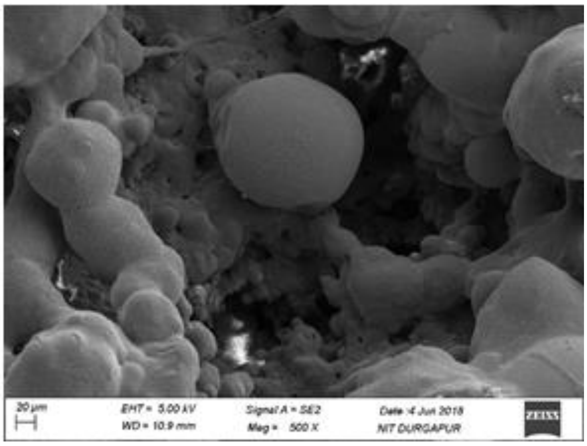
20 µm
EHT = 5.00 kV
WD = 10.9 mm
Signal A = SE2
Mag = 500 X
Date :4 Jun 2018
NIT DURGAPUR

(h) Sample S4

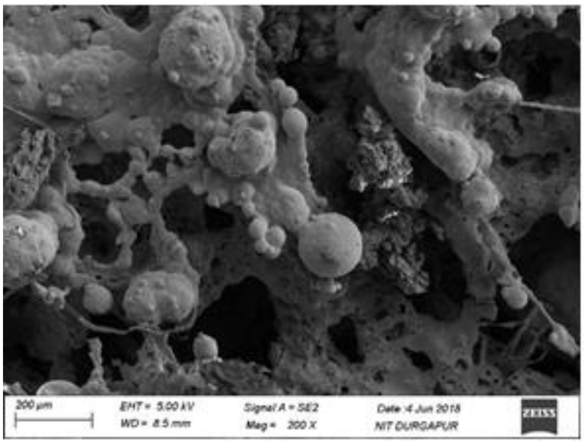
200 µm
EHT = 5.00 kV
WD = 8.5 mm
Signal A = SE2
Mag = 200 X
Date :4 Jun 2018
NIT DURGAPUR

(i) Sample S5

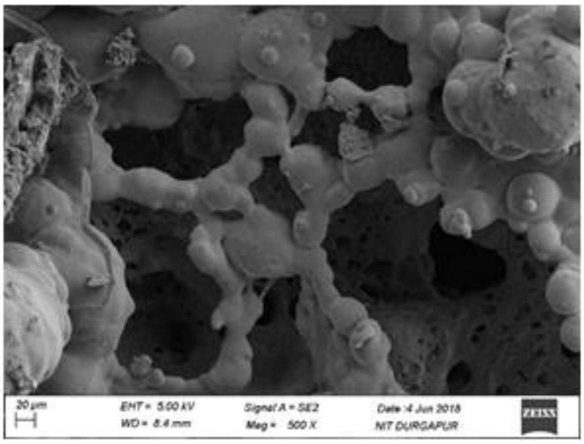
20 µm
EHT = 5.00 kV
WD = 8.4 mm
Signal A = SE2
Mag = 500 X
Date :4 Jun 2018
NIT DURGAPUR

(j) Sample S5

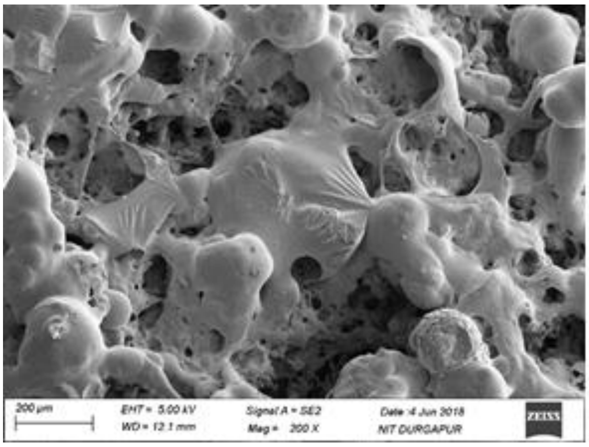
200 µm
EHT = 5.00 kV
WD = 12.1 mm
Signal A = SE2
Mag = 200 X
Date :4 Jun 2018
NIT DURGAPUR

(k) Sample S6

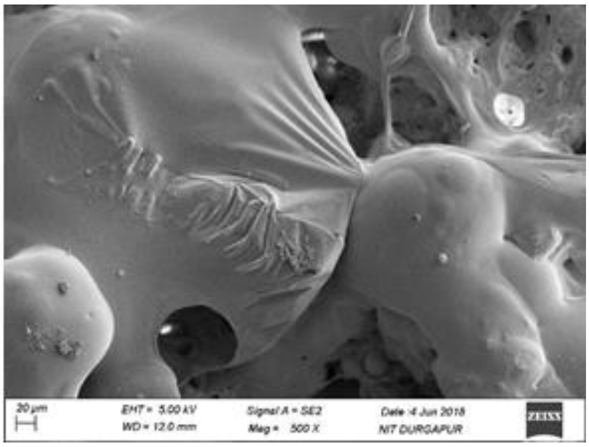
20 µm
EHT = 5.00 kV
WD = 12.0 mm
Signal A = SE2
Mag = 500 X
Date :4 Jun 2018
NIT DURGAPUR

(l) Sample S6

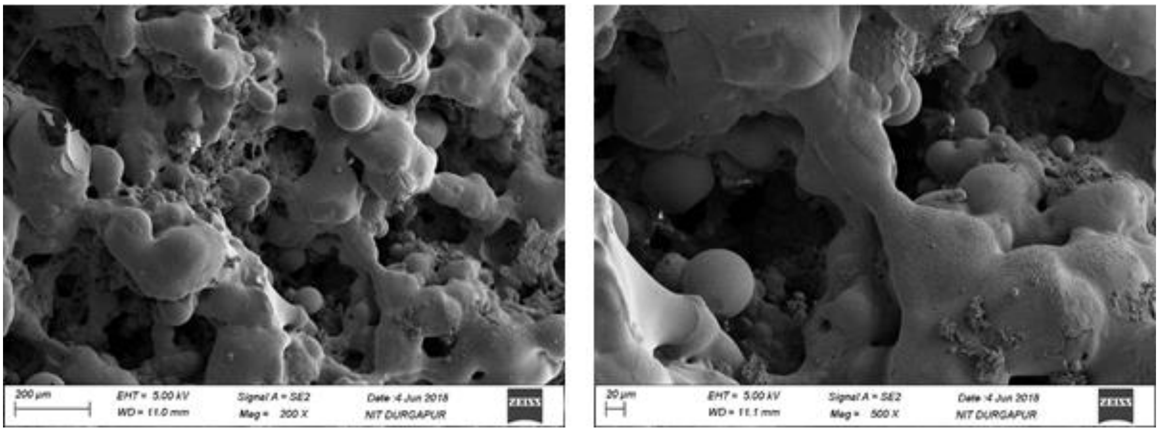

(m) Sample S7

(n) Sample S7

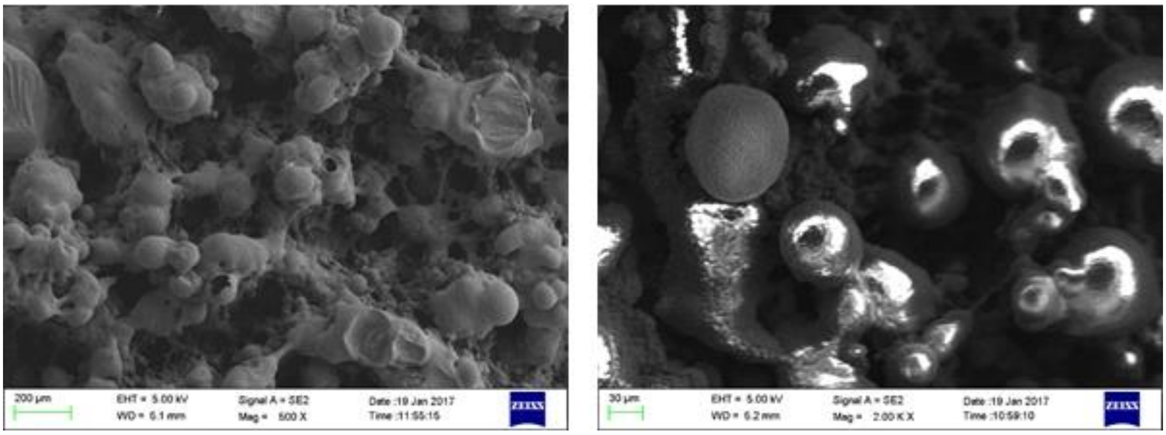

(p) Sample S10

(q) Sample S10

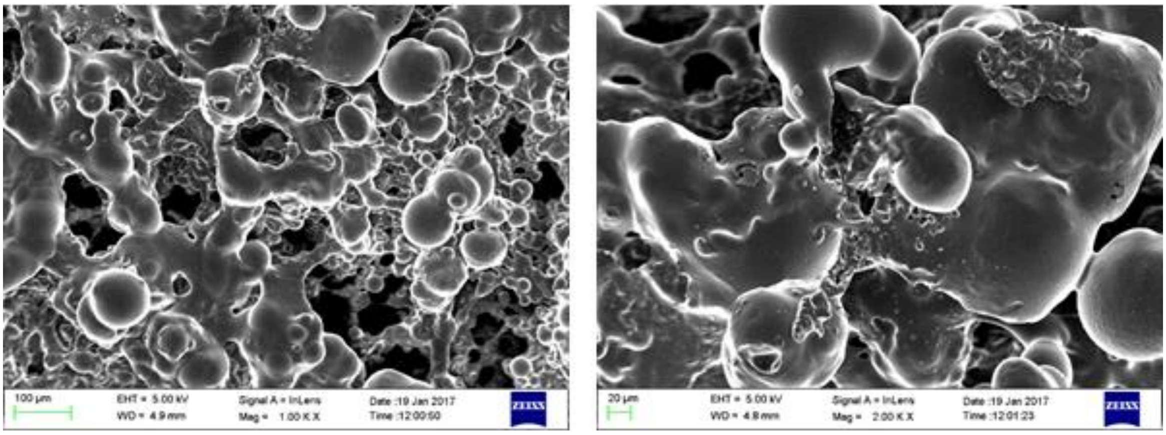

(r) Sample S11

(s) Sample S11

Fig. 4.9: SEM Micrographs of selective laser sintered copper powder of 5µm average particle size blended with silicon oil (different laser parameters shown in Table 4.4)

c) Effect of process parameters on neck formation and porosity

Dry copper powder is sintered in different laser power as shown in Table 4.3. During sintering of dry copper powder, laser power is not changed but scanning speed is changed. SEM micrograph reveals that, sample S8 has more dense structure than S9. Due to low scanning speed, laser power density is more in case of Sample S8.

Table 4.4 shows the different process parameters of laser scanning during scanning of mixture of copper powder and silicon oil. The SEM micrographs of two component sintering show more dense structure than the dry sintered samples. Difference is also observed in the cases of two component sintering using different parameters. In Table 4.4 it is observed that samples are prepared in three different laser powers – 20W, 14W and 11W. Using 20W laser power three samples are prepared with scan speed of 16mm/s, 20mm/s and 24mm/s. Using 14W laser power two samples are prepared with scan speed of 12mm/s and 14mm/s. Using 11W laser power two samples are prepared with scan speed of 12mm/s, 14mm/s and 16mm/s.

i) *The effect of scanning speed on porosity level is explained as below:*
From the SEM micrographs of samples S1, S2 and S3 (Fig. 4.9(a and b), 4.9(c and d), 4.9(e and f)), it is observed that, porosity level of the sample S1 is low among them. Laser power for the samples S1, S2 and S3 are same but S1 is prepared with lowest scanning speed among them. This reveals that laser energy density used for preparing sample S1 is more among all the three samples and this shows lower level of porosity among them. Laser power of S4 and S5 is same i.e. 14W but S4 is prepared with lower scanning speed i.e. 12mm/s and of S6, S7 and (S10 & S11) is same i.e. 11W but S6 is prepared with lower scanning speed i.e. 12mm/s. From the micrographs it is observed that, porosity level of Sample S6 is lower than the samples S4, S5, S7, S10 and S11. SEM micrographs of samples S4, S5, S6, S7, S10 and S11 are shown in Fig. 4.9(g and h), 4.9(i and j), 4.9(k and l), 4.9(m and n), 4.9(p and q) and 4.9(r and s) respectively.

ii) *The effect of laser power on porosity level is explained as below:*
Sample S4 and S6 are prepared using same scanning speed of 12mm/s but with different laser power of 14W and 11W respectively. Sample S5 and S7 are prepared using same scanning speed of 14mm/s but with different laser power of 14W and

11W respectively. Sample S1 and (S10&S11) are prepared using same scanning speed of 16mm/s but with different laser power of 20W and 11W respectively. SEM images of Sample S4, S5 and S1 show the lower porosity. These three samples are prepared with higher laser power in that set. Higher laser power of same scanning speed, porosity level become lower.

4.3.2 Selective Laser Sintering of copper powder blended with binder material using Continuous Wave (CW) Fibre Array Packages (FAP) Diode Laser

a) Observations

In these sets of experiments, copper powder of average grain size 5µm is scanned selectively using Continuous Wave (CW) FAP Diode Laser. The layers of copper powder blended with silicon oil is scanned. After development of the parts, residual of Silicon oil is found very less in the sintered parts. Due to high intensity of laser silicon oil is vaporized. Due to very low scanning speed the intensity of laser in increased and the part is heated. The SEM micrographs for three samples (J-1, J-2, and J-3) shown in Fig. 4.10(a, b and c) have indicated neck formation and bonding between adjacent particles and adjacent layers. Dense structure of sintered copper particles is also visible with very low porosity. However, due to high intensity of laser with higher scanning speed rough surface is observed. The SEM images of Sample J-4, J-5 and J-6 (Fig. 4.10(d, e and f)) reveals full melting of the particles with large pores on the surface.

b) Characterization sintered parts

Fig. 4.7 depicts the pictorial views of six selectively laser sintered parts in which is prepared by scanning copper powder blended with silicon oil using CW FAP Diode Laser. SEM images are taken for further analysis the parts. Fig. 4.10 shows the SEM views of the six samples. The SEM images of the samples J-1, J-2 and J-3 reveal that sintering is performed quite well. And the from the SEM images of sample J-4, J-5 and J-6 it is observed that, particles are totally melted rather than getting defused. Due to full melting of the particles of the top surface become smoother. Due to rapid melting, condensation and solidification of molten materials some pores are created.

i) Neck growth and bonding between adjacent particles and layers shows good result in the SEM micrographs (Fig. 4.10(a, b and c)) of sample J-1, J-2 and J-3. Upper surface of the part become rough. From the SEM images of sample J-4, J-5 and J-6 (Fig. 4.10(d, e and f)) neck growth is not visible properly. In the later case, due to high intensity of laser the copper particles are melted fully and then solidified.

ii) Porosity level in the samples J-1, J-2 and J-3 is very low. Whereas, lot of pores are visible on the top surface of the samples J-4, J-5 and J-6. Due to low scanning speed the energy density of laser irradiation is quite high. High energy density leads the particles to full melting. Due to rapid melting and solidification shrinkage in material take place and large pores are created.

c) Effect of process parameters on structure of sintered part

The samples are prepared in various process conditions e.g. scan speed, hatch spacing and laser power. For the samples J-4, J-5 and J-6 laser scanning speed are same i.e. 180mm/min or 3mm/s. The scanning speed is very low, due to this reason melting takes place. The samples S1 and S2 are prepared by scanning with scan speed of 500mm/min or 8.33mm/s and laser power 13W and 10W respectively. Sample J-3 is prepared with laser scan of scanning speed of 800mm/min or 13.33mm/s with laser power of 10W. Due to low scanning speed the intensity of laser is increased. This results dense structure of sintered part.

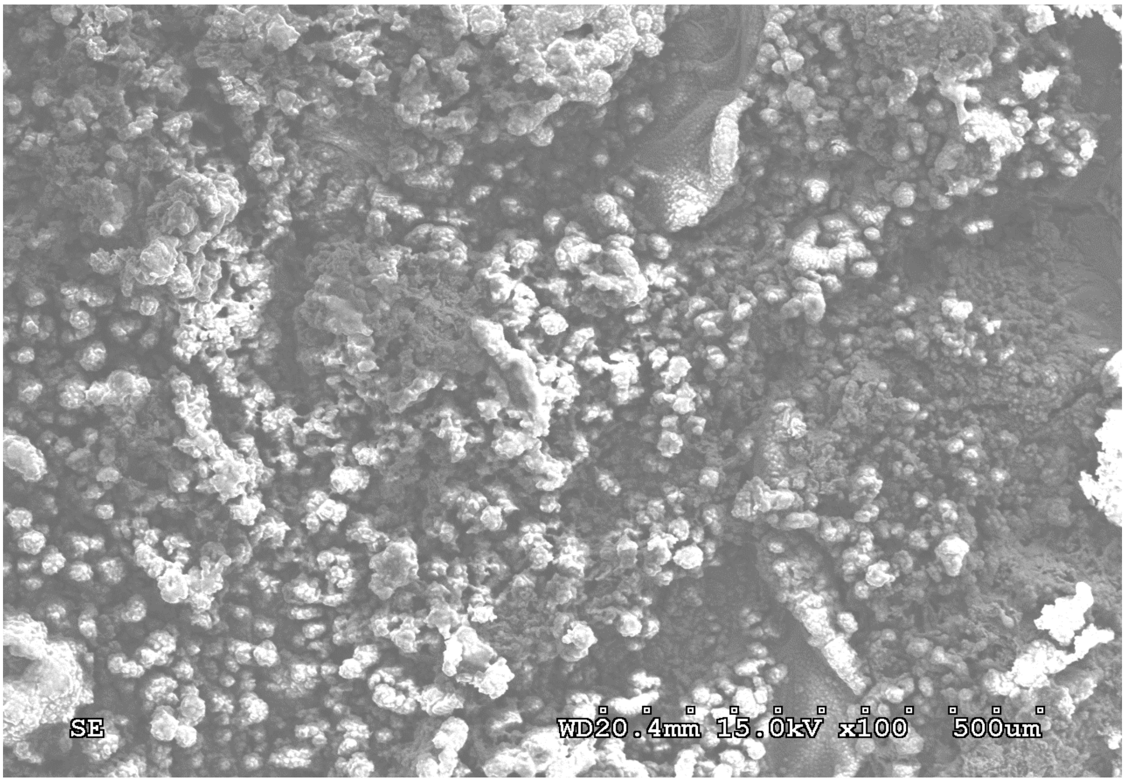
SE
WD20.4mm 15.0kV x100 500um

(a) Sample No. – J-1

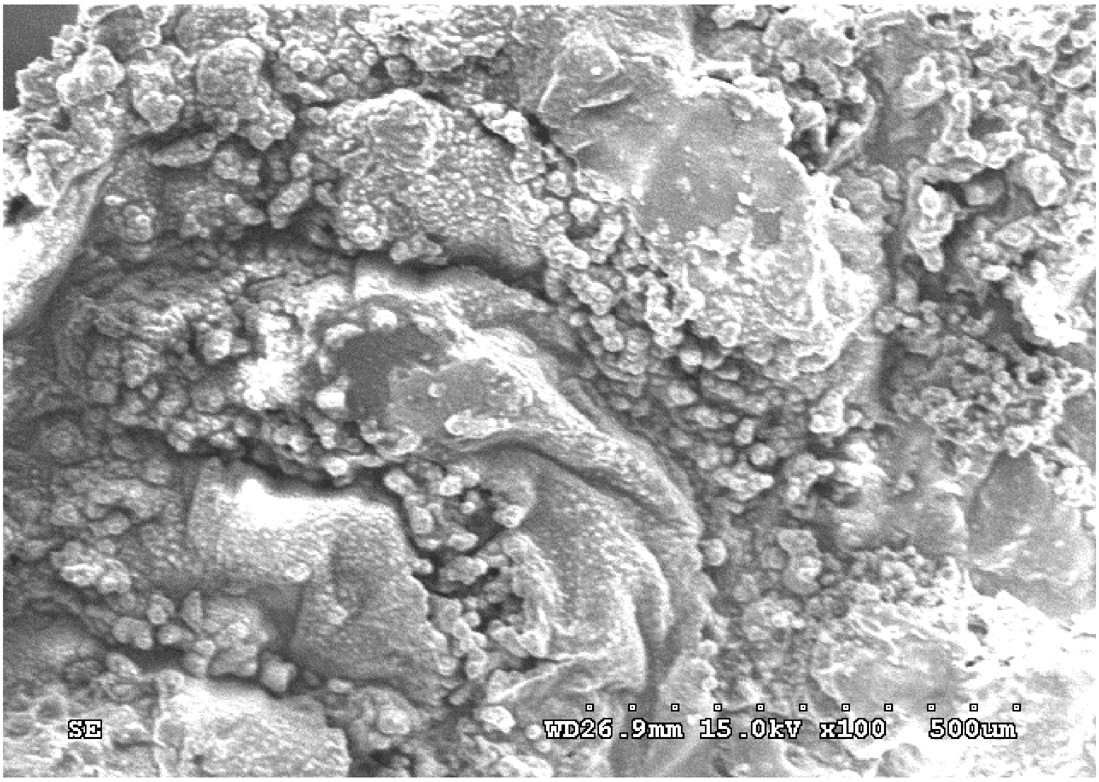
SE
WD26.9mm 15.0kV x100 500um

(b) Sample No. – J-2

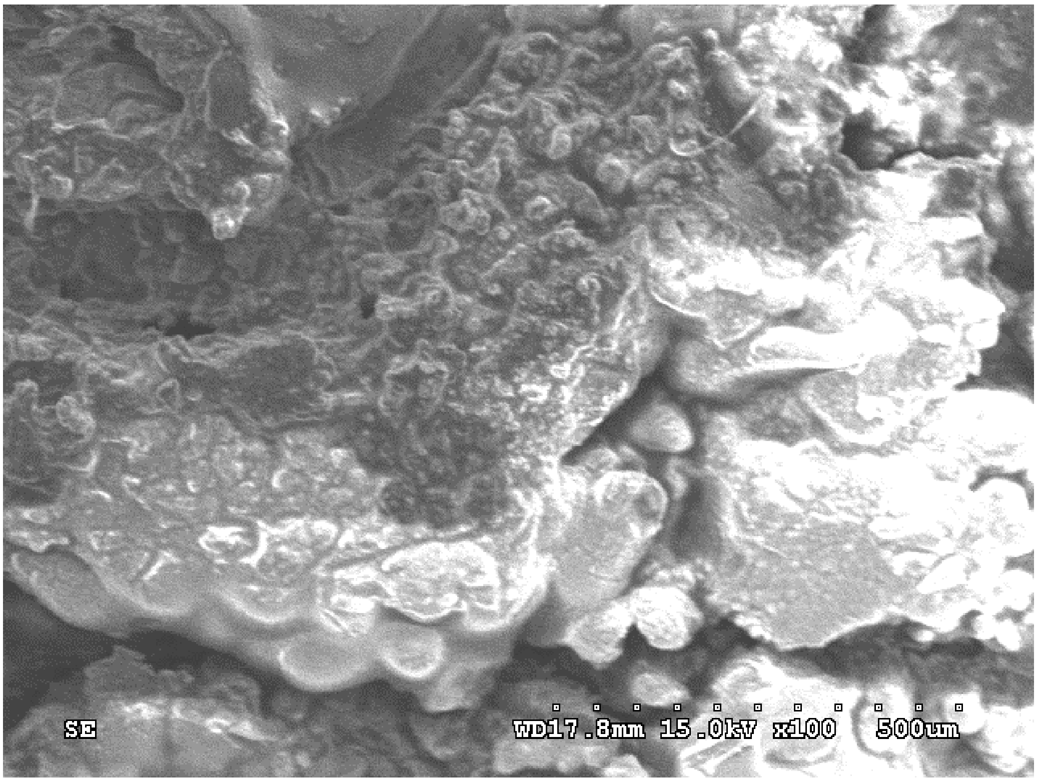
SE
WD17.8mm 15.0kV x100 500um

(c) Sample No. – J-3

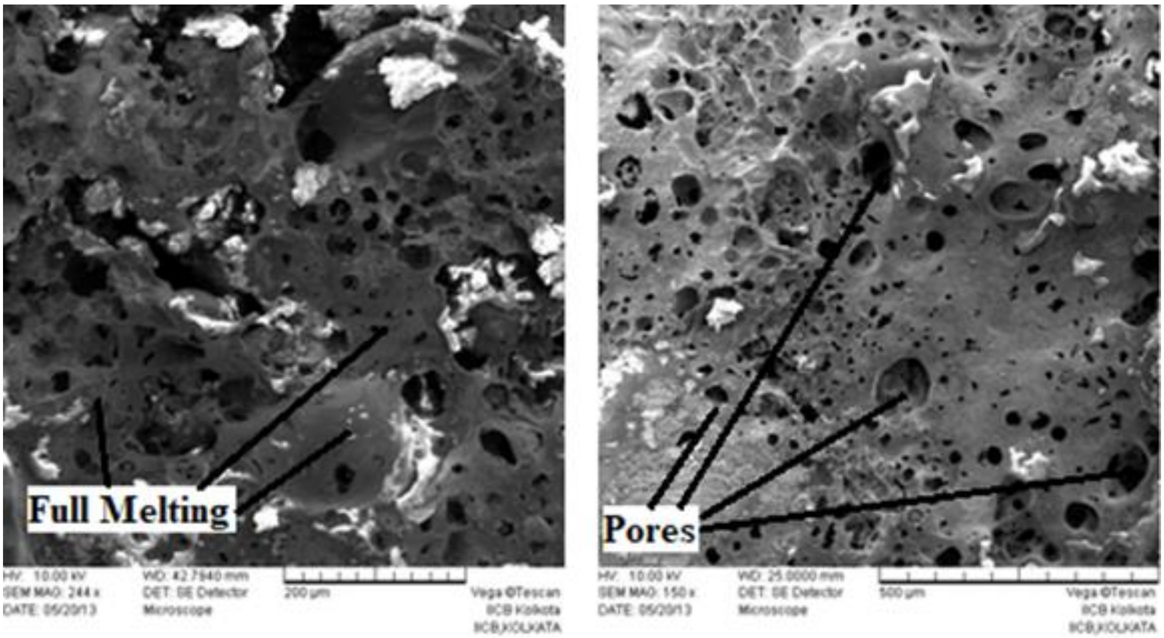
Full Melting
HV: 10.00 kV
SEM MAG: 244 x
DATE: 05/20/13
WD: 42.7940 mm
DET: SE Detector
Microscope
200 μm
Vega ©Tescan
IICB Kolkota
IICB,KOLKATA
Pores
HV: 10.00 kV
SEM MAG: 150 x
DATE: 05/20/13
WD: 25.0000 mm
DET: SE Detector
Microscope
500 μm
Vega ©Tescan
IICB Kolkota
IICB,KOLKATA

(d) Sample No. – J-4

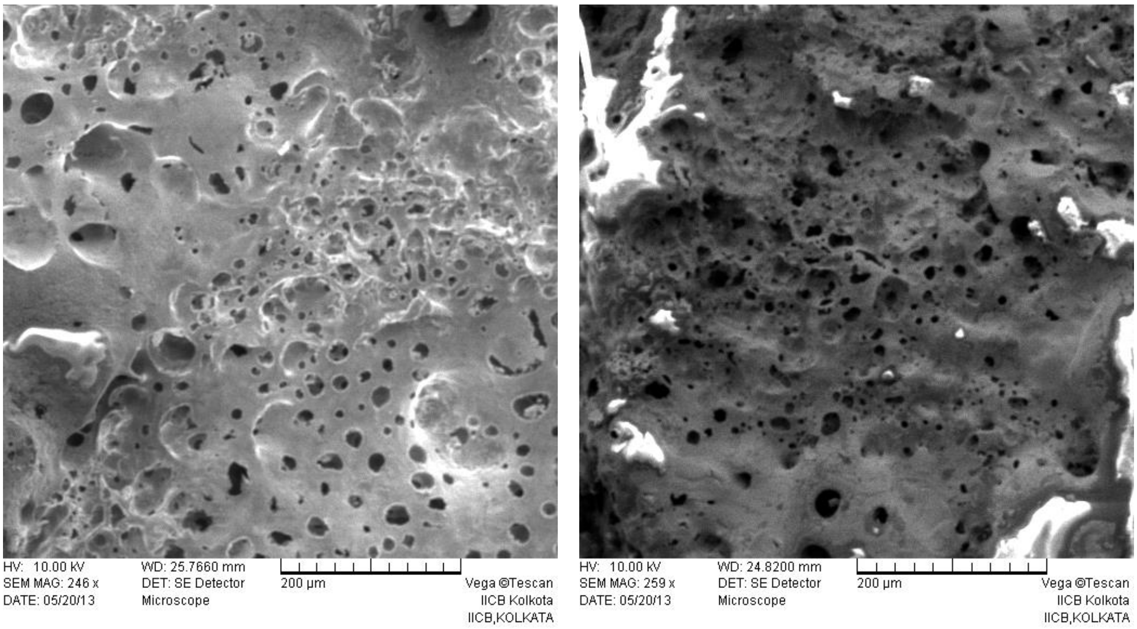
HV: 10.00 kV
WD: 25.7660 mm
SEM MAG: 246 x
DET: SE Detector
200 µm
Vega ©Tescan
DATE: 05/20/13
Microscope
IICB Kolkota
IICB,KOLKATA
HV: 10.00 kV
WD: 24.8200 mm
SEM MAG: 259 x
DET: SE Detector
200 µm
Vega ©Tescan
DATE: 05/20/13
Microscope
IICB Kolkota
IICB,KOLKATA

(e) Sample No. – J-5

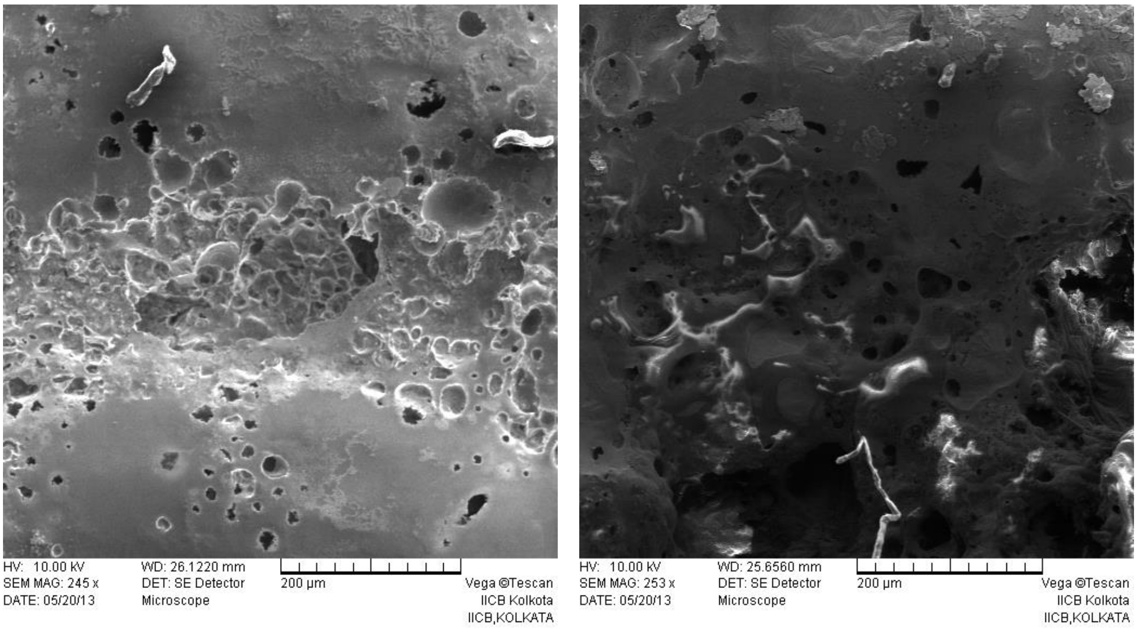
HV: 10.00 kV
WD: 26.1220 mm
SEM MAG: 245 x
DET: SE Detector
200 µm
Vega ©Tescan
DATE: 05/20/13
Microscope
IICB Kolkota
IICB,KOLKATA
HV: 10.00 kV
WD: 25.6560 mm
SEM MAG: 253 x
DET: SE Detector
200 µm
Vega ©Tescan
DATE: 05/20/13
Microscope
IICB Kolkota
IICB,KOLKATA

(f) Sample No. – J-6

Fig. 4.10: SEM Micrographs of selective laser sintered copper powder of 5µm average particle size blended with silicon oil (scanned under CW FAP Diode laser)

4.4 Summary

Experimental investigation of selective laser sintering of 5µm copper particles have been performed to explain the neck formation and porosity formation between adjacent particles. Continuous Wave laser irradiation is used to conduct sintering experiments. Parts are prepared by scanning dry copper powder as well as the copper powder blended with silicon. Processing conditions e.g. hatch spacing, scan speed and laser power are used for developing parts using Continuous Wave Diode Laser.

After removal of moisture, the almost dry copper powder is then coated over the aluminium substrate and scanned under the Continuous Wave (CW) Fibre Delivered Diode Laser to develop the part. Thick layer is created to avoid flying of powder particles from the track. Due to higher intensity of laser it can reach up to more depth of layer of copper powder. Though from the outside of developed parts look strong but those are found to be very fragile and break while removing from the substrate.

Later nine more parts are prepared by scanning 10 successive layers of copper powder with silicon oil binder using Continuous Wave Fibre Delivered Diode Laser. Six more parts are prepared by scanning 10 successive layers of copper powder with silicon oil binder using Continuous Wave (CW) Fibre Array Packages (FAP) Diode Laser.

Following are the observations:

i) The selective laser sintering of sub-micron (5µm) grainsized copper powder using Continuous Wave Fibre Delivered Diode Laser has shown successful neck growth between adjacent particles. Neck growth is appreciable during sintering of copper powder with and without binder materials.

ii) Neck formation is not very much appreciable while parts are developed by CW Fibre Array Packages (FAP) Diode Laser. Laser beam spot diameter of CW FAP diode laser is 1011.5µm and hatch spacing used is 500µm. As hatch spacing is less than laser beam spot diameter, laser beam paths are overlapped with each other. This phenomenon of overlapping of laser beam path overheats the layer of copper powder during scanning. Due to overheating copper particles are melted rather than fusing.

iii) Porosity level during sintering scanning of dry powder using CW Fibre Delivered Diode Laser become higher. Dry Sintered part become porous due to shrinkage of molten material. Developed part become very much fragile due to weak bonding between adjacent particles and layers.

iv) Porosity level becomes less due to higher intensity of continuous wave laser than the Q-switched pulsed laser.

v) Due to overheating copper powder particles melt fully (which is undesirable for sintering) and then condensed and solidified. Due to full melting of material, top surface of the solidified part become smooth but due to rapid heating, condensation and solidification large pores are created.

During MD simulation virtual experiments of sintering of copper nanoparticles full melting phenomenon is observed due to overheating. 0.72nm copper particles are heated continuously for 30ps time, but after heating for approximately 20ps, the copper nanoparticles are fully melted. Similar case of overheating is observed during scanning 5μm copper particles using CW Fibre Array Packages (FAP) Diode Laser. It is also observed that, due to overheating copper particles are fully melted.

CHAPTER – 5

GENERAL CONCLUSIONS AND FUTURE SCOPE

5.1 General Conclusions

In present research theoretical and experimental investigation have been carried out on Selective Laser Sintering of micro-nano scale metal powder. Molecular Dynamics Simulation based study for selective laser sintering of Copper nano-particles have been conducted in order to explore the mechanism of neck formation and resulting porosity creation throughout the process of selective laser sintering of nano-scale metal powder. Several Molecular Dynamics Simulation based virtual experiments have been conducted by varying particle size to explore neck formation of adjacent particles of same layer as well as subsequent layers and to quantify the porosity formation and its dependency on particle size. To explore the phenomena for micro-scale metal powder, experiments of selective laser sintering have been conducted using 5µm copper-based powder. To investigate the role of binder material, experiments of selective laser sintering of dry copper powder and mixture of copper powder with binder material have been carried out. Several experiments have been conducted to understand the influence of various processing parameters like laser source, laser power, scanning speed, hatch spacing on neck formation and porosity formation. New area of selective laser sintering in the range of submicron (less than 10µm) sized metal powder has been developed. Besides this influence of binder material during selective laser sintering of sub-micron (less than 10µm) grainsized metallic powder materials has been explored. Based on the theoretical and experimental observation following general conclusion may be drawn:

1. Molecular Dynamics simulation based virtual experiments of selective laser sintering of identical spherical copper nano-particle pair, revealed that ultra-short pulse laser irradiation has a crucial role to optimize selective laser sintering of nano-sized metal particles.

2. From the results of Molecular Dynamics simulation based virtual experiment of non-isothermal sintering of 1.82nm identical spherical copper nano-particles pair it has been observed that at the end of rapid heating at the rate of 4.0×10^{13} K/s, the diameter of neck between nano-particles become 1.2nm, and that is approximately 67% of initial diameter of particle. This phenomenon indicates strong bond between the adjacent particles.

3. Virtual experiments of sintering of pair of copper nano-particles of 1nm, pair of copper nano-particles of 2nm and pair of copper nano-particles of 3nm at same rate of heating i.e. 4.0×10^{13} K/s, show that the growth in neck diameter in lower sized nano-particles is consistent and thorough as compared to the bigger sized nano-particles pairs at the same rate of heating. The vector-plots is clearly showing that displacement of the atoms was in the direction of the point of contact of two nano-particles.

4. In order to explore and quantify the effect of particle size on formation of porosity throughout process of selective laser sintering, virtual experiments of laser sintering of four numbers of copper nano-particle were conducted using Molecular Dynamics simulations. In one experimental model, four spherical alike copper nano-particles of 0.72nm size were heated continuously for 30ps of time at 4×10^{13} K/s rate of heating. In second and third experimental models the particle size of four copper nano-particles were 1.82nm and 3.64nm respectively. In all the three cases the heating rate of 4×10^{13} K/s was maintained. From the results it was observed that four 0.72nm copper nano-particles has been melted fully and become a single near spherical nano-particle at the end of 30picosecond time. In the case of four 3.64nm copper nano-particles large pore has been observed due to very less melting of material. Whereas model of four 1.82nm nano-particles showed better result of neck formation and porosity level. From the results of these virtual experiments it may be concluded that particle size has a key role to achieve required porosity in the sintered part.

5. Experimental investigation has been carried out to explore the phenomena of neck formation and resulting porosity for micro-scale metal powder the. The results of sintering dry copper powder (without using binder materials) of average grain size 5µm has revealed a lot of difficulties and limitations like (a) flying-off particles from the track of laser irradiation, (b) shrinkage of molten melt due to rapid cooling, (c) balling phenomenon due to shrinkage of molten melt, (d) high porosity level due to flying-off of powder particles, shrinkage and balling effect, (e) difficulty in achieving strong bonding in successive layers. These difficulties and limitation could not be avoided by varying process parameters in different laser sources – diode pumped nano-second pulsed q-switched Nd:YAG laser and Continuous Wave

diode lasers. In both the cases the built-up structure collapsed as the structure was very much fragile. SEM micrographs of the broken parts showed neck formation in adjacent particles but it has been observed that the neck diameter was very low as compared to particle diameter. Due to this reason bonding of adjacent particles become weaker and built-up sintered part become fragile.

6. The difficulties and limitations, faced during sintering dry copper powder, could be resolved to a great extent by blending binder materials with copper powder. In order to investigate the effect of process parameters on neck formation between adjacent particles and bonding of neighbouring particles and subsequent layers and resulting porosity, several solid selectively laser sintered part have been developed by using different process parameters in different laser sources – diode pumped nanosecond pulsed q-switched Nd:YAG laser as well as Continuous Wave diode lasers. The SEM micrographs of all the developed sintered part reveal that neck formation between adjacent particles. The SEM micrographs of developed sintered samples at different process parameters using both the laser sources reveal that the bonding of neighbouring particles become quite strong as diameter of fully-grown neck become almost 60% to 90% of diameter of powder particle. From the SEM micrographs it is observed that fully grown neck diameter in the sintered samples using Continuous Wave diode lasers are greater as compared to the sintered samples using diode pumped q-switched nanosecond pulsed Nd:YAG laser. Due to continuous heating the neck formed thoroughly during sintering using Continuous Wave diode lasers.

   The SEM micrograph of the built-up sintered samples at laser powers of 12W, 13.65W and 15.2W and scanning speed of 3mm/s revealed that the copper particles are fully melted and solidified. This phenomenon of full melting happened due to overheating of powder layer as during laser scanning very low scanning speed and high laser power were used and also laser beam paths were overlapped with each other.

7. In order to investigate the porosity level in the sintered samples the SEM micrographs of all the sintered parts are studied. From the microscopic views (taken by optical microscope) of dry sintered powder by diode pumped q-switched nanosecond pulsed Nd:YAG laser reveal large pores in the sintered part. Due to

flying-off of powder particles, shrinkage and balling effect large pores were created. The SEM micrographs of dry sintered powder using Continuous Wave diode lasers also showed large void areas. Whereas the SEM micrographs of sintered samples of mixture of copper powder and silicon oil binder showed very less pores as compared to the dry sintered powder. Due to low porosity dense structure has been achieved. The SEM micrographs of sintered samples using Continuous Wave diode lasers showed more dense structure than the samples sintered by diode pumped q-switched nanosecond pulsed Nd:YAG laser. Porosity level became less due to higher intensity of continuous wave laser than the Q-switched pulsed laser. Due to overheating copper powder particles melted fully during scanning by CW Fibre Array Packages (FAP) Diode Laser and then condensed and solidified. Due to full melting of material, top surface of the solidified part become smooth. But due to rapid heating and rapid condensation and solidification some large pores were created.

It is expected that the present research findings will not only open up new insights to the fundamental and applied research in the area of selective laser sintering of submicron sized (less than 10µm particle size) metal powder but also help the modern manufacturing industries for proficient manufacturing of customised complex geometry microparts.

5.2 Future Scope

The future scopes of research in the area include:

i) Further Molecular Dynamics based virtual experiments can be performed for the metallic, non-metallic and composite material particles of micrometer size range on the basis of developing atomistic models applying different consideration of atomistic models and thermodynamic ensembles,

ii) Further practical experiments of selective laser sintering on nanometer range metallic, non-metallic and composite material powder particles can be performed and effect of processing parameters can be compared with theoretical study,

iii) Further experiments of selective laser sintering on micrometer range ceramic and composite material powder particles can be performed and effect of processing parameters can be investigated to achieve better result of minimizing porosity level,

iv) Fundamental research on selection of binder material during selective laser sintering to achieve better result in minimizing porosity level.

REFERENCES

References:

[01] Vaezi, M., Seitz, H. and Yang, S., 2013. A review on 3D micro-additive manufacturing technologies. *The International Journal of Advanced Manufacturing Technology*, *67*(5-8), pp.1721-1754.

[02] Bourell, D., Kruth, J.P., Leu, M., Levy, G., Rosen, D., Beese, A.M. and Clare, A., 2017. Materials for additive manufacturing. *CIRP Annals*, *66*(2), pp.659-681.

[03] Pinkerton, A.J., 2016. Lasers in additive manufacturing. *Optics & Laser Technology*, *78*, pp.25-32.

[04] Thompson, M.K., Moroni, G., Vaneker, T., Fadel, G., Campbell, R.I., Gibson, I., Bernard, A., Schulz, J., Graf, P., Ahuja, B. and Martina, F., 2016. Design for Additive Manufacturing: Trends, opportunities, considerations, and constraints. *CIRP annals*, *65*(2), pp.737-760.

[05] Tofail, S.A., Koumoulos, E.P., Bandyopadhyay, A., Bose, S., O’Donoghue, L. and Charitidis, C., 2017. Additive manufacturing: Scientific and technological challenges, market uptake and opportunities. *Materials today*, pp.22-37.

[06] Kruth, J.P., Wang, X., Laoui, T. and Froyen, L., 2003. Lasers and materials in selective laser sintering. *Assembly Automation*, *23*(4), pp.357-371.

[07] Kruth, J.P., Mercelis, P., Van Vaerenbergh, J., Froyen, L. and Rombouts, M., 2005. Binding mechanisms in selective laser sintering and selective laser melting. *Rapid prototyping journal*, *11*(1), pp.26-36.

[08] Regenfuss, P., Ebert, R. and Exner, H., 2007. Laser micro sintering–a versatile instrument for the generation of microparts. *Laser Technik Journal*, *4*(1), pp.26-31.

[09] Regenfuss, P., Streek, A., Hartwig, L., Klötzer, S., Brabant, T., Horn, M., Ebert, R. and Exner, H., 2007. Principles of laser micro sintering. *Rapid Prototyping Journal*, *13*(4), pp.204-212.

[10] Johnson, D.L., 1969. New method of obtaining volume, grain-boundary, and surface diffusion coefficients from sintering data. *Journal of Applied Physics*, *40*(1), pp.192-200.

[11] Dai, C., Zhu, H.H., Ke, L.D., Lei, W.J. and Chen, B.J., 2011. Development a Cu-based metal powder for selective laser micro sintering. In *Journal of Physics: Conference Series* (Vol. 276, No. 1, p. 012016). IOP Publishing.

[12] Ristic, M.M., 1975. Science of sintering and its future [Yugoslavia]: *International Institute for the Science of Sintering*.

[13] Ristić, M.M. and Milosević, S.Đ., 2006. Frenkel's theory of sintering. *Science of Sintering*, *38*(1), pp.7-11.

[14] Paul, S., Nagahanumaiah, Mitra, S. and Roy, D., 2018. Molecular Dynamics Simulation Study of Neck Growth in Micro-selective Laser Sintering of Copper Nanoparticles. In *Simulations for Design and Manufacturing* (pp. 259-292). Springer, Singapore.

[15] Kruth, J.P., Levy, G., Klocke, F. and Childs, T.H.C., 2007. Consolidation phenomena in laser and powder-bed based layered manufacturing. *CIRP annals*, *56*(2), pp.730-759.

[16] Mercelis, P. and Kruth, J.P., 2006. Residual stresses in selective laser sintering and selective laser melting. *Rapid prototyping journal*, *12*(5), pp.254-265.

[17] German, R.M., 2013. History of sintering: empirical phase. *Powder Metallurgy*, *56*(2), pp.117-123.

[18] Kumar, S., 2003. Selective laser sintering: a qualitative and objective approach. *Jom*, *55*(10), pp.43-47.

[19] Dong, L., Makradi, A., Ahzi, S. and Remond, Y., 2009. Three-dimensional transient finite element analysis of the selective laser sintering process. *Journal of materials processing technology*, *209*(2), pp.700-706.

[20] Glardon, R., Karapatis, N., Romano, V. and Levy, G.N., 2001. Influence of Nd: YAG parameters on the selective laser sintering of metallic powders. *CIRP Annals-Manufacturing Technology*, *50*(1), pp.133-136.

[21] Gusarov, A.V., Laoui, T., Froyen, L. and Titov, V.I., 2003. Contact thermal conductivity of a powder bed in selective laser sintering. *International Journal of Heat and Mass Transfer*, *46*(6), pp.1103-1109.

[22] Paul, R. and Anand, S., 2012. Process energy analysis and optimization in selective laser sintering. *Journal of Manufacturing Systems*, *31*(4), pp.429-437.

[23] Qian, B. and Shen, Z., 2013. Laser sintering of ceramics. *Journal of Asian Ceramic Societies*, *1*(4), pp.315-321.

[24] Senthilkumaran, K., Pandey, P.M. and Rao, P.M., 2008, August. Shrinkage compensation along single direction dexel space for improving accuracy in selective laser sintering. In *Automation Science and Engineering, 2008. CASE 2008. IEEE International Conference on* (pp. 827-832). IEEE.

[25] Fischer, P., Romano, V., Weber, H.P., Karapatis, N.P., Boillat, E. and Glardon, R., 2003. Sintering of commercially pure titanium powder with a Nd: YAG laser source. *Acta Materialia*, *51*(6), pp.1651-1662.

[26] Li, L., Hong, M., Schmidt, M., Zhong, M., Malshe, A., Huis, B. and Kovalenko, V., 2011. Laser nano-manufacturing–state of the art and challenges. *CIRP Annals-Manufacturing Technology*, *60*(2), pp.735-755.

[27] Daw, M.S. and Baskes, M.I., 1984. Embedded-atom method: Derivation and application to impurities, surfaces, and other defects in metals. *Physical Review B*, *29*(12), p.6443.

[28] Richardson, C.F. and Clancy, P., 1991. Picosecond laser processing of copper and gold: a computer simulation study. *Molecular Simulation*, *7*(5-6), pp.335-355.

[29] Pan, H., Ko, S.H. and Grigoropoulos, C.P., 2008. The solid-state neck growth mechanisms in low energy laser sintering of gold nanoparticles: a molecular dynamics simulation study. *Journal of Heat Transfer*, *130*(9), p.092404.

[30] Yang, L., Gan, Y., Zhang, Y. and Chen, J.K., 2012. Molecular dynamics simulation of neck growth in laser sintering of different-sized gold nanoparticles under different heating rates. *Applied Physics A*, *106*(3), pp.725-735.

[31] Jiang, S., Zhang, Y., Gan, Y., Chen, Z. and Peng, H., 2013. Molecular dynamics study of neck growth in laser sintering of hollow silver nanoparticles with different heating rates. *Journal of Physics D: Applied Physics*, *46*(33), p.335302.

[32] Wang, X.C., Laoui, T., Bonse, J., Kruth, J.P., Lauwers, B. and Froyen, L., 2002. Direct selective laser sintering of hard metal powders: experimental study and

simulation. *The International Journal of Advanced Manufacturing Technology*, *19*(5), pp.351-357.

[33] Salmoria, G.V., Fancello, E.A., Roesler, C.R. and Dabbas, F., 2013. Functional graded scaffold of HDPE/HA prepared by selective laser sintering: microstructure and mechanical properties. *The International Journal of Advanced Manufacturing Technology*, *65*(9-12), pp.1529-1534.

[34] Gu, D. and Shen, Y., 2006. WC–Co particulate reinforcing Cu matrix composites produced by direct laser sintering. *Materials Letters*, *60*(29-30), pp.3664-3668.

[35] Nakamoto, T., Shirakawa, N., Ueda, N., Miyata, Y. and Sone, T., 2008. Plasma nitriding to selective laser sintering parts made of SCM430 powder. *Surface and Coatings Technology*, *202*(22-23), pp.5484-5487.

[36] Singh, S.S., Roy, D., Mitra, R., Rao, R.S., Dayal, R.K., Raj, B. and Manna, I., 2009. Studies on laser sintering of mechanically alloyed Al50Ti40Si10 composite. *Materials Science and Engineering: A*, *501*(1-2), pp.242-247.

[37] Simchi, A., Petzoldt, F. and Pohl, H., 2003. On the development of direct metal laser sintering for rapid tooling. *Journal of materials processing technology*, *141*(3), pp.319-328.

[38] Zhu, H.H., Lu, L. and Fuh, J.Y.H., 2006. Study on shrinkage behaviour of direct laser sintering metallic powder. *Proceedings of the Institution of Mechanical Engineers, Part B: Journal of Engineering Manufacture*, *220*(2), pp.183-190.

[39] Regenfuss, P., Streek, A., Hartwig, L., Klötzer, S., Brabant, T., Horn, M., Ullmann, F., Ebert, R. and Exner, H., 2007. Material depending mechanisms in laser micro sintering. *Proceedings of the 5th LANE*, pp.403-418.

[40] Ebert, R., Regenfuss, P., Klötzer, S., Hartwig, L. and Exner, H., 2003, November. Process assembly for µm-scale SLS, reaction sintering, and CVD. In *Fourth International Symposium on Laser Precision Microfabrication* (Vol. 5063, pp. 183-189). International Society for Optics and Photonics.

[41] Exner, H., Regenfuss, P., Hartwig, L., Klötzer, S. and Ebert, R., 2003, November. Selective laser micro sintering with a novel process. In *Fourth International*

Symposium on Laser Precision Microfabrication (Vol. 5063, pp. 145-152). International Society for Optics and Photonics.

[42] Exner, H., Regenfuss, P., Hartwig, L., Klötzer, S. and Ebert, R., 2003. Microsintering of miniature and precise components and tools. *Proc. of the Euro-uRapid, Frankfurt/Main,* pp.1-2.

[43] Regenfuss, P., Hartwig, L., Klotzer, S., Ebert, R. and Exner, H., 2004. Microparts by a novel modification of selective laser sintering. *Technical Papers-Society of Manufacturing Engineers-All Series-*.

[44] Petsch, T., Regenfuß, P., Ebert, R., Hartwig, L., Klötzer, S., Brabant, T. and Exner, H., 2004, October. Industrial laser micro sintering. *In International Congress on Applications of Lasers & Electro-Optics* (Vol. 2004, No. 1, p. M705). LIA.

[45] Exner, H., Horn, M., Streek, A., Ullmann, F., Hartwig, L., Regenfuß, P. and Ebert, R., 2008. Laser micro sintering: A new method to generate metal and ceramic parts of high resolution with sub-micrometer powder. *Virtual and Physical Prototyping*, *3*(1), pp.3-11.

[46] Ebert, R., Ullmann, F., Hartwig, L., Suess, T., Kloetzer, S., Streek, A., Schille, J., Regenfuss, P. and Exner, H., 2010, February. Laser microsintering of tungsten in vacuum. In *Frontiers in Ultrafast Optics: Biomedical, Scientific, and Industrial Applications X* (Vol. 7589, p. 75891G). International Society for Optics and Photonics.

[47] Regenfuss, P., Hartwig, L., Klötzer, S., Ebert, R., Brabant, T., Petsch, T. and Exner, H., 2005. Industrial freeform generation of microtools by laser micro sintering. *Rapid Prototyping Journal, 11*(1), pp.18-25.

[48] Streek, A., Regenfuss, P., Ebert, R., Exner, H. and Laserapplikationszentrum, F.M., 2008. Laser micro sintering–a quality leap through improvement of powder packing. In *The Proceedings of the 19th Annual SFF Symposium* (Vol. 297).

[49] Streek, A., Regenfuss, P., Ebert, R. and Exner, H., 2009. Laser micro sintering-upgrade of the technology. In *Proceedingsof 28th International Congress on Applications ofLasers and Electro-Optics (ICALEO 2009). Orlando: Laser Institute of America* (Vol. 102, pp. 1140-1147).

[50] Chen, J., Yang, J. and Zuo, T., 2006, January. Micro fabrication with selective laser micro sintering. In *Nano/Micro Engineered and Molecular Systems, 2006. NEMS'06. 1st IEEE International Conference on* (pp. 426-429). IEEE.

[51] Paul, B., Jain, D., Bidaye, A.C., Sharma, I.G. and Pillai, C.G.S., 2009. Sintering kinetics of submicron sized cobalt powder. *Thermochimica Acta*, *488*(1-2), pp.54-59.

[52] Shirazi, S.F.S., Gharehkhani, S., Mehrali, M., Yarmand, H., Metselaar, H.S.C., Kadri, N.A. and Osman, N.A.A., 2015. A review on powder-based additive manufacturing for tissue engineering: selective laser sintering and inkjet 3D printing. *Science and Technology of Advanced Materials*, *16*(3), p.033502.

[53] Shishkovsky, I. and Scherbakov, V., 2012. Selective laser sintering of biopolymers with micro and nano ceramic additives for medicine. *Physics Procedia*, *39*, pp.491-499.

[54] Streek, A., Regenfuss, P. and Exner, H., 2013. Fundamentals of energy conversion and dissipation in powder layers during laser micro sintering. *Physics Procedia*, *41*, pp.858-869.

[55] Ghita, O.R., James, E., Trimble, R. and Evans, K.E., 2014. Physico-chemical behaviour of poly (ether ketone) (PEK) in high temperature laser sintering (HT-LS). *Journal of Materials Processing Technology*, *214*(4), pp.969-978.

[56] Das, S., Fuesting, T.P., Danyo, G., Brown, L.E., Beaman, J.J. and Bourell, D.L., 2000. Direct laser fabrication of superalloy cermet abrasive turbine blade tips. *Materials & Design*, *21*(2), pp.63-73.

[57] Kathuria, Y.P., 1999. Microstructuring by selective laser sintering of metallic powder. *Surface and Coatings Technology*, *116*, pp.643-647.

[58] Bae, S.W., Kim, D.S. and Choi, K.H., 2007, October. Development of new laser algorithm in the SFF system using a SLS process. In *Control, Automation and Systems, 2007. ICCAS'07. International Conference on* (pp. 2583-2586). IEEE.

[59] Chang, S., Li, L., Lu, L. and Fuh, J.Y.H., 2017. Selective laser sintering of porous silica enabled by carbon additive. *Materials*, *10*(11), p.1313.

[60] Chivel, Y. and Smurov, I., 2010. On-line temperature monitoring in selective laser sintering/melting. *Physics Procedia*, *5*, pp.515-521.

[61] Dürr, H., Pilz, R. and Eleser, N.S., 1999. Rapid tooling of EDM electrodes by means of selective laser sintering. *Computers in Industry*, *39*(1), pp.35-45.

[62] Kasperovich, G., Haubrich, J., Gussone, J. and Requena, G., 2016. Correlation between porosity and processing parameters in TiAl6V4 produced by selective laser melting. *Materials & Design*, *105*, pp.160-170.

[63] Kwak, S.J., Hwang, M.J. and Lee, D.Y., 2007, October. Optimal post-process of industrial solid freeform fabrication system. In *Control, Automation and Systems, 2007. ICCAS'07. International Conference on* (pp. 2578-2582). IEEE.

[64] Macedo, Z.S. and Hernandes, A.C., 2002. Laser sintering of Bi4Ti3O12 ferroelectric ceramics. *Materials letters*, *55*(4), pp.217-220.

[65] Ning, Y., Wong, Y.S., Fuh, J.Y. and Loh, H.T., 2006. An approach to minimize build errors in direct metal laser sintering. *IEEE Transactions on automation science and engineering*, *3*(1), pp.73-80.

[66] Read, N., Wang, W., Essa, K. and Attallah, M.M., 2015. Selective laser melting of AlSi10Mg alloy: Process optimisation and mechanical properties development. *Materials & Design (1980-2015)*, *65*, pp.417-424.

[67] Shaw, B. and Dirven, S., 2016, November. Investigation of porosity and mechanical properties of nylon SLS structures. In *Mechatronics and Machine Vision in Practice (M2VIP), 2016 23rd International Conference on* (pp. 1-6). IEEE.

[68] Song, J.L., Li, Y.T., Deng, Q.L. and Hu, D.J., 2007. Rapid prototyping manufacturing of silica sand patterns based on selective laser sintering. *Journal of Materials Processing Technology*, *187*, pp.614-618.

[69] Stichel, T., Frick, T., Laumer, T., Tenner, F., Hausotte, T., Merklein, M. and Schmidt, M., 2018. A Round Robin study for selective laser sintering of polymers: Back tracing of the pore morphology to the process parameters. *Journal of Materials Processing Technology*, *252*, pp.537-545.

[70] Wei, S., Bangchao, Y., Xuanhong, Z., Jianhua, M., Qifeng, P. and Xingwei, W., 2015. Effect of Sintering Time on the Microstructure of Porous Tantalum. *Rare Metal Materials and Engineering*, *44*(2), pp.319-322.

[71] Yan, W., Li, N., Li, Y., Liu, G., Han, B. and Xu, J., 2011. Effect of particle size on microstructure and strength of porous spinel ceramics prepared by pore-forming in situ technique. *Bulletin of Materials Science*, *34*(5), pp.1109-1112.

[72] Koo, B.U., Yi, Y., Lee, M. and Kim, B.K., 2017. Effects of particle size and forming pressure on pore properties of Fe-Cr-Al porous metal by pressureless sintering. *Metals and Materials International*, *23*(2), pp.336-340.

[73] Das, S., Wohlert, M., Beaman, J.J. and Bourell, D.L., 1998. Producing metal parts with selective laser sintering/hot isostatic pressing. *JoM*, *50*(12), pp.17-20.

[74] Das, S., 1999. Producing metal parts with selective laser sintering/hot isostatic pressing. *JOM*, *51*(4), pp.2-2.

[75] Duan, B. and Wang, M., 2011. Selective laser sintering and its application in biomedical engineering. *MRS bulletin*, *36*(12), pp.998-1005.

[76] Fina, F., Madla, C.M., Goyanes, A., Zhang, J., Gaisford, S. and Basit, A.W., 2018. Fabricating 3D printed orally disintegrating printlets using selective laser sintering. *International journal of pharmaceutics*, *541*(1-2), pp.101-107.

[77] Hao, L., Savalani, M.M., Zhang, Y., Tanner, K.E. and Harris, R.A., 2006. Selective laser sintering of hydroxyapatite reinforced polyethylene composites for bioactive implants and tissue scaffold development. *Proceedings of the Institution of Mechanical Engineers, Part H: Journal of Engineering in Medicine*, *220*(4), pp.521-531.

[78] Ji, L. and Jiang, Y., 2006. Dielectric and microstructure modification of Ta2O5 ceramics by laser sintering. *Materials Letters*, *60*(1), pp.86-89.

[79] Ji, L. and Jiang, Y., 2006. Laser sintering of transparent Ta2O5 dielectric ceramics. *Materials Letters*, *60*(12), pp.1502-1504.

[80] Kinzel, E., Sigmarsson, H., Xu, X. and Chappell, W., 2005. Selective laser sintering of microwave components. In *Microwave Conference, 2005 European* (Vol. 1, pp. 4-pp). IEEE.

[81] Laoui, T., Santos, E., Osakada, K., Shiomi, M., Morita, M., Shaik, S.K., Tolochko, N.K., Abe, F. and Takahashi, M., 2006. Properties of titanium dental implant models made by laser processing. *Proceedings of the Institution of Mechanical Engineers, Part C: Journal of Mechanical Engineering Science*, *220*(6), pp.857-863.

[82] Singh, J.P. and Pandey, P.M., 2013. Fitment study of porous polyamide scaffolds fabricated from selective laser sintering. *Procedia Engineering*, *59*, pp.59-71.

[83] Sun, Z., Tan, X., Tor, S.B. and Yeong, W.Y., 2016. Selective laser melting of stainless steel 316L with low porosity and high build rates. *Materials & Design*, *104*, pp.197-204.

[84] Yang, J., Shi, Y., Shen, Q. and Yan, C., 2009. Selective laser sintering of HIPS and investment casting technology. *Journal of Materials Processing Technology*, *209*(4), pp.1901-1908.

[85] Yuan, S., Zheng, Y., Chua, C.K., Yan, Q. and Zhou, K., 2018. Electrical and thermal conductivities of MWCNT/polymer composites fabricated by selective laser sintering. *Composites Part A: Applied Science and Manufacturing*, *105*, pp.203-213.

[86] Plimpton, S., 2017, October 23. LAMMPS Users Manual. Retrieved October 31, 2017, from http://lammps.sandia.gov/index.html

[87] Oluwajobi, A., 2012. Molecular Dynamics Simulation of Nanoscale Machining. *In Molecular Dynamics-Studies of Synthetic and Biological Macromolecules*. InTech.

[88] Johnson, J.K., Zollweg, J.A. and Gubbins, K.E., 1993. The Lennard-Jones equation of state revisited. *Molecular Physics*, *78(3)*, pp.591-618.

[89] Foiles, S.M., Baskes, M.I. and Daw, M.S., 1986. Embedded-atom-method functions for the fcc metals Cu, Ag, Au, Ni, Pd, Pt, and their alloys. *Physical review B, 33(12)*, p.7983.

[90] Bonny, G., Pasianot, R.C. and Malerba, L., 2009. Fe–Ni many-body potential for metallurgical applications. *Modelling and Simulation in Materials Science and Engineering, 17(2),* p.025010.

[91] Frenkel, D., Understanding Molecular Simulation/Daan Frenkel, Berend Smith. Computational *Science Series Academic Press, San Diego.–2002.–658 pp*.

[92] Morse, P.M., 1929. Diatomic molecules according to the wave mechanics. II. Vibrational levels. *Physical Review*, *34*(1), p.57.

[93] Lim, T.C., 2003. The relationship between Lennard-Jones (12-6) and Morse potential functions. *Zeitschrift für Naturforschung A*, *58*(11), pp.615-617.

[94] Tersoff, J., 1988. Empirical interatomic potential for silicon with improved elastic properties. *Physical Review B*, *38*(14), p.9902.

[95] Verlet, L., 1967. Computer" experiments" on classical fluids. I. Thermodynamical properties of Lennard-Jones molecules. *Physical review*, *159*(1), p.98.